

**NASA TECHNICAL
MEMORANDUM**

NASA TM X-52565

(NASA-TM-X-52565) THRUST AND PUMPING
CHARACTERISTICS OF CYLINDRICAL EJECTORS
USING AFTERBURNING TURBOJET GAS GENERATOR
(NASA) ~~44~~ p HC : CSCL 21E

N73-32622

Unclass

G3/28 18713

NASA TM X-52565



**THRUST AND PUMPING CHARACTERISTICS OF CYLINDRICAL
EJECTORS USING AFTERBURNING TURBOJET GAS GENERATOR**

by Nick E. Samanich and Sidney C. Huntley
Lewis Research Center
Cleveland, Ohio
1969



NASA TM X-52565

THRUST AND PUMPING CHARACTERISTICS OF CYLINDRICAL EJECTORS
USING AFTERBURNING TURBOJET GAS GENERATOR

by Nick E. Samanich and Sidney C. Huntley

Lewis Research Center
Cleveland, Ohio

NATIONAL AERONAUTICS AND SPACE ADMINISTRATION

ii

U U

THRUST AND PUMPING CHARACTERISTICS OF CYLINDRICAL EJECTORS USING AFTERBURNING TURBOJET GAS GENERATOR

By Nick E. Samanich and Sidney C. Huntley

Lewis Research Center
National Aeronautics and Space Administration
Cleveland, Ohio

ABSTRACT

Static tests of cylindrical ejectors having ejector-to-primary-diameter ratios from 1.1 to 1.6 and ejector-length-to-primary-nozzle-diameter ratios from 0.9 to 2.1 are reported. Power setting of the J85-13 turbojet engine was varied from part power to maximum afterburning. Corrected secondary weight-flow ratio was varied from 0.02 to 0.08 over a range of exhaust nozzle pressure ratios from 2.0 to 9.0. Secondary flow temperature rise and pressure-drop characteristics through the nacelle secondary flow passage were also obtained.

SUMMARY

A series of cylindrical ejector shrouds were tested with a General Electric J85-13 afterburning turbojet engine mounted in a nacelle in an altitude facility. Internal thrust, secondary flow pumping characteristics, and pressure and temperature profiles along the ejector walls were obtained. Secondary flow temperature rise and total pressure drop characteristics through the nacelle secondary passage were also determined. Power setting of the engine was varied from part power to maximum afterburning yielding exhaust gas temperatures to 2000K. The ratio of corrected secondary-to-primary weight flow was varied from approximately 0.02 to 0.08 over a range of exhaust nozzle pressure ratios from 2.0 to 9.0. The four ejectors tested had a range of ejector exit-to-primary-nozzle-diameter ratio from 1.1 to 1.6 and ejector length-to-primary-nozzle-diameter ratio from 0.90 to 2.1.

INTRODUCTION

A research program has been initiated at the Lewis Research Center to study installation effects on turbojet engine exhaust nozzles in flight over the speed range from Mach 0.5 to 1.3. An F-106 aircraft has been modified to permit the installation of two pod-mounted afterburning J-85 turbojet engines. The two strut-mounted nacelles are at a 32-percent semi-span outboard location with the exhaust nozzles in close proximity to the underside trailing edge of the wing. Plans include the testing of various types of exhaust nozzles representative of variable-geometry supersonic-cruise nozzles, some of which have cylindrical ejector shrouds



during off-design operation at low speeds. One is a variable flap ejector with the flaps fixed in the subsonic-cruise position. Another, planned for use as a reference, also has a cylindrical ejector shroud but the external surface incorporates an abrupt base step.

In order to define the internal performance of the reference and variable flap-type ejectors, as well as determine flight worthiness, a ground test version of the nacelle assembly with gas generator was tested in the Propulsion Systems Laboratory altitude chamber of the Lewis Research Center. Presented herein are the internal thrust and secondary flow pumping characteristics, as well as pressure and temperature profiles along the ejector walls, for four cylindrical ejectors. Secondary flow total pressure drop and temperature-rise characteristics through the nacelle are also reported. The ejector-to-primary-nozzle-diameter ratio varied from 1.1 to 1.6 and ejector-length-to-primary-nozzle-diameter ratio from 0.9 to 2.1. Power setting of the gas generator was varied from part power to maximum afterburning yielding exhaust gas temperatures to 2000K. Corrected secondary weight flow was varied from approximately 0.02 to 0.08 over a range of exhaust nozzle pressure ratios from 2.0 to 9.0. Cold-flow data of the research ejectors have also been obtained with 0.34 scale (21.59 cm diameter) models.

APPARATUS AND PROCEDURE

Installation

A schematic view and photograph of the research hardware installation in the altitude facility are shown in figures 1 and 2. The nacelle, which housed a J85-13 turbojet was a 63.5 cm diameter cylinder with a faired bulged section underneath the compressor region to accommodate the engine accessory package (see fig. 3). The entire engine nacelle mock-up including bellmouth, secondary-flow piping and research ejector was mounted on a rigid platform suspended by four flexure rods. Several lengths of thin wall tubing were used in the secondary airflow line between the platform and ground, which were oriented transverse to the thrust axis, to minimize any frictional effects. Pressure forces acting on the nacelle were transmitted to a water-cooled load cell used to measure thrust. A front bulkhead with a labyrinth seal around the inlet section of the nacelle separated the plenum cavity from the altitude chamber, providing a means of adjusting exhaust pressure independent of inlet pressure. Exhausters controlled the altitude cell pressure and also helped eject the gas generator exhaust gases



which were directed into an exhaust duct located immediately downstream of the exit. A minimal amount of air was discharged into the altitude cell through the bulkhead wall to keep the cell purged of exhaust gases and cooled to an acceptable temperature level.

The primary weight flow was supplied and metered to the engine through a 35.56 cm diameter bellmouth venturi. A separate supply was available for secondary weight flow. Standard ASME sharp-edged orifices were used to meter the secondary flow which was supplied to a torroidal manifold encompassing the inlet section about 40 cm upstream of the compressor face. The secondary flow was then directed through an annular channel to a conical rotating valve, see fig. 4, located on the outer periphery of the inlet just ahead of the compressor face. The flow was modulated by rotating one of two slotted mating surfaces which varied the flow area through 23 slots from closed to 290 cm². During the initial phase of testing, secondary air was scavenged from the inlet near the compressor face, as would be done in flight, to establish the inlet valve pressure-drop characteristics.

The gas generator used was a General Electric J85-13 turbojet (SN 243775) which was previously calibrated in the same facility (ref. 1). The J-85 is an afterburning turbojet having an eight-stage axial flow compressor, a two-stage axial flow turbine and has a mass of approximately 271 kilograms. It requires about 20 kg/sec airflow and at standard sea-level static conditions, develops 18,100 newtons of thrust at maximum afterburning and 12,100 newtons thrust at military power.

Test Hardware

The J-85 has a variable area primary nozzle that closely approximates a circular geometry. As the exit area is modulated for changes in power, the primary nozzle translates longitudinally and a corresponding change in exit-flow convergence angle occurs (see fig. 5). The overlapping primary leaves translate on a roller-track-cage arrangement into a nozzle-housing ring. The nozzle-housing ring has a series of 24 rectangular cut-outs (see fig. 6) located circumferentially about the ring. A flow diverter was used with all ejectors to force secondary cooling air underneath the nozzle-housing ring and over the primary leaves.

Details of the ejectors tested are presented in figure 6 and a photograph of one of them is shown in figure 7. All had cylindrical internal geometries and were constructed of Inconel 600 having a nominal wall thickness of 0.160 cm. The internal diameters of the ejectors ranged from 42.67 cm to 49.63 cm. Ejectors 1 and 2 had



the same internal diameter, 42.67 cm, but varied only in overall length.

Instrumentation

Location and details of the measuring stations of the engine-nacelle installation and ejector hardware are shown in figures 8 and 9. All thermocouples were chromel-alumel and those in the secondary passage had radiation shields. Skin temperatures were measured with the juncture of the thermocouple imbedded in the skin, flush with the hot side surface. The gas temperatures reported at the inlet to the secondary flow valve (T_{V1}) and at the exit of the secondary passage (T_S) are averages of four thermocouples located approximately 90° apart at each station, while ejector skin temperatures are averages of the thermocouples in the respective axial planes. Secondary flow total pressures reported at the secondary flow valve inlet, (P_{V1}), immediately downstream of the valve, (P_{V2}), and at the exit of the secondary passage, (P_S), are also averages of four total head probes located approximately 90° apart at each station.

The engine parameters were measured with the same instrumentation as in reference 1 except at the compressor face (Sta. 2). Average total pressure at Sta. 2 was obtained from 15 area-weighted probes located in three hollow de-icing struts.

Figure 9 shows the instrumentation which was typical of all ejectors tested. For the short ejector, the same axial spacing was used for the instrumentation which resulted in fewer measurement stations. The exit plane (Sta. 9) instrumentation was identical for all ejectors tested. The average of two static pressures located externally at Sta. 9 was used as ambient pressure, p_0 .

Procedure

Performance characteristics of each ejector configuration were investigated over a range of primary pressure ratios from 2.0 to 9.0 at corrected secondary-to-primary-cooling-flow ratios from 2 to 8 percent and J-85 power settings from approximately 95-percent speed to maximum afterburning. Pressure drop and temperature rise characteristics of the secondary flow were also determined.

Initial testing was done with the scavenge inlet system which closely simulated the geometry to be used in the flight nacelle. Pressure drop characteristics of the secondary flow valve were determined over a range of valve settings. Pressure and temperature at the compressor face were varied to encompass a range of simulated flight conditions from Mach 0.5 to 1.3. Because of the



additional weight flow being scavenged by the secondary, the engine was maintained at less than rated speed to avoid inlet choking. In subsequent tests, the thrust and pumping characteristics of the ejector nozzles were determined using a separate metered secondary air supply. Conditions in the plenum chamber were maintained relatively constant at a total pressure and temperature of $64.0 \times 10^3 \text{ N/M}^2$ and 300K. A range of pre-determined cell ambient pressures were scheduled which would result in a primary-nozzle-to-ambient-pressure-ratio range of approximately 2.0 to 9.0. At each cell pressure, the engine was operated over a range of power settings; at each power setting, secondary weight flow was varied over a nominal range of 2 to 8 percent corrected secondary flow. Pressure in the annular passage just upstream of the secondary flow valve was maintained at the same value as the compressor face pressure and the secondary flow valve area was modulated to set various secondary flows. Several ejector-skin and primary-leaf temperatures were continuously monitored during data acquisition to assure safe operating conditions.

Airflow at Sta. 1 was determined from static pressure measurements in the throat of the venturi, a calculated flow coefficient, and total pressure and temperature measurements in the plenum just ahead of the bellmouth lip. Knowing compressor inlet flow, the total pressure and temperature at the turbine discharge (Sta. 5) and the fuel flow rates, other parameters at Sta. 8 such as effective area (A_8), total pressure (P_8) and temperature (T_8) were obtained from previous calibrations (ref. 1).

The axial force transmitted to the thrust cell was composed of: (1) the nozzle thrust force; (2) inlet momentum of the primary airflow; and (3) the nacelle-bellmouth tare force. The ejector internal gross thrust, F_G , was obtained by subtracting the tare force and adding the inlet momentum to the recorded axial force. The ideal jet thrust of each stream was calculated from the measured mass-flow rate expanded isentropically from its total pressure (P_8 and P_s) to ambient pressure (p_0). The ideal thrust of the secondary flow was equated to zero when the secondary total pressure was less than ambient pressure, p_0 .

Two thrust efficiency parameters were calculated, $F_G/(F_{ip}+F_{is})$ and F_G/F_{ip} , where F_G is the ejector internal gross thrust, F_{ip} is the ideal thrust of the primary flow and F_{is} is the ideal thrust of the secondary coolant flow. The thrust-efficiency parameters, secondary total-pressure ratio, and the nozzle-pressure ratio for each nozzle configuration were plotted as a function of corrected secondary weight-flow ratio at each power setting. Values of each of these parameters were then interpolated to obtain parameters at discrete corrected secondary weight-flow ratios. These values

U U N N U N N N N N N N N N N N N N N N

are shown by symbols in all figures where corrected secondary-to-primary-flow ratios of 0.02, 0.04, 0.06 and 0.08 are stated. Actual test points were selected for all other data figures.

Although an attempt was made to repeat power settings, a variation in primary area, A_8 , and primary temperature, T_8 , did occur. Below is a tabulated summary of the variations obtained and representative values for the nominal settings quoted.

| <u>Power</u> | <u>D8 (±% tolerance), cm</u> | <u>T8 (±% tolerance), K</u> |
|--------------|------------------------------|-----------------------------|
| 95% N | 31.98 (1.3) | 755 (1.0) |
| Military | 30.46 (1.0) | 923 (1.0) |
| Min. Reheat | 32.93 (1.6) | 1230 (1.3) |
| Reheat B | 35.56 (1.7) | 1440 (2.5) |
| Reheat A | 37.35 (1.7) | 1670 (3.0) |
| Max. Reheat | 39.69 (1.7) | 1945 (2.0) |

RESULTS AND DISCUSSION

Secondary Flow Characteristics

In most supersonic turbojet installations, some type of ejector located downstream of the primary nozzle is used to pump secondary cooling air over critical engine parts and components, as well as the ejector itself. Furthermore, if judiciously chosen, increases in nozzle thrust efficiency can be obtained with the use of ejector shrouds (see refs. 2 and 3). The cooling air can be taken on-board through the engine inlet, scooped from the outer surface of the nacelle, bled from the compressor or possibly obtained through a combination of methods. Whatever method is used, the amount of cooling air that can be pumped is dependent on the pumping characteristics of the ejector nozzle and the pressure and temperature of the cooling air at the entrance to the ejector shroud. To determine these characteristics for the flight nacelle, an exact duplication of the conditions in the secondary passage was attempted. Secondary air was scavenged directly from the primary flow during the initial testing phase to measure valve pressure drop. Subsequently, a separate metered secondary air supply manifold system was installed. In both scavenge and manifold inlet systems, the path of the secondary coolant downstream of the valve was the same; the air passed over the engine outer casing and was directed under the nozzle-housing ring and into the ejector.



Summary plots of the total pressure drop and temperature rise characteristics of the secondary flow are presented in figures 10 and 11. Figure 10 presents the pressure recovery across the secondary flow valve (wide open) and the remaining recovery through the secondary passage. Both scavenge and manifold inlet systems gave comparable results. Slightly more than half of the total pressure drop occurred across the valve; approximately 75 percent of the remaining drop (data not reported) occurred between the valve and nozzle-housing ring. The data in the lower part of figure 10 reflects the total pressure recovery from the valve exit (V_2) to the secondary exit station (s). The noticeable scatter in the results can be attributed primarily to the fact that (1) the generalizing parameter $\frac{W_s \sqrt{\theta_{v1}}}{S_{v1}}$ does not reflect the

effects of the temperature rise and consequent velocity change of the secondary flow for different power settings and (2) the number of pressure measurements in the valve region was somewhat limited.

Figure 11 is a summary plot characterizing the temperature rise of the secondary cooling flow for various corrected secondary flow rates over a range of engine power settings. Presented in the figure is the total temperature rise through the nacelle from valve entrance (V_1) to secondary exit (s). Approximately half of the temperature rise occurred between the valve inlet, (V_1) and the nozzle-housing ring; the remainder occurred in the passage under the nozzle-housing ring.

Although the secondary flow characteristics are presented for the specific installation tested, they should be representative of a typical turbojet nacelle assembly. At a Mach number of 1.2 and an altitude of 11,000M (36,089 feet) with the J-85 in maximum reheat, the engine total mass flow is approximately 11.6 kg/sec (25.5 lbs/sec). Assuming a total pressure and total temperature of 54,402 N/M² (7.89 psia) and 279K (503R) at the secondary valve entrance, the secondary weight flow parameter, $\frac{W_s \sqrt{\theta_{v1}}}{S_{v1}}$ is

2.24 kg/sec (4.91 lbs/sec) for a corrected secondary-to-primary-weight-flow ratio of .05. The corresponding total cumulative pressure drop across the valve and secondary passage is approximately 7-1/2 percent with a corresponding increase in secondary flow temperature of about 170K (306R).

Pumping and Thrust Characteristics

Figures 12 through 23 show the pumping and thrust characteristics for each ejector as a function of nozzle total pressure ratio at interpolated values of corrected secondary coolant flows



of 0.02, 0.04, 0.06, and 0.08. Thrust efficiency is presented in two forms, $F_G/(F_{ip}+F_{is})$ and F_G/F_{ip} . The ideal thrust of the secondary flow was equated to zero when the total pressure of the secondary stream was less than ambient pressure, p_0 , as noted by the flagged symbols. All references in the report referring to thrust efficiency pertain to the thrust efficiency parameter $F_G/(F_{ip}+F_{is})$.

Similar characteristic trends were recorded for all ejectors. Minimum ejector thrust efficiency occurred at a nozzle pressure ratio at which the secondary flow became insensitive to further decreases in ambient pressure. This minimum pressure ratio corresponded to the value at the "knee" of the pumping characteristic curves. At this condition, a maximum amount of primary jet over-expansion existed with a correspondingly low pressure on the back side of the primary nozzle leaves.

The data for Ejector 4 is presented in figure 24 for constant values of secondary flow ratio for different engine power settings.

Several observations can be made:

1. Secondary flow markedly improved the thrust efficiency at all power settings tested.
2. When operating near the design pressure ratio, thrust efficiencies approaching 98 percent were measured with moderate amounts of secondary flow.
3. Internal thrust efficiencies of near 90 percent were measured when operating at very low pressure ratios (≤ 3.0) compared to design (16.0) with the primary jet separated from the ejector wall and with moderate secondary flows.

Figure 25 compares the thrust efficiency of Ejectors 1 and 2 which differ only in overall length. The data is plotted for a military power setting which geometrically results in an ejector-to-primary-diameter ratio of 1.42 and an ejector-length-to-primary diameter of 2.06 and 1.03 for the long and short ejectors, respectively. It can be noted that the efficiency of both ejectors was comparable at nozzle pressure ratios near the design value of 9.7. However, there was a marked difference at low pressure ratios with the short ejector having considerably higher efficiency. This was due primarily to the fact that with the short ejector the primary jet separated more readily from the shroud. Since its pumping characteristics were poorer prior to jet attachment, higher secondary pressure levels were required to pump the same secondary flows.



These higher pressures resulted in a higher net force acting on the back side of the primary leaves in the thrust direction.

The secondary-to-primary-pressure ratio at which the secondary flow becomes insensitive to downstream pressure disturbances, sometimes called minimum ejector pressure ratio, is compared with theory (ref. 4) and to the cold-flow model data in figure 26. Agreement with theory is good at the lower values of the secondary flow but deviates at the higher flows with the experimental data indicating poorer than predicted pumping capability. The 0.34 scale cold-flow model data exhibited somewhat better pumping characteristics (lower ejector pressure ratio) than the hot full-scale hardware.

Wall Pressure and Temperature Profiles

Figure 27 shows pressure and temperature profiles along the wall of Ejector 3 for various power settings. At each power setting, the data for the various nozzle pressure ratios tested are shown. The behavior of the two stream flows appears similar at all power settings. At the low pressure ratios, the primary jet was separated from the shroud with the secondary flow adjusting to local ambient pressure at the exit. As pressure ratio was increased to a "critical" value, primary jet attachment to the ejector shroud occurred. Upon reaching this condition, the secondary flow parameters upstream of the mid-shroud location became insensitive to further nozzle pressure ratio increases. As nozzle pressure ratio was increased beyond the "critical" value, the secondary flow increased in velocity along the shroud to a point where the flow could no longer sustain any further overexpansion and the jet separated from the shroud wall. The flow then incurred a sharp pressure discontinuity adjusting to local ambient pressure at the exit. As pressure ratio was further increased, a value was reached (still lower than design) where the secondary flow accelerated continuously to the ejector shroud exit where the local pressure was lower than ambient pressure. In this case the nozzle was flowing full but overexpanded. Any further increases in nozzle pressure ratio did not affect the internal-ejector characteristics. At the lower-power settings, maximum skin temperatures occurred near the midpoint of the ejector; at higher-power settings, maximum skin temperatures were measured near the exit of the ejector shroud.

SUMMARY OF RESULTS

The following results were obtained from static altitude tests of four cylindrical ejectors having ejector-to-primary-diameter ratios from 1.1 to 1.6 and ejector-length-to-primary-diameter ratios from 0.9 to 2.1 using an afterburning gas generator. Data were

U U U U U U U U U U U U U U U U U U U U

obtained at corrected secondary-to-primary-weight-flow ratios from 0.02 to 0.08 over a range of exhaust nozzle pressure ratios from 2.0 to 9.0.

1. High values of internal thrust efficiency, on the order of 98 percent, were measured with cylindrical ejectors near their design pressure ratio with moderate amounts of secondary flow.
2. Internal thrust efficiencies near 90 percent were measured at very low pressure ratios (≤ 3.0) compared to design (~ 16.0) with the primary jet separated and moderate secondary weight flows.
3. At a simulated Mach 1.2 flight condition, the secondary air temperature rise was 170K and the total cumulative pressure drop across the secondary flow valve and the passage between the nacelle and engine was 7-1/2 percent at a maximum reheat power setting and five percent corrected secondary cooling flow.
4. Theoretical predictions of the pumping characteristics agreed well with the data at low values of secondary flow but were overly optimistic at the higher rates.
5. Cold-flow scale-model data exhibited somewhat better pumping characteristics than measured with the hot full-scale hardware.

SYMBOLS

| | |
|-------|--|
| A | area (cold), cm^2 |
| A_8 | primary nozzle exit effective flow area, cm^2 |
| D | diameter (cold), cm |
| D_8 | primary nozzle exit diameter based on A_8 , cm |
| F | jet thrust, N |
| F_G | measured ejector internal gross thrust, N |
| L | ejector length measured from primary nozzle exit, cm |
| l | distance aft of primary nozzle, cm |
| P | total pressure, N/M^2 |
| p | static pressure, N/M^2 |



| | |
|-------------------|---|
| $(P_8/p_0)_{des}$ | pressure ratio corresponding to supersonic one-dimensional isentropic expansion from A_8 to A_9 |
| $(P_s/P_8)_{min}$ | ejector pressure ratio at which the secondary flow becomes independent of downstream conditions |
| r | radius, cm |
| T | total temperature, K |
| t | static temperature, K |
| w | weight flow, kg/sec |
| x | axial station (compressor face arbitrarily assigned as station 254.0), cm |
| α | angle formed by the inner surface of primary nozzle leaves with respect to horizontal centerline, deg |
| δ | dimensionless ratio of total pressure to standard sea-level pressure of $101.329 \times 10^3 \text{ N/M}^2$ |
| θ | dimensionless ratio of total temperature to standard sea-level temperature of 288.15K |
| τ | ratio of secondary total temperature at exit of secondary passage to primary total temperature |
| ω | ratio of secondary-to-primary-weight flows |

Subscripts

| | |
|----|--|
| ej | ejector wall |
| ip | one-dimensional isentropic expansion of primary flow |
| is | one-dimensional isentropic expansion of secondary flow |
| s | exit of secondary passage |
| v1 | secondary flow valve entrance |
| v2 | secondary flow valve exit |
| 0 | ambient in altitude cell |
| 8 | primary nozzle exit |
| 9 | ejector shroud exit |



REFERENCES

1. Antl, R. J.; and Burley, R. R.: Steady-State Airflow and Afterburning Performance Characteristics of Four J85-GE-13 Turbojet Engines. NASA TMX-1742, 1969.
2. Greathouse, W. K.; and Hollister, D. P.: Airflow and Thrust Characteristics of Several Cylindrical Cooling-Air Ejectors With a Primary to Secondary Temperature Ratio of 1.0. NACA RM E52L24, 1953.
3. Trout, A. M.; Papell, S. S.; and Povolny, J. H.: Internal Performance of Several Divergent-Shroud Ejector Nozzles With High Divergence Angles. NACA RM E57F13, 1957.
4. Kochendorfer, F. D.; and Rousso, M. D.: Performance Characteristics of Aircraft Cooling Ejectors Having Short Cylindrical Shrouds. NACA RM E51E01, 1951.

U U U U U U U U U U U U U U U U U U U U

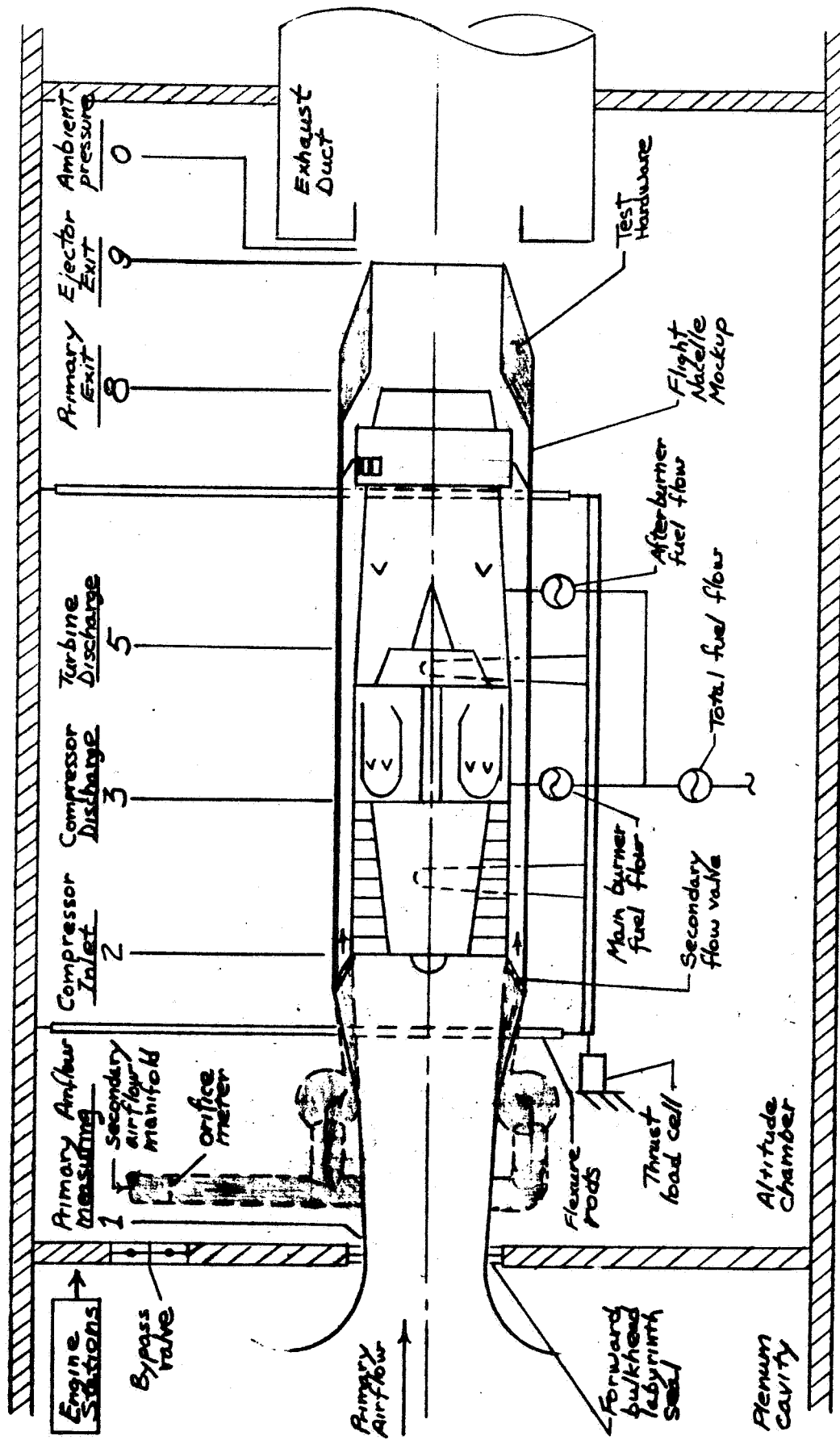


Figure 1 - Schematic of Test Installation

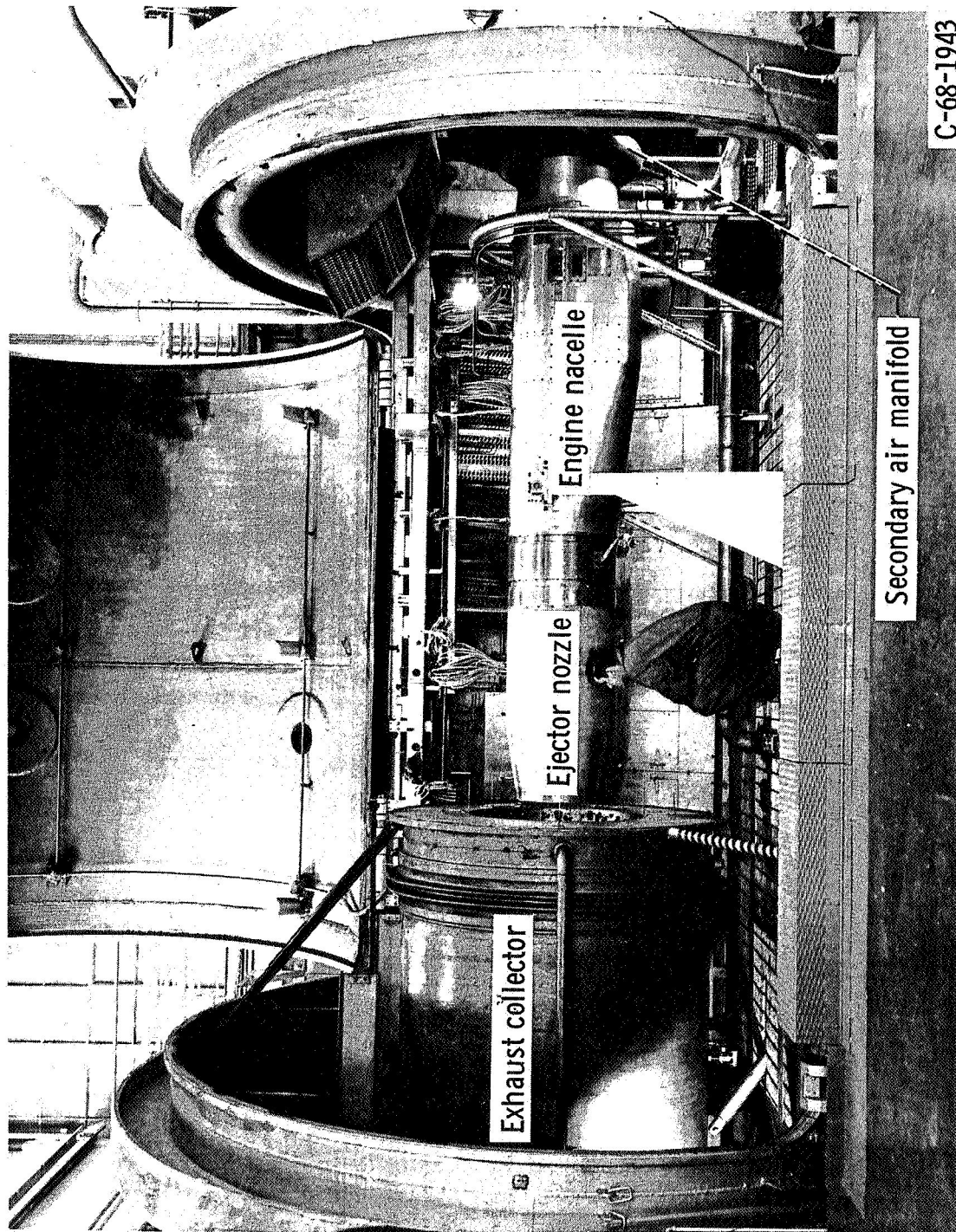


Figure 2. - Photograph of test hardware in altitude chamber.

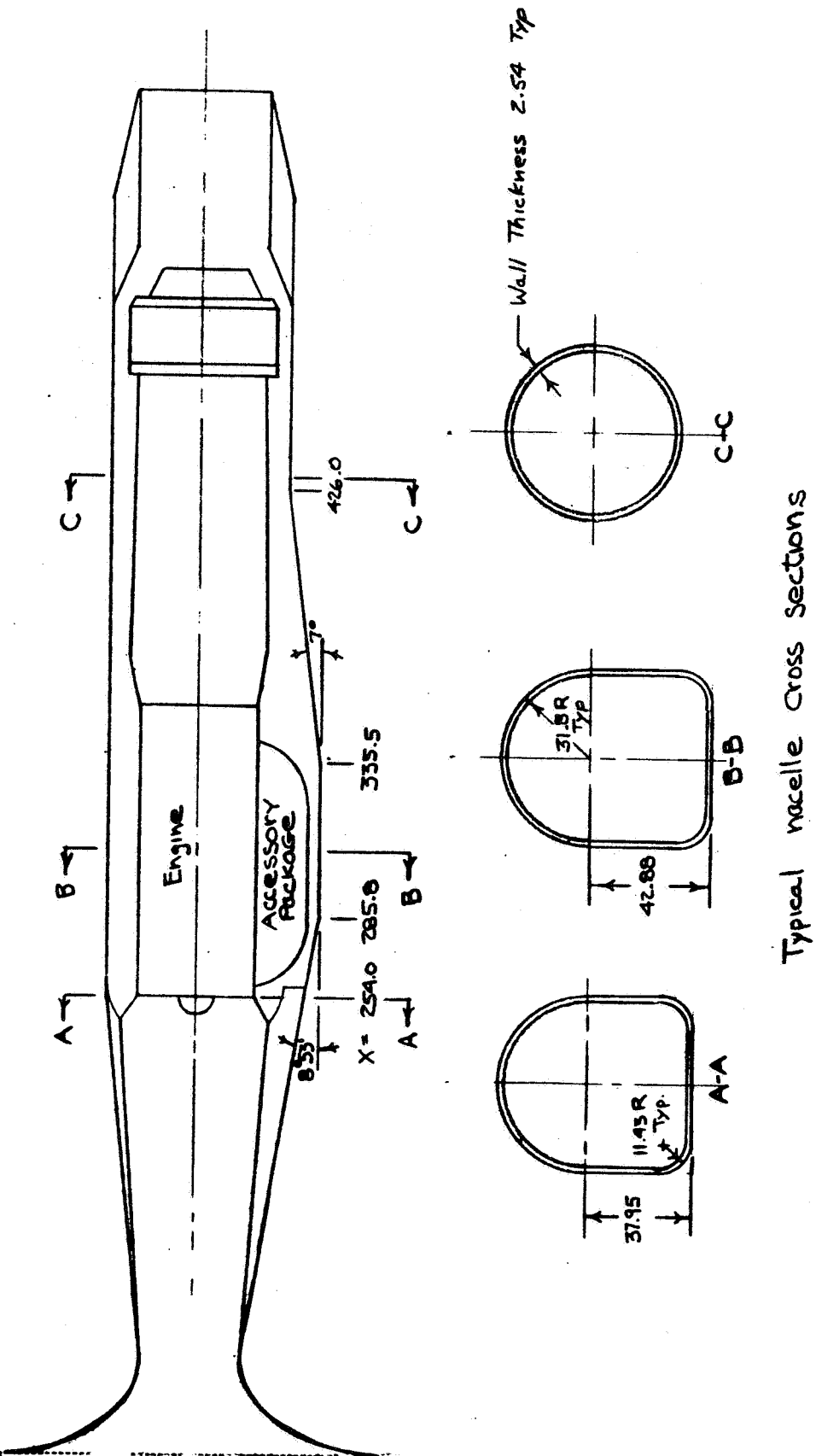


Figure 3 - Nacelle Details

E-4967

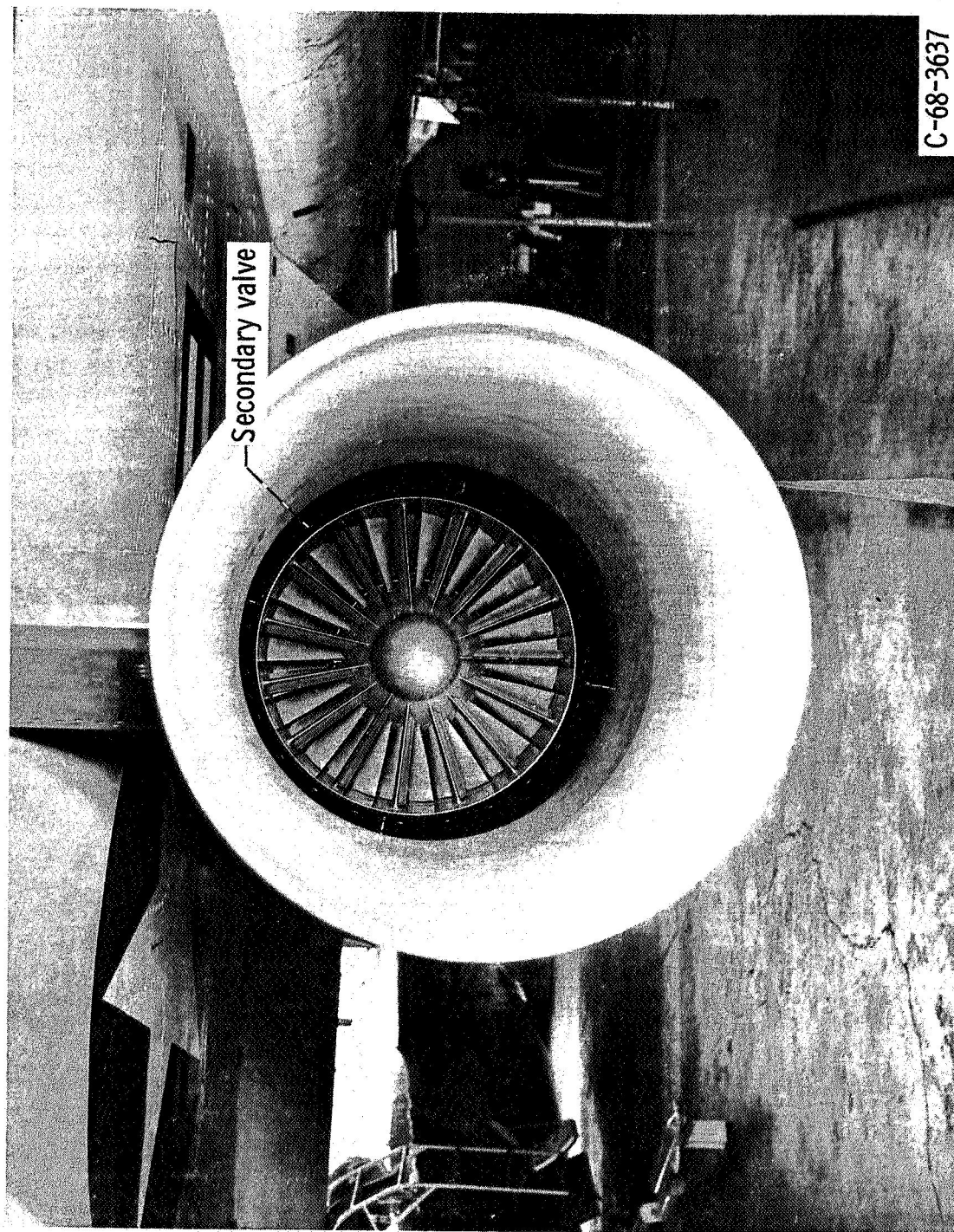


Figure 4. - Photograph showing secondary flow valve.

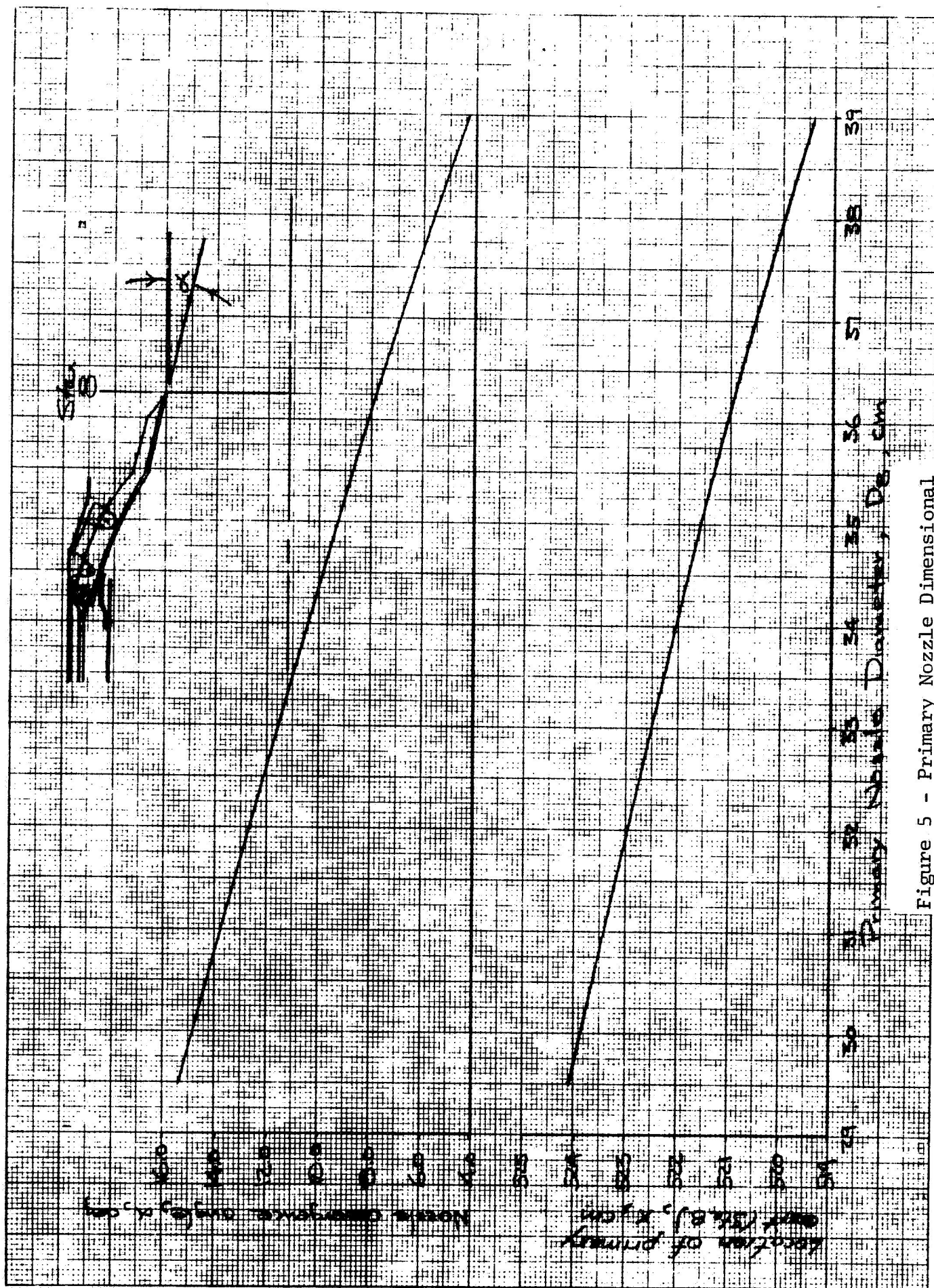


Figure 5 - Primary Nozzle Dimensional Characteristics

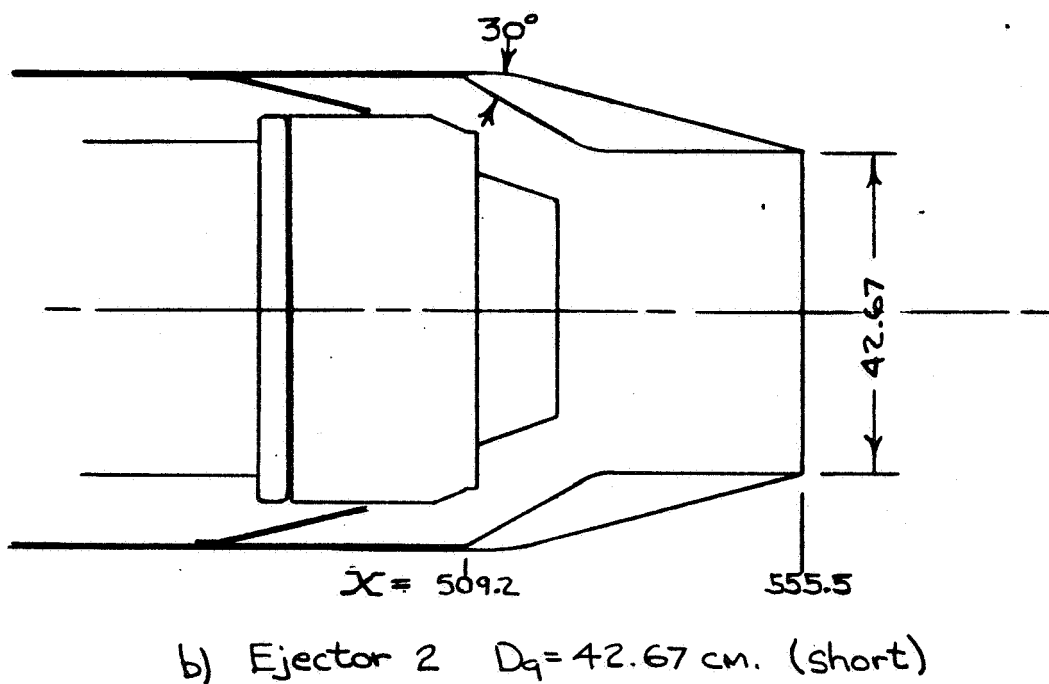
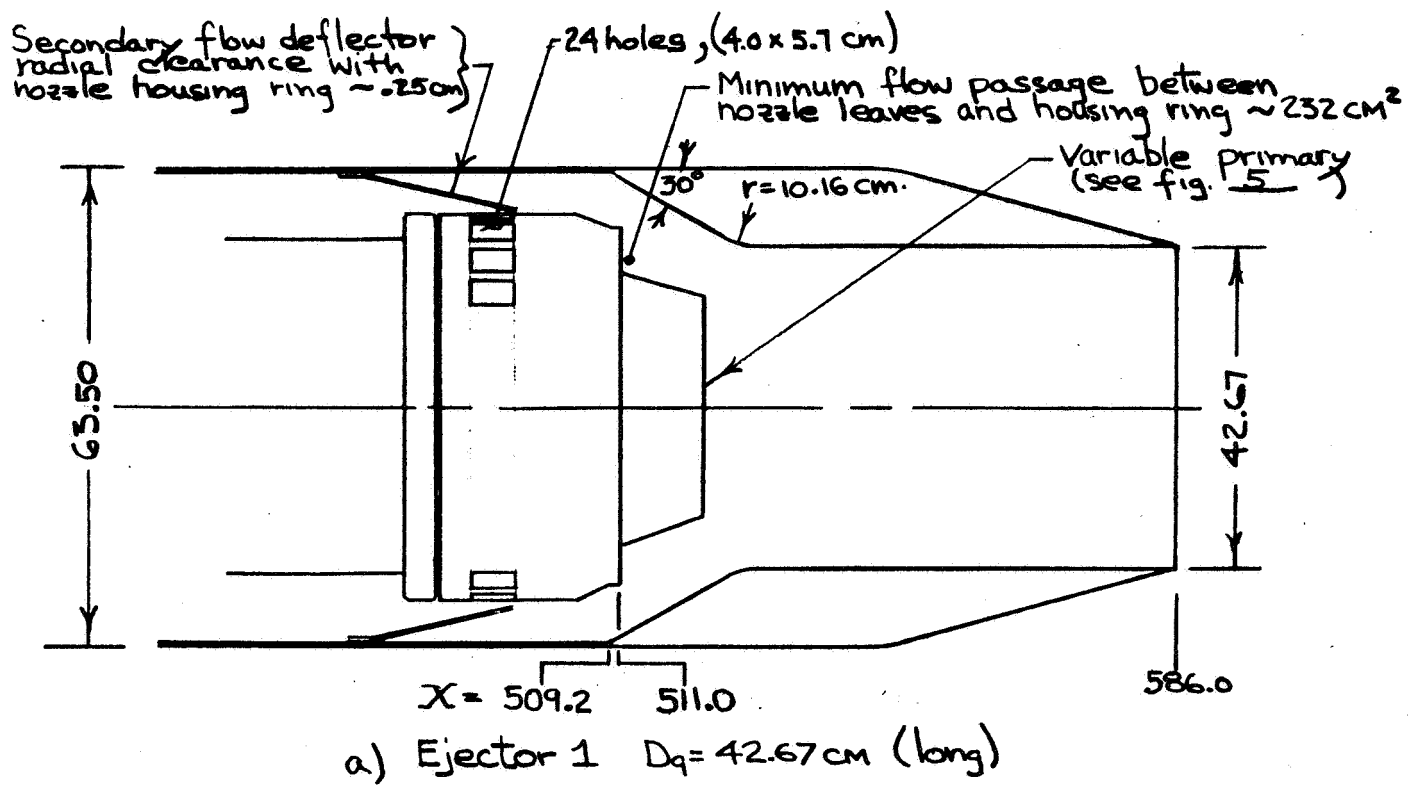
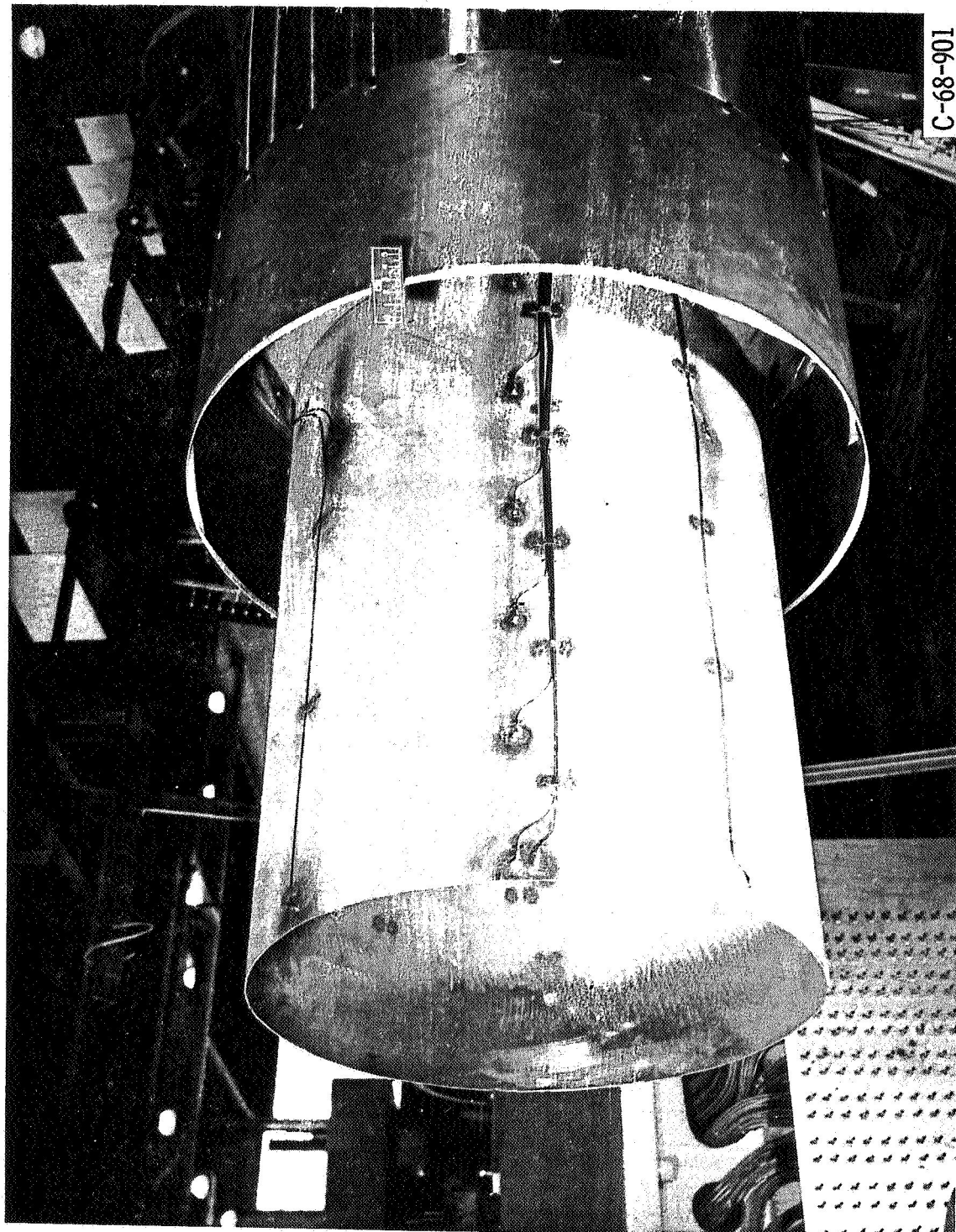


Figure 6 - Dimensional Characteristics of Ejector Nozzles

E-4967



C-68-901

Figure 7. - Photograph of ejector 3.

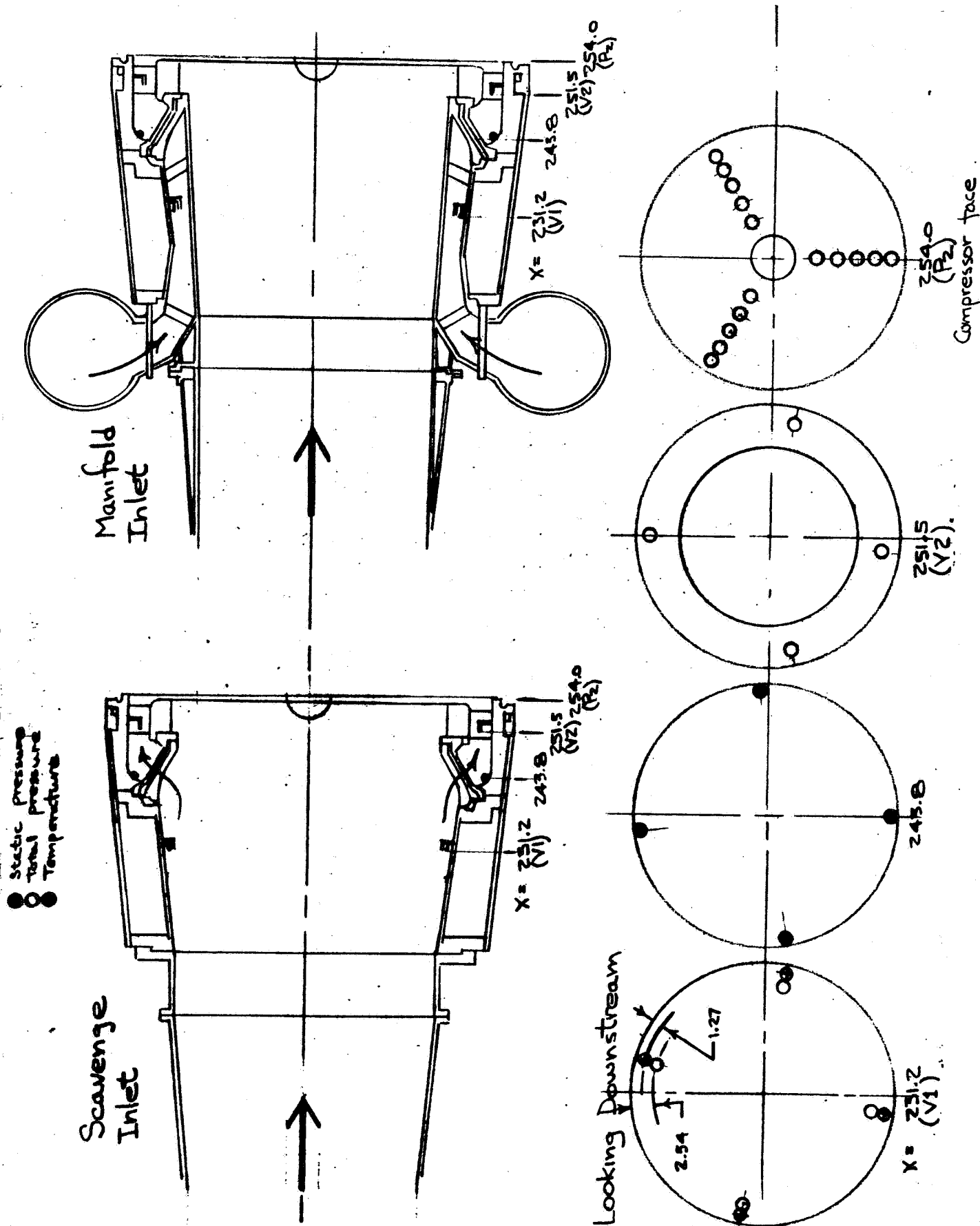


Figure 8 - Instrumentation Details of Inlet Region

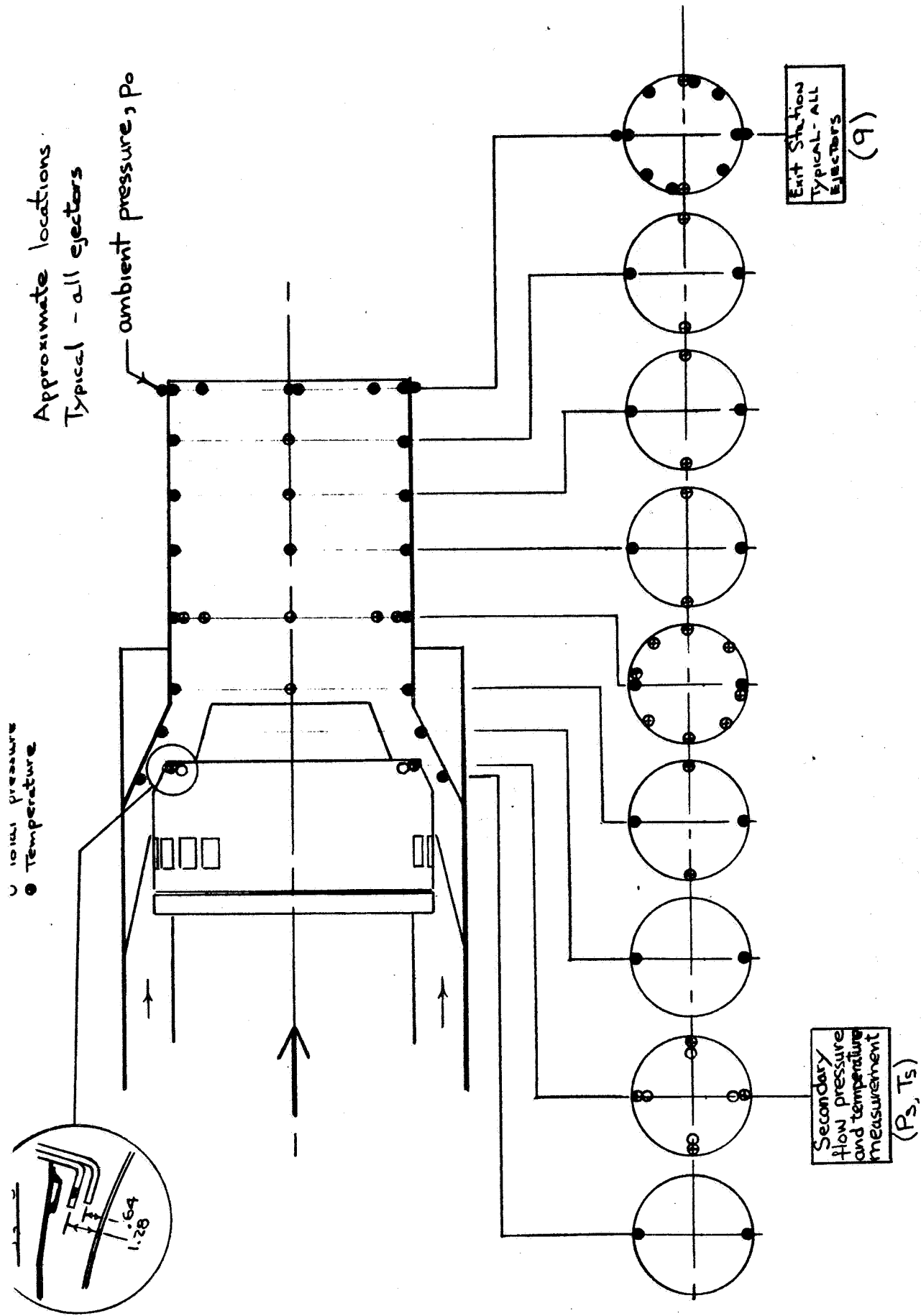


Figure 9 - Instrumentation Details
of Ejectors

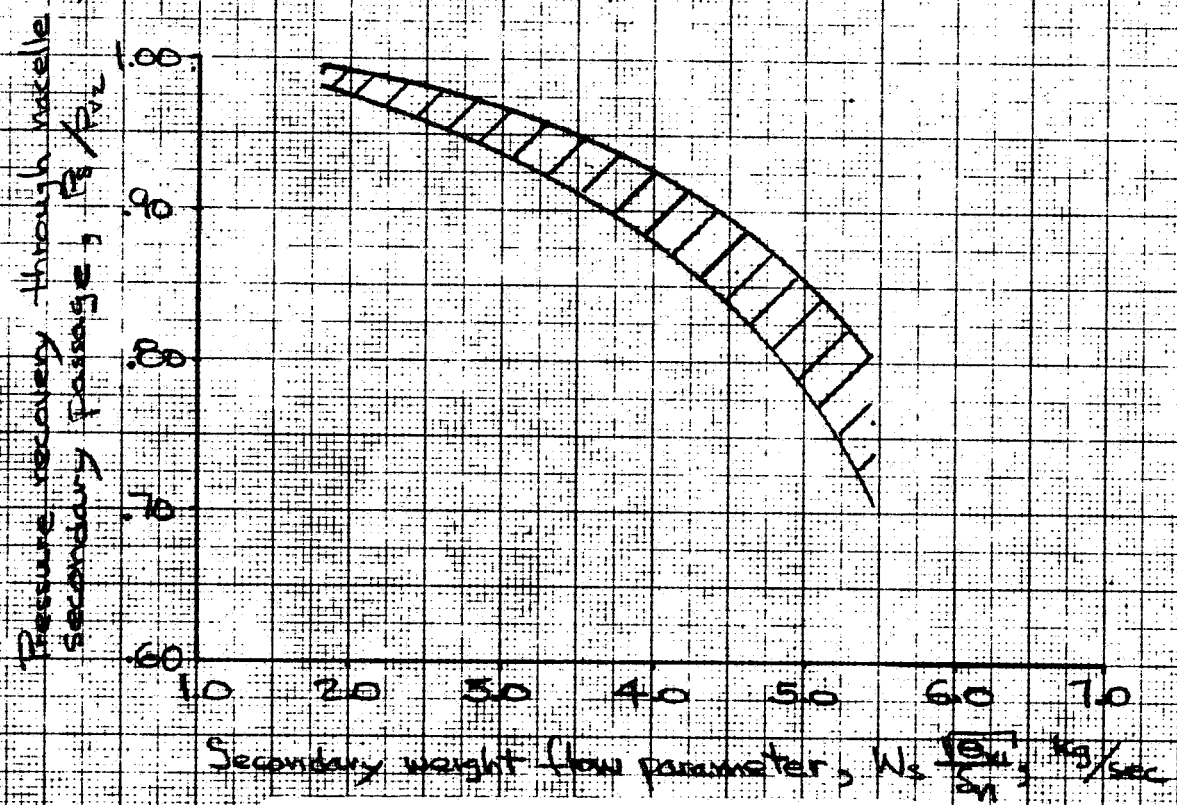
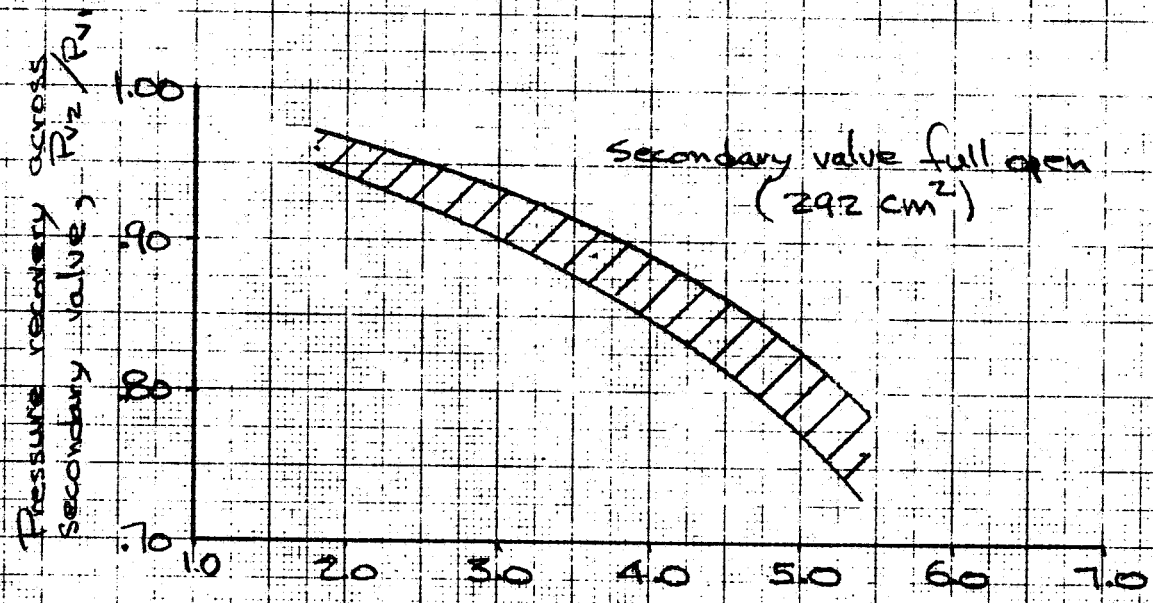


Figure 10 - Secondary Flow Pressure Drop Characteristics

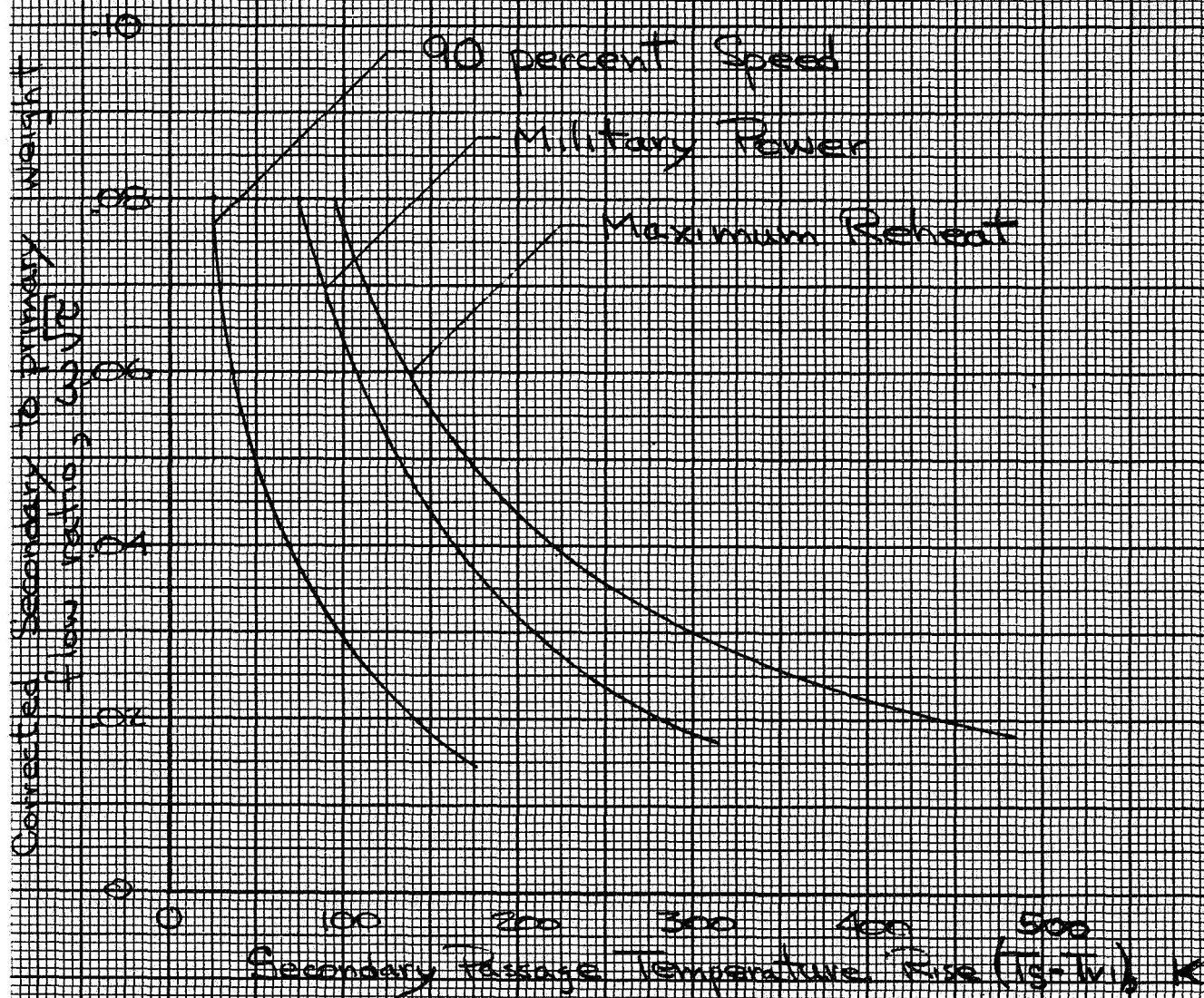


Figure 11 - Nacelle Secondary Flow Temperature Rise

P_0/P_0
 O 1.42
 Δ 1.32
 ▽ 1.17
 Flashed symbols P_0/P_0

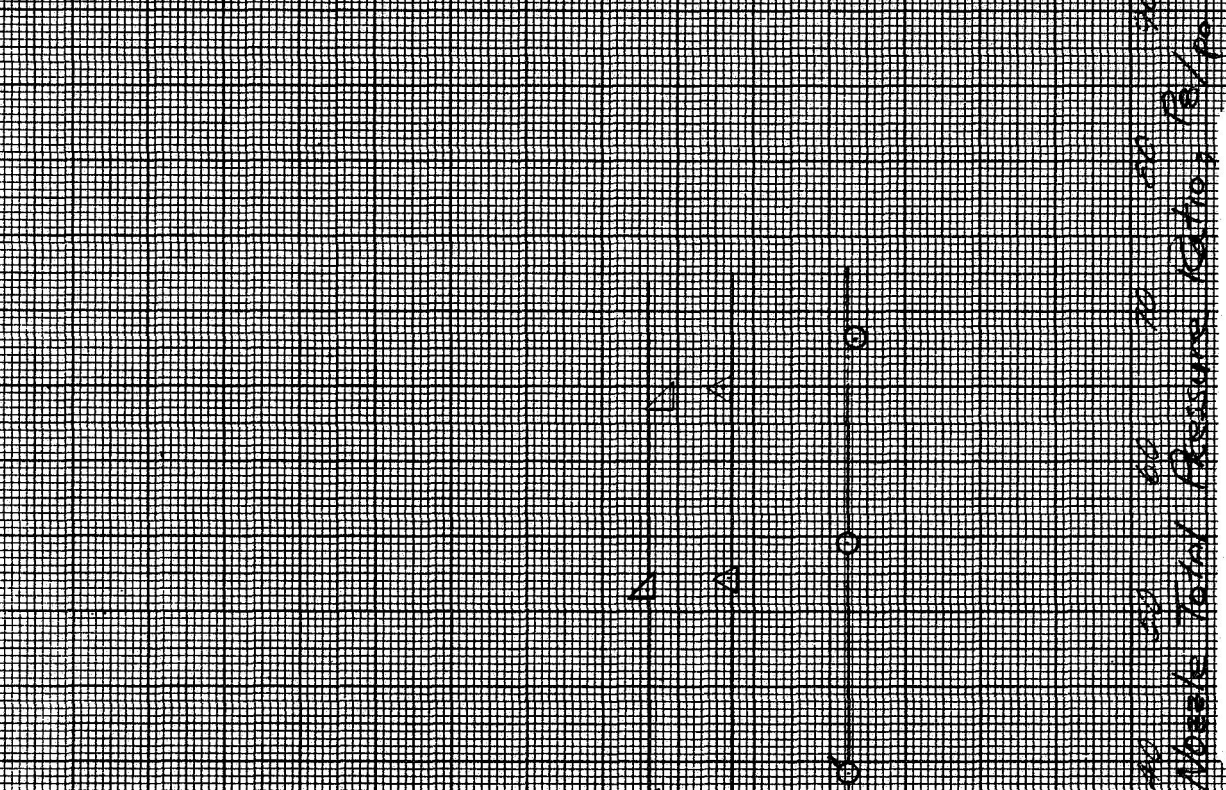


Figure 12a - Secondary Flow Pumping Characteristics
 Ejector 1 $W/P_0 = 0.02$

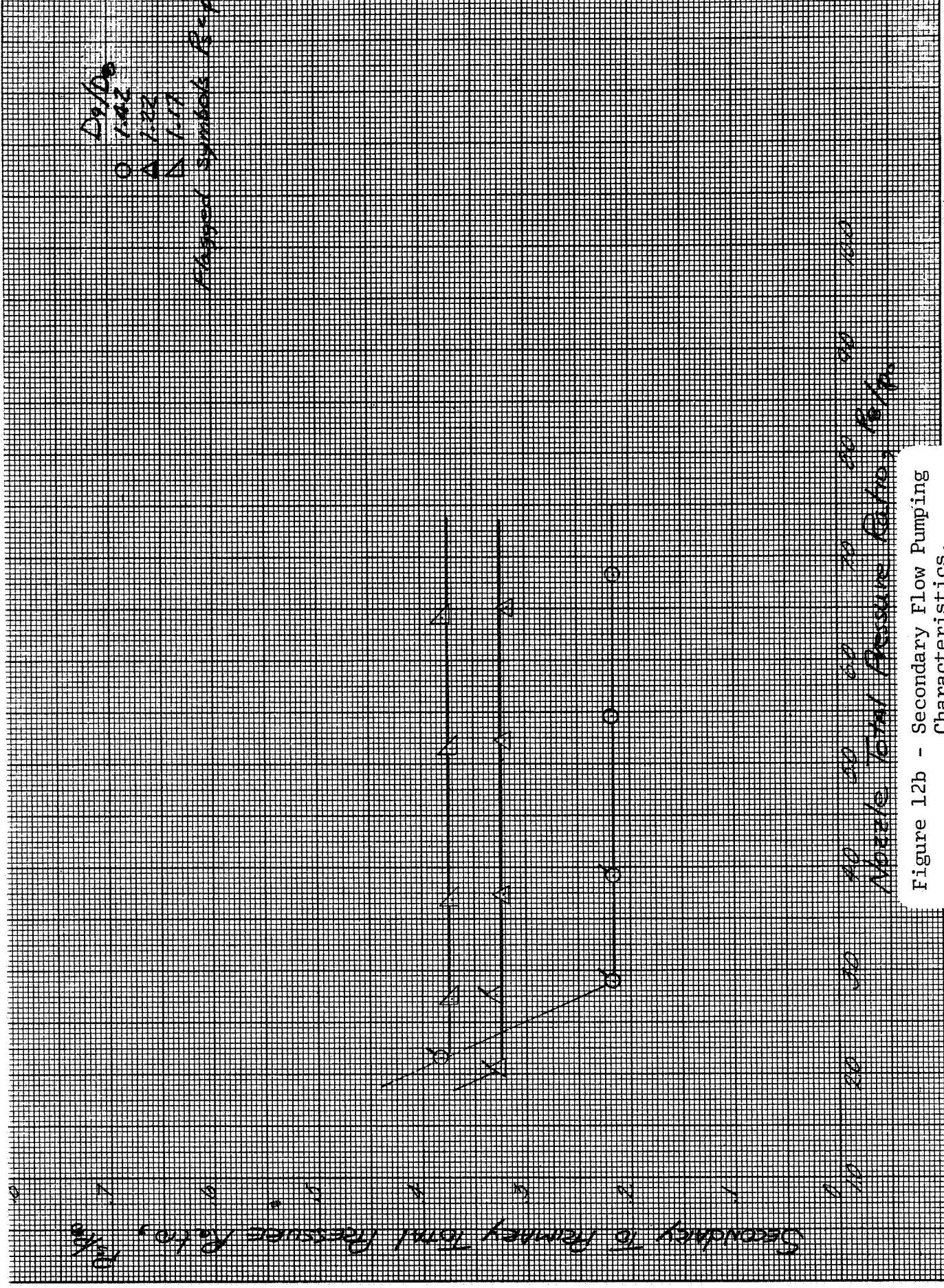


Figure 12b - Secondary Flow Pumping Characteristics
Ejector 1 $\omega\sqrt{P_1} = .04$

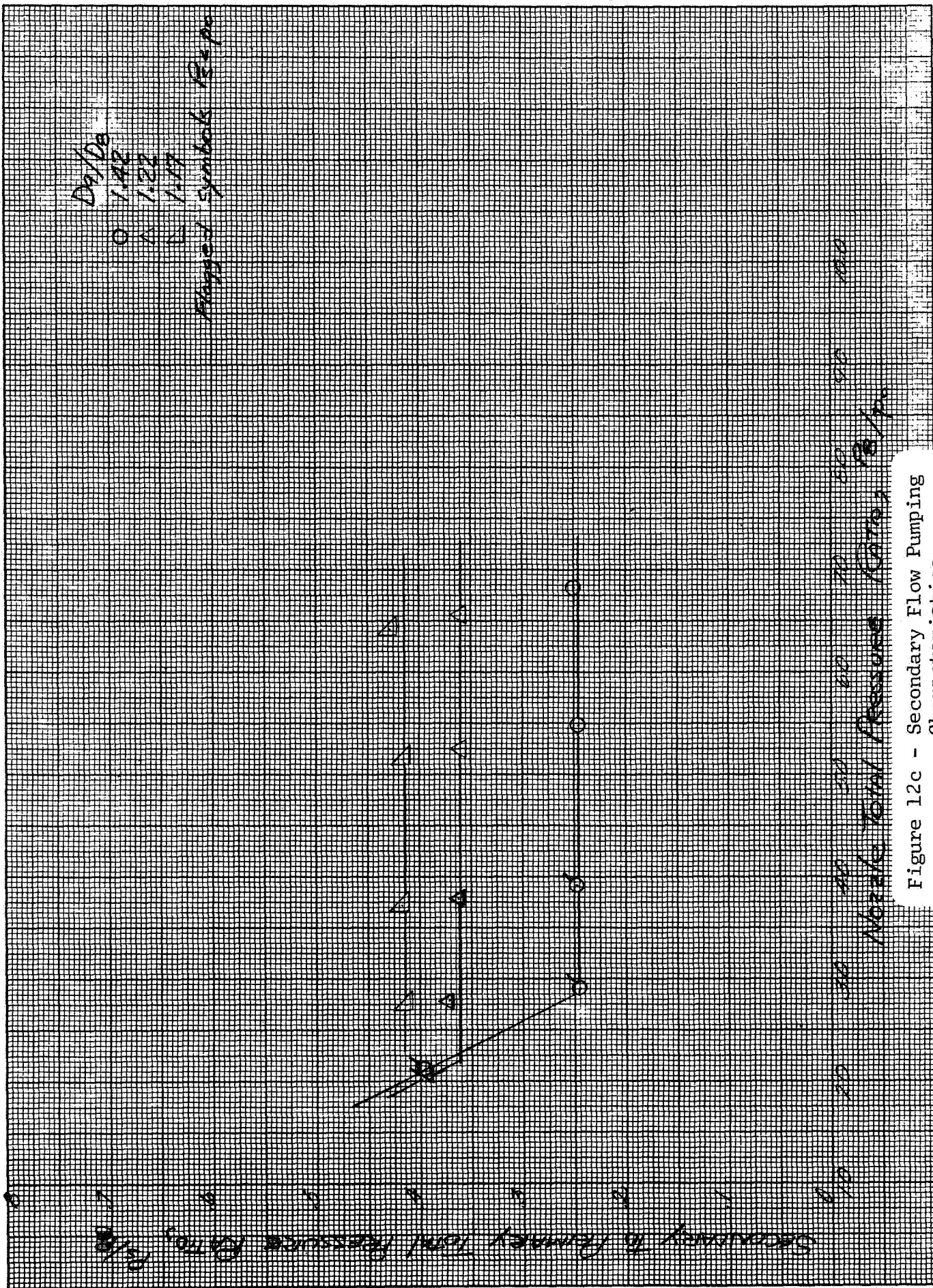


Figure 12c - Secondary Flow Pumping Characteristics
Ejector 1 $\omega\sqrt{\tau} = 0.06$

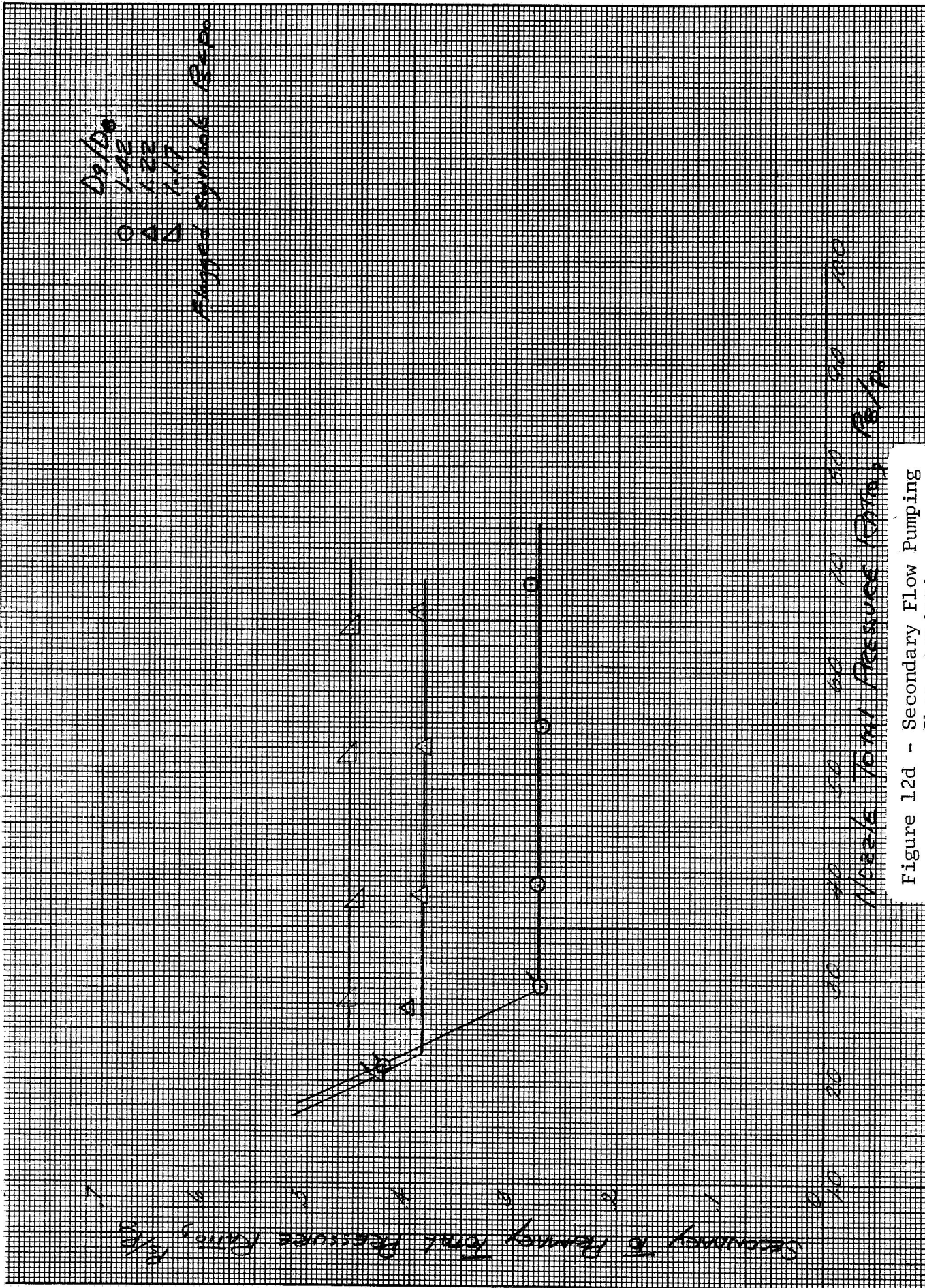


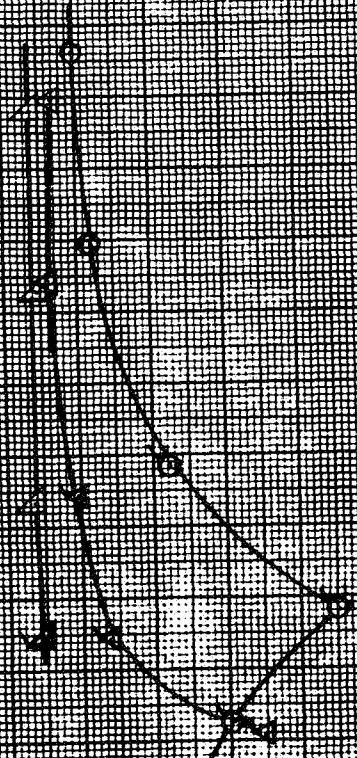
Figure 12d - Secondary Flow Pumping Characteristics,

Ejector 1 $WVR = 0.08$

$\Delta p / p_0$
 0 1.42
 0 1.25
 0 1.17

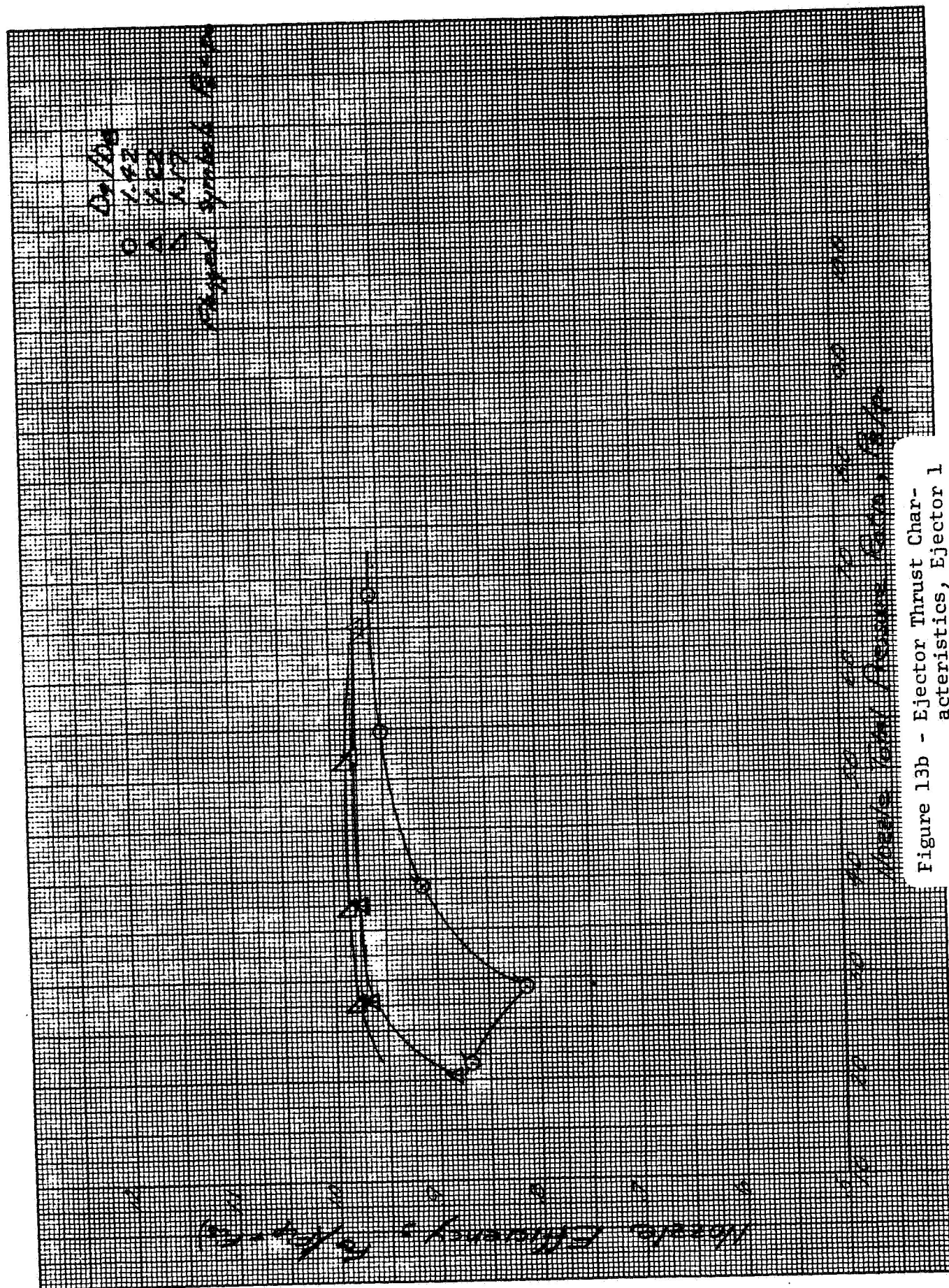
Plotted Symbols Refer

Nozzle Efficiency, ϵ_{Nz}



Nozzle Exit Pressure Ratio, P_e/P_0

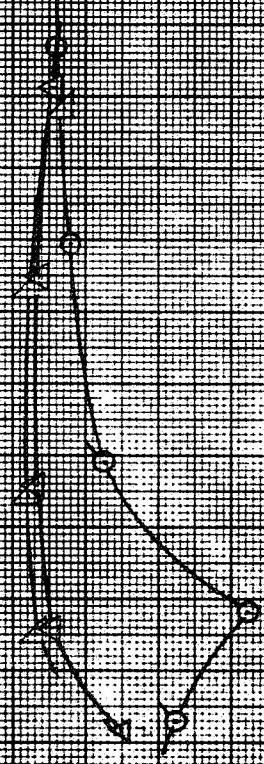
Figure 13a - Ejector Thrust Characteristics, Ejector 1
 $\omega/\sqrt{\gamma} = .02$



0.100
 0.102
 0.103
 0.104

0.100
 0.102
 0.103
 0.104

Absolute Efficiency - 0.64 - 0.70



0.100
 0.102
 0.103
 0.104

Absolute Total Pressure Ratio

Figure 13c - Ejector Thrust Characteristics, Ejector 1
 $\omega/\sqrt{\gamma} = 0.06$



Figure 13d - Ejector Thrust Characteristics, Ejector 1
 $\omega \sqrt{\tau} = .08$

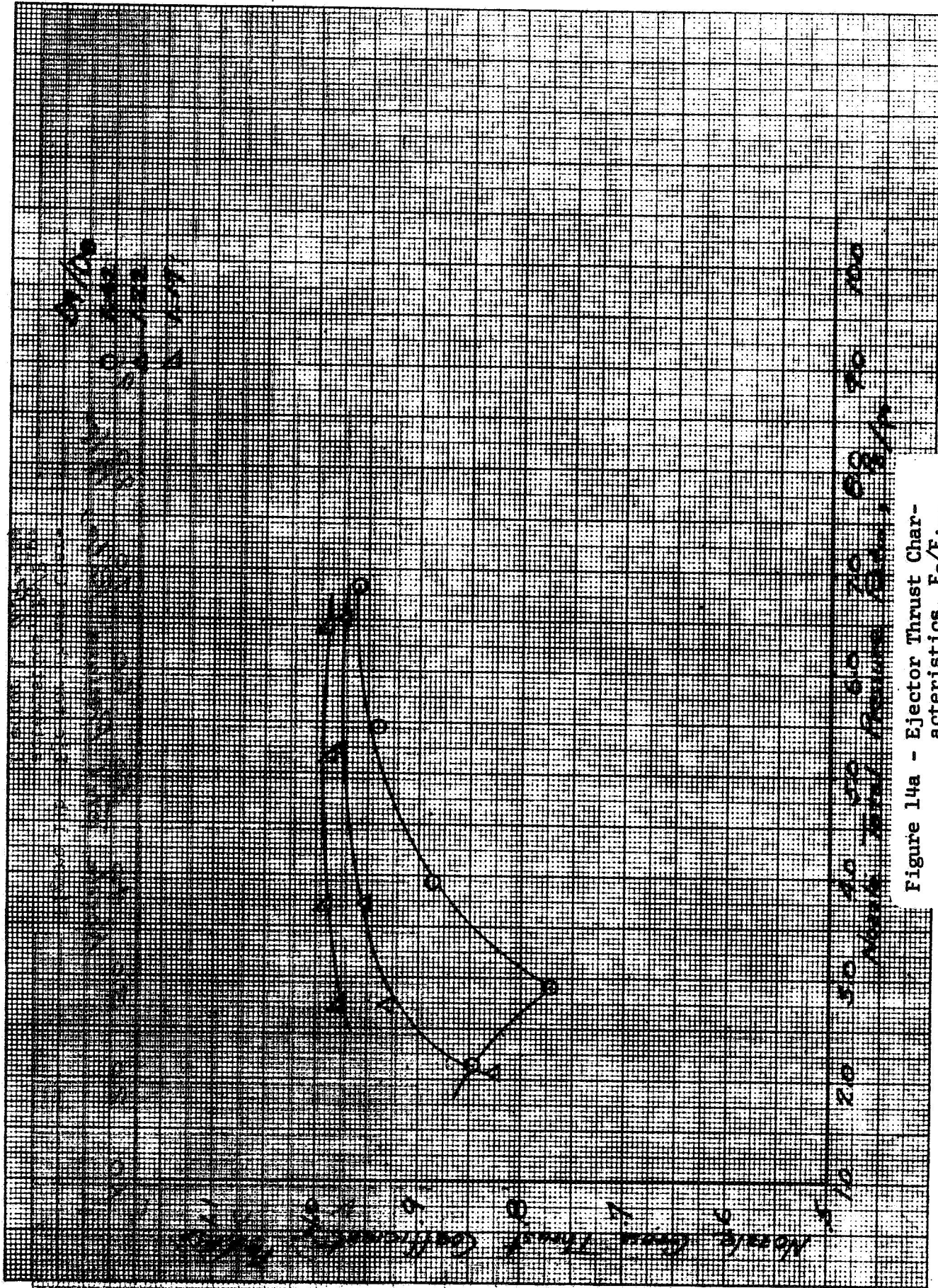


Figure 14a - Ejector Thrust Characteristics, $F_{G/Fip}$, Ejector 1 $\omega V^2 = .02$

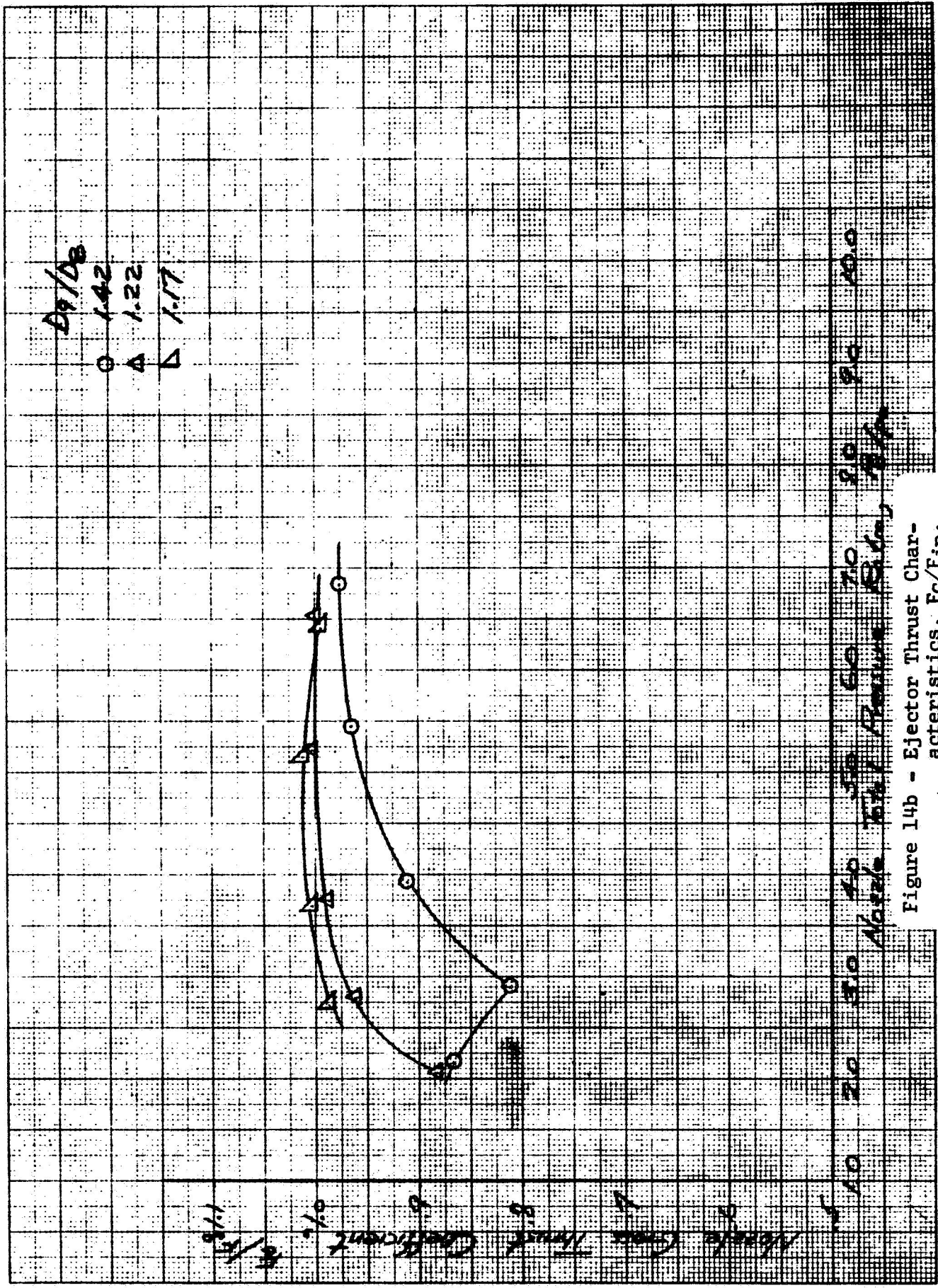


Figure 14b - Ejector Thrust Characteristics, F_g/F_{ip} , Ejector 1 $\omega \sqrt{P} = 0.04$

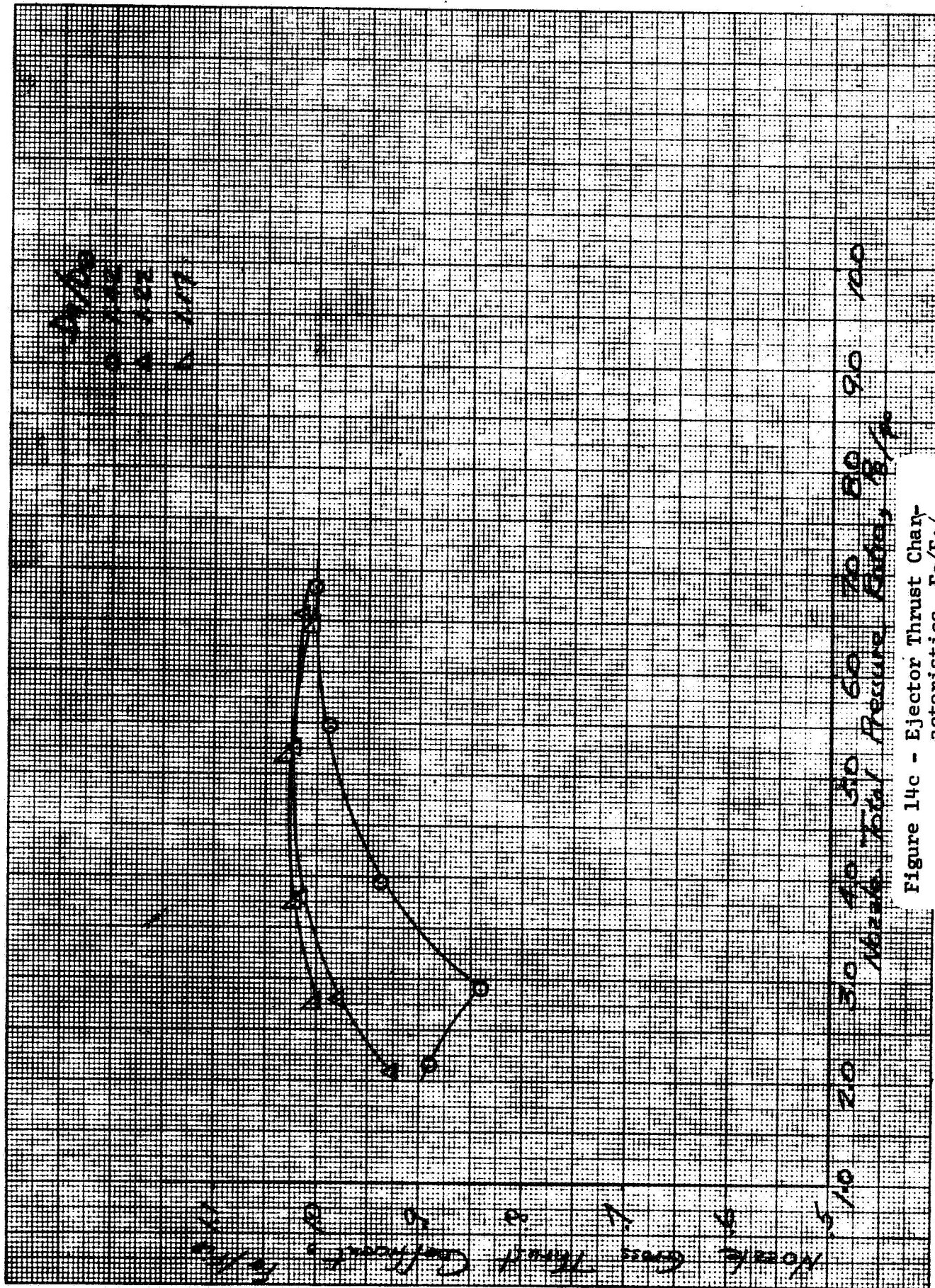


Figure 14c - Ejector Thrust Characteristics, F_g/F_{ip} ; Ejector 1 $W/P = .06$

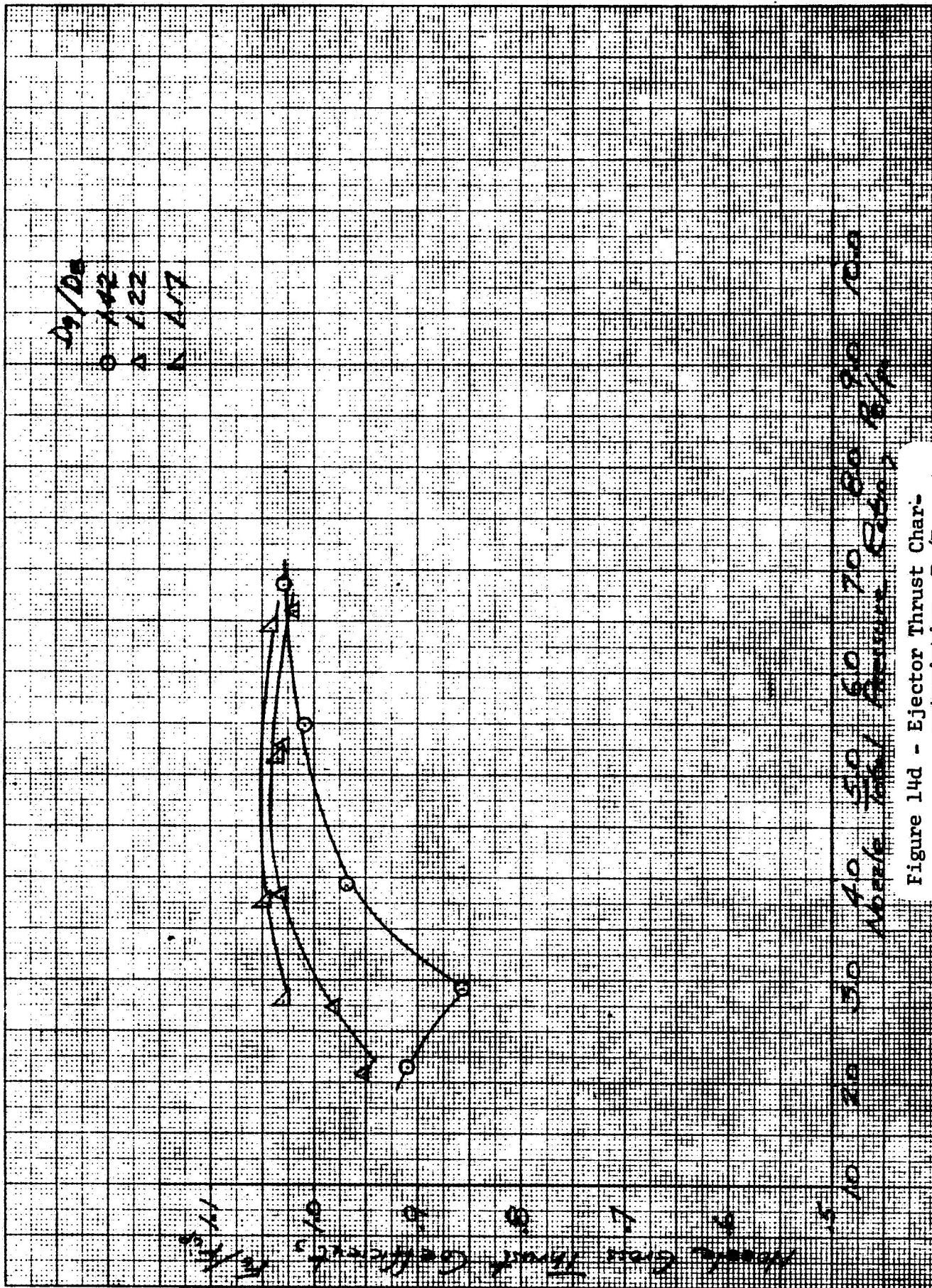


Figure 14d - Ejector Thrust Characteristics, F_{ip}/F_{ip} , Ejector 1 $W/F_{ip} = 0.08$

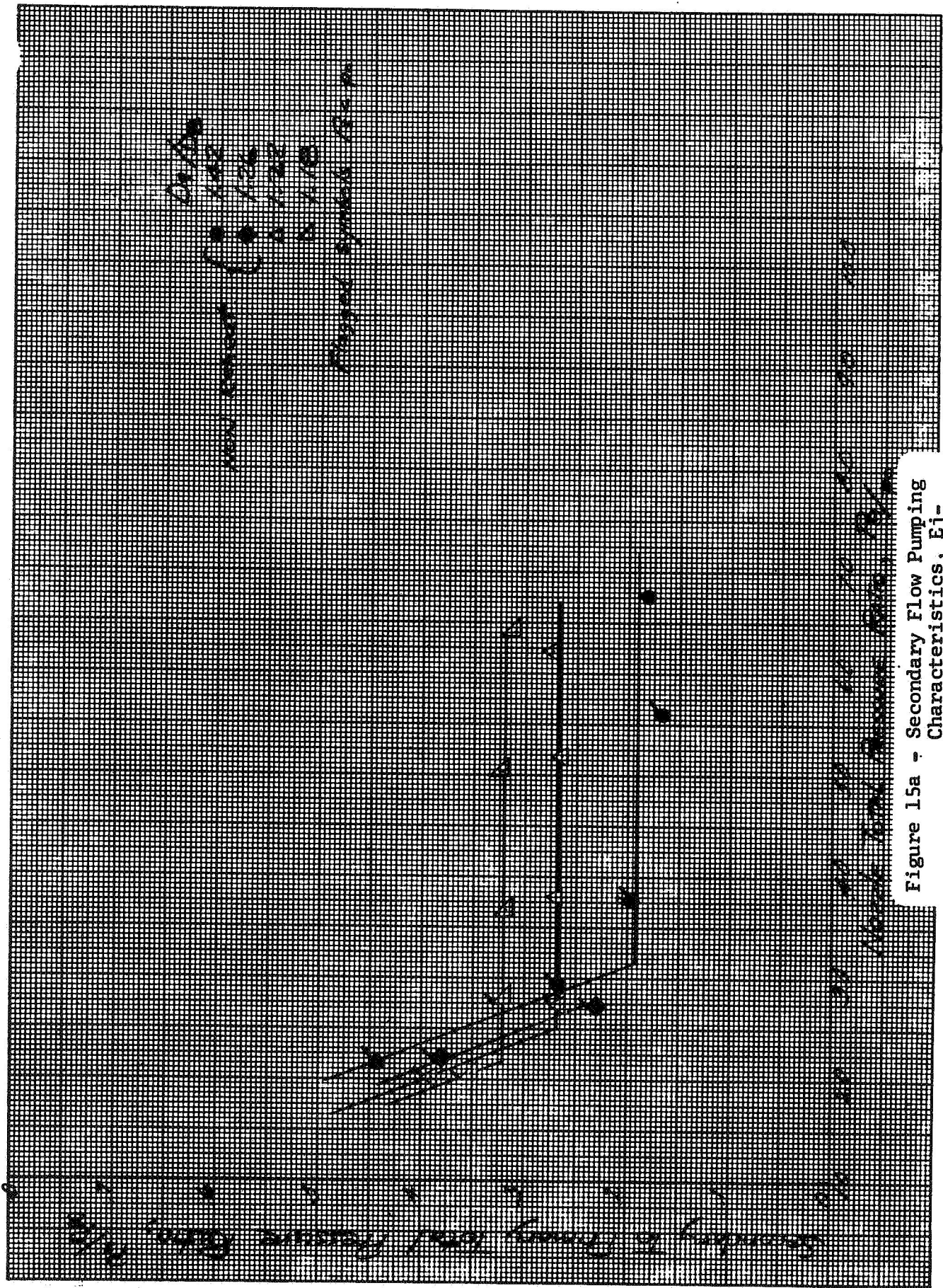


Figure 15a - Secondary Flow Pumping Characteristics, E_j -
ector 2 $\omega\sqrt{t} = 0.02$

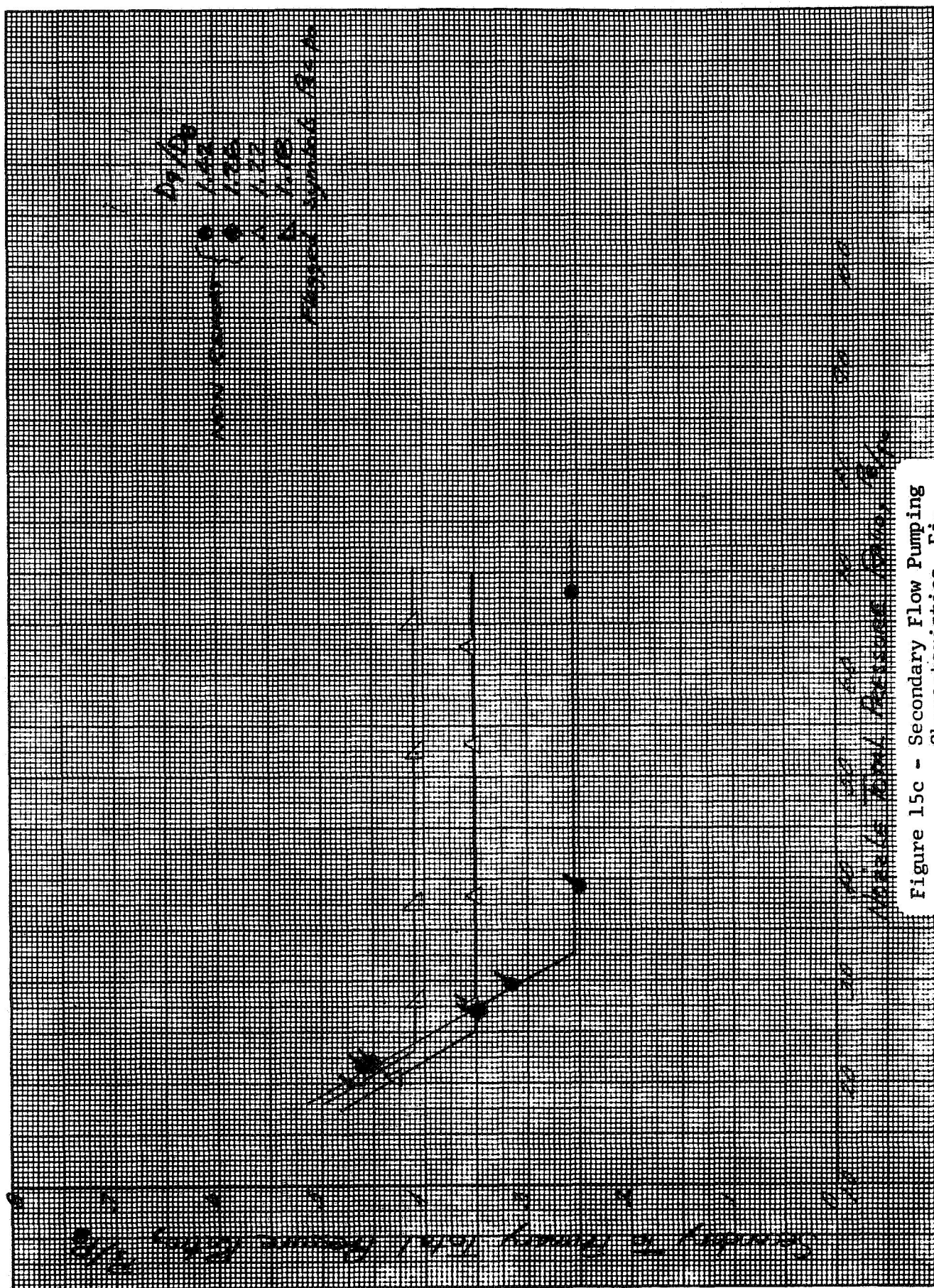


Figure 15c - Secondary Flow Pumping Characteristics, Ej-
ector 2 $W/\sqrt{T} = .06$

Secondary to Primary Total Pressure Ratio, P_2/P_1



Flow Rate (GPM)

Figure 15d - Secondary Flow Pumping Characteristics, Ejector 2 $W/F = .08$

W/F = .08
 W/F = .10
 W/F = .12
 W/F = .14
 W/F = .16

Pressure Ratio

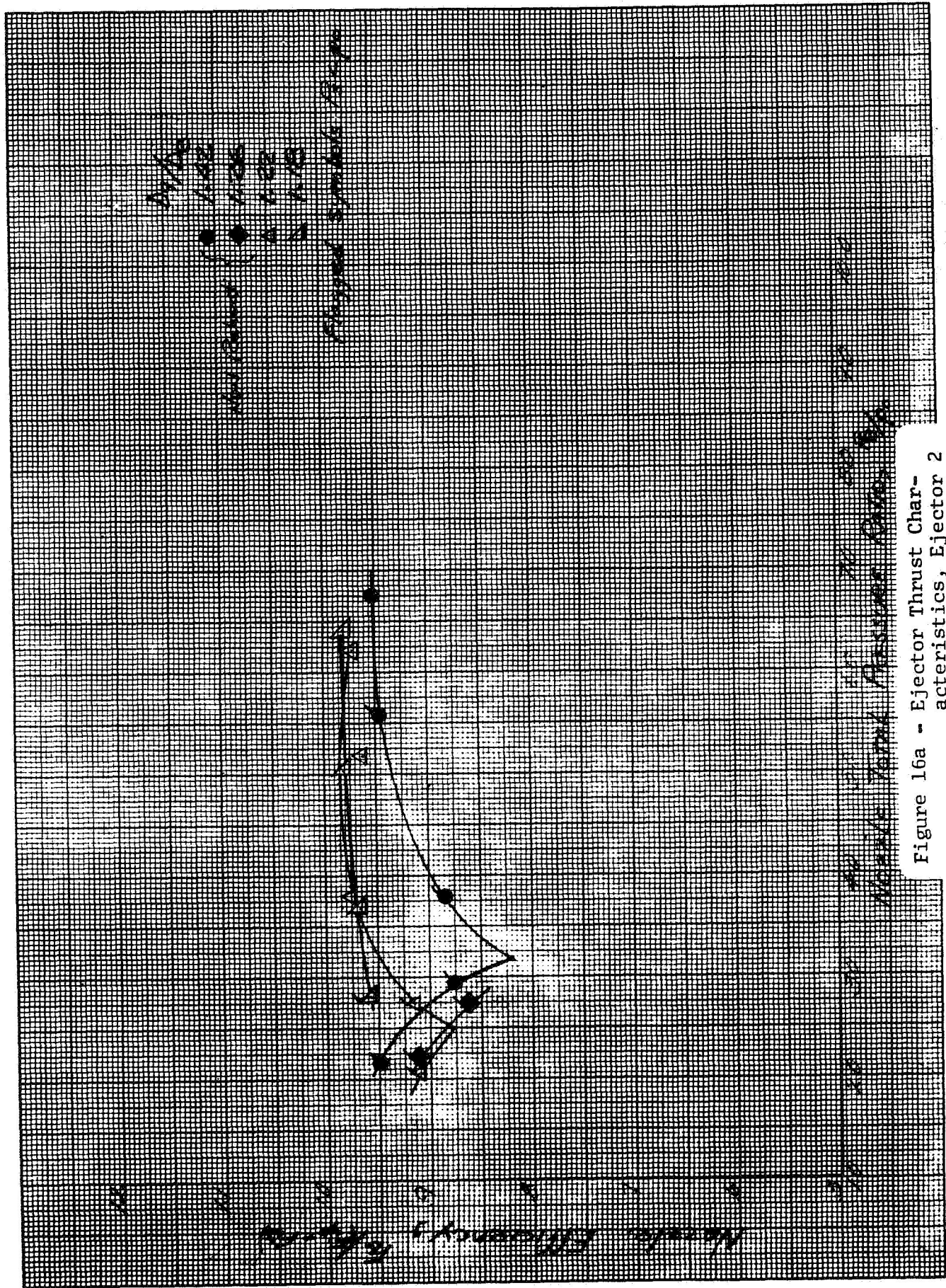


Figure 16a - Ejector Thrust Characteristics, Ejector 2
 $\omega \sqrt{T} = .02$

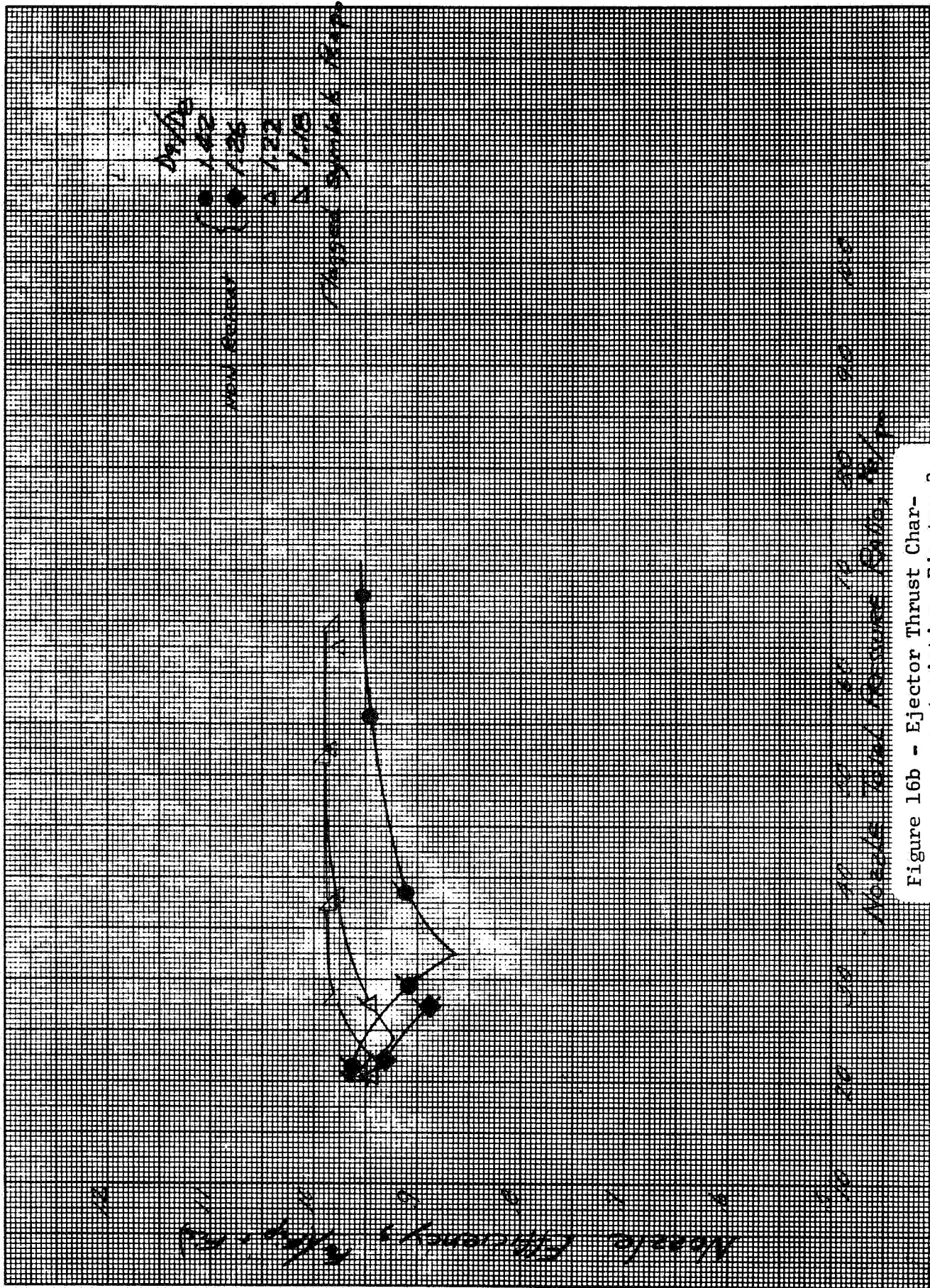
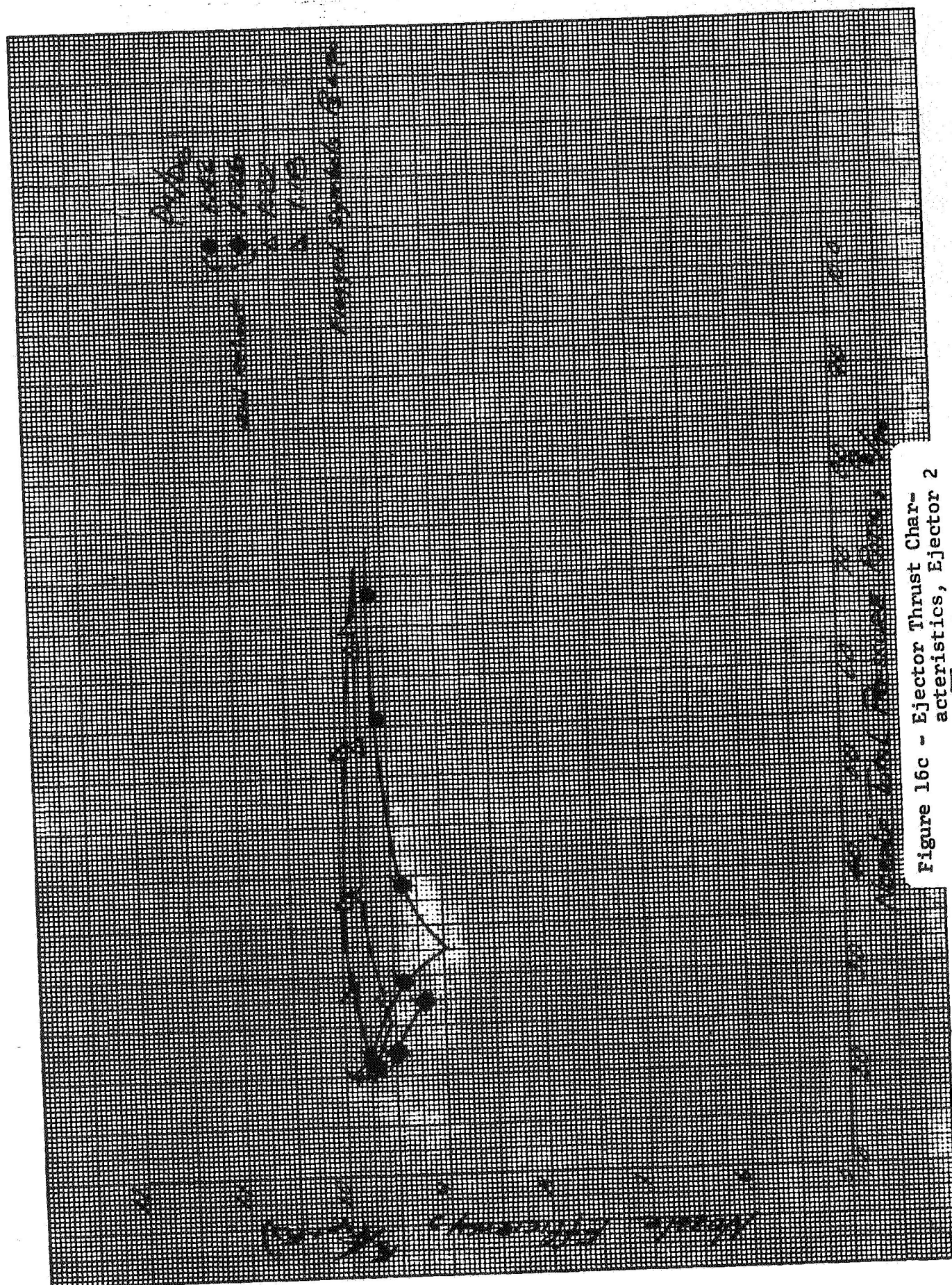
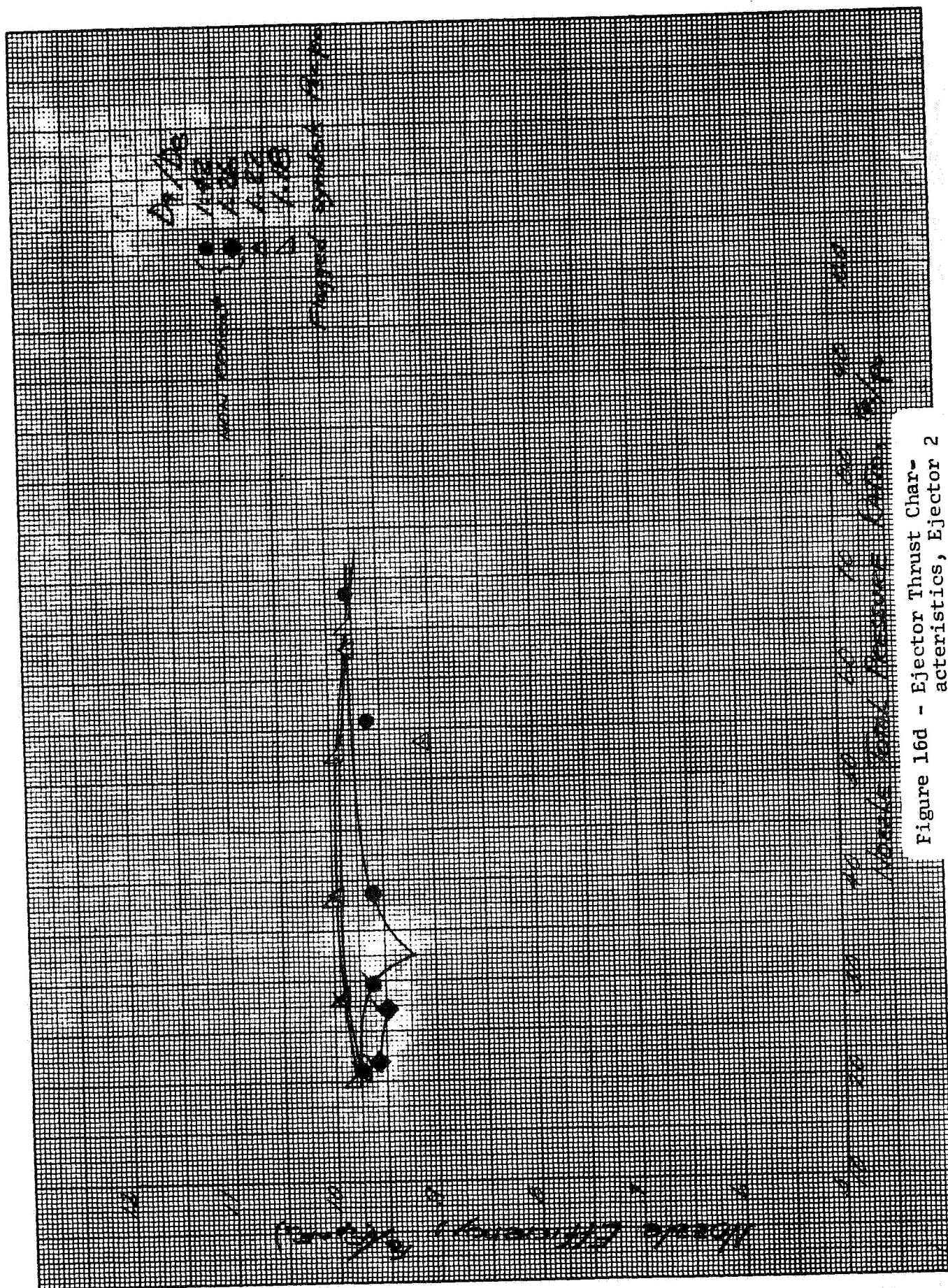


Figure 16b - Ejector Thrust Characteristics, Ejector 2

$$\omega/P = .04$$




$$WVZ = .08$$

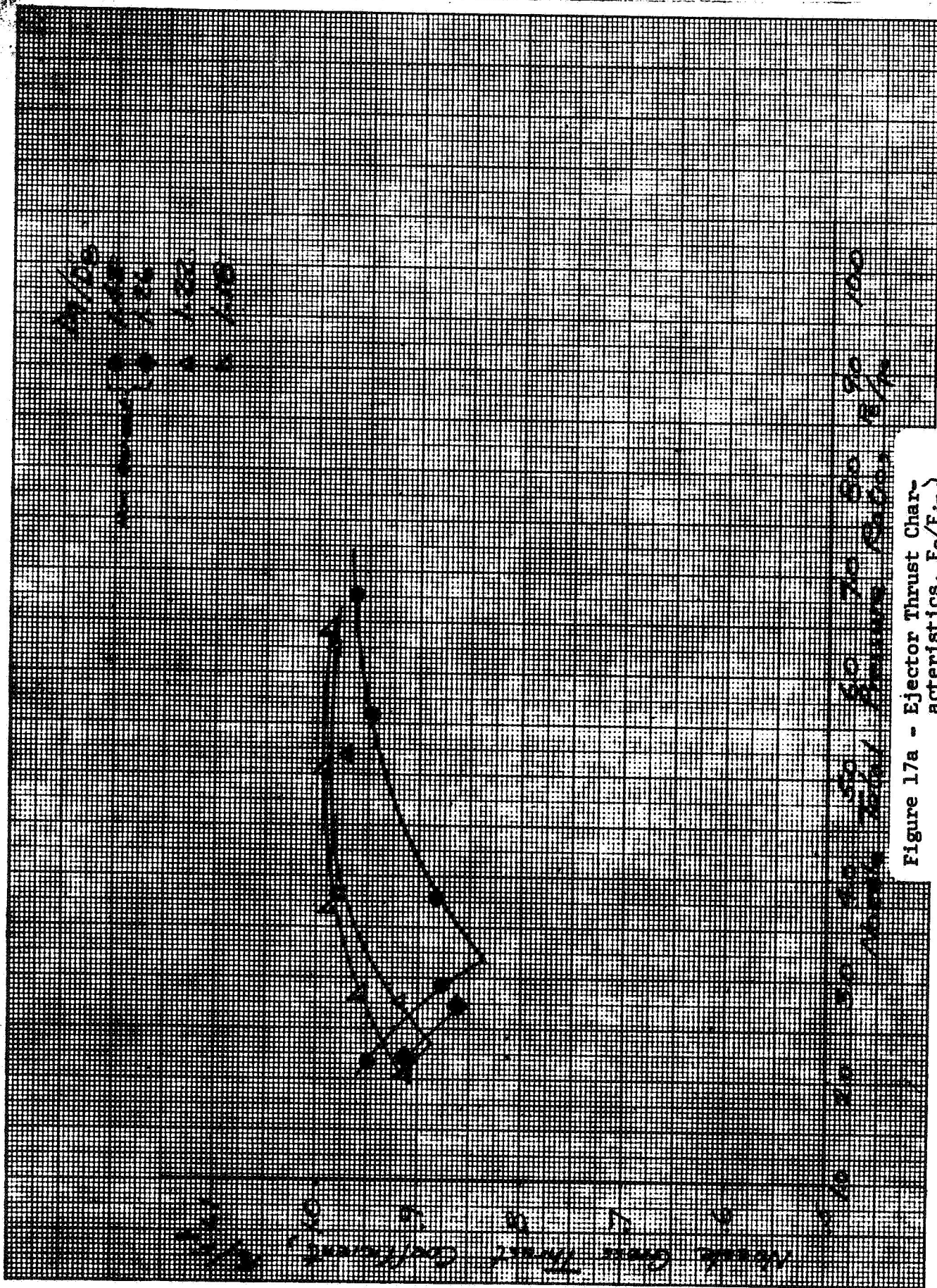


Figure 17a - Ejector Thrust Characteristics, F_G/F_{ip}
Ejector 2 $\omega/\sqrt{\gamma} = 0.02$

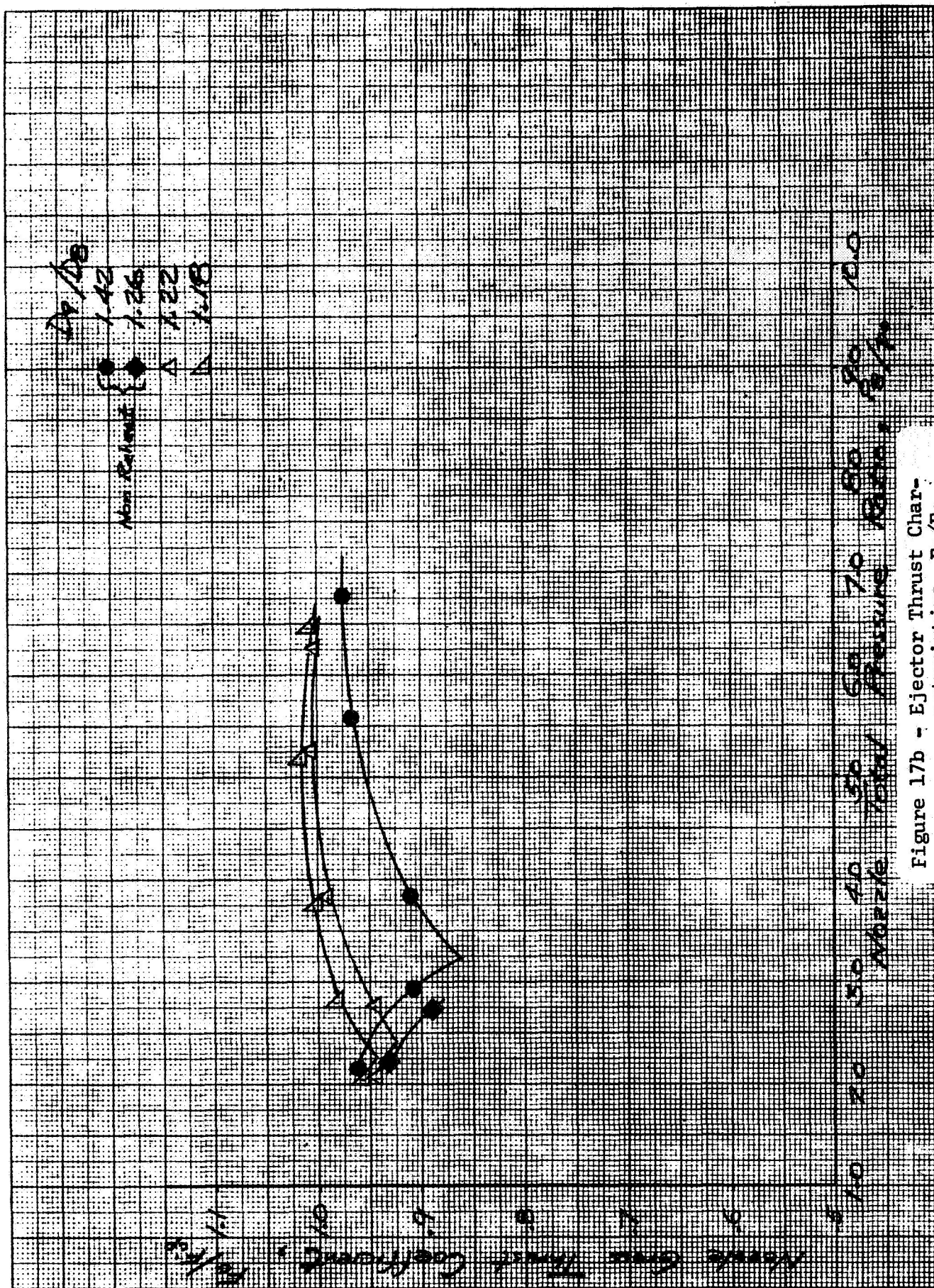


Figure 17b - Ejector Thrust Characteristics, F_G/F_{ip} , Ejector 2 $\omega/\sqrt{2} = .04$

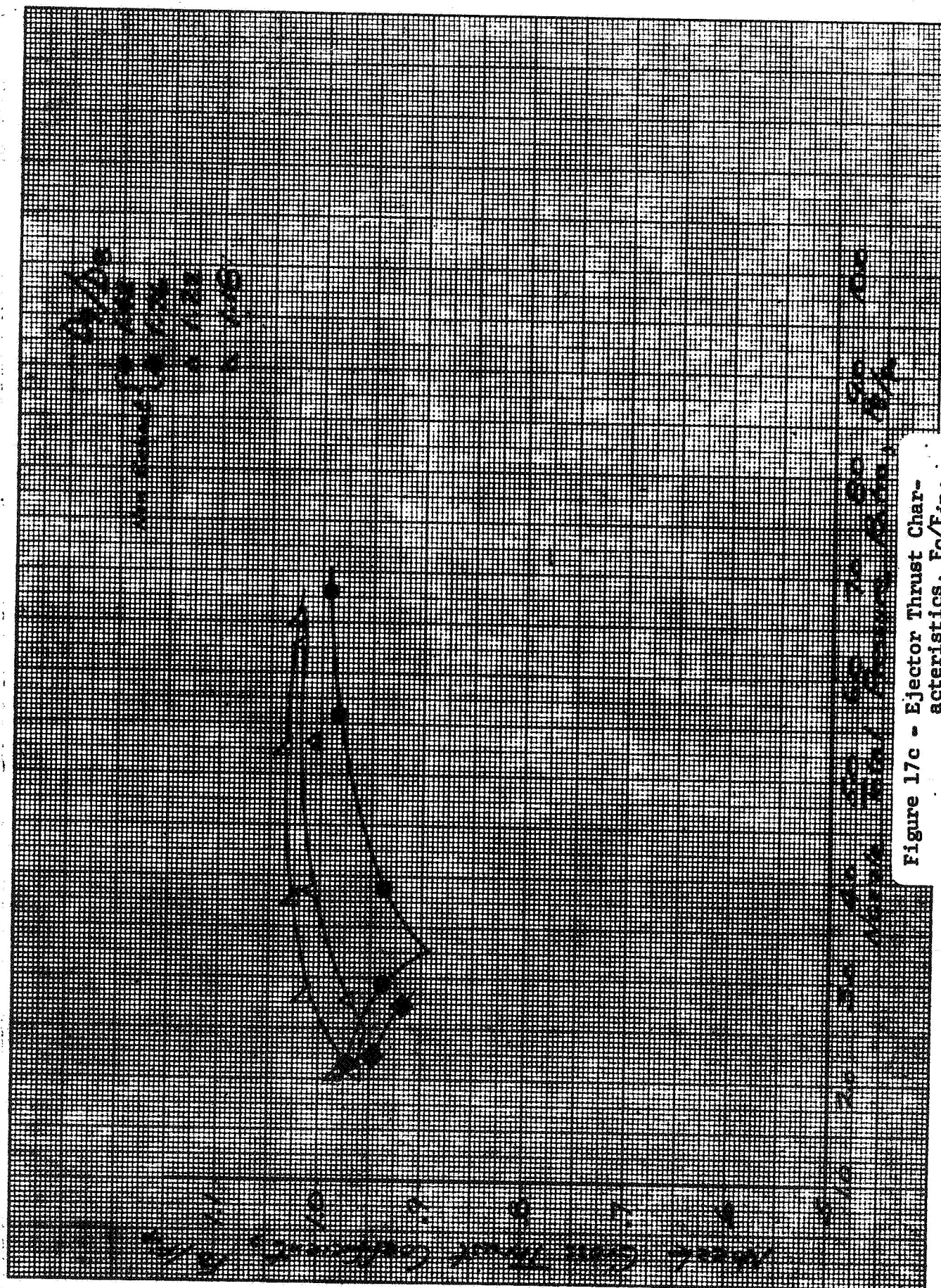


Figure 17c - Ejector Thrust Characteristics, FG/Fip, Ejector 2 *W/F₂ = .04*

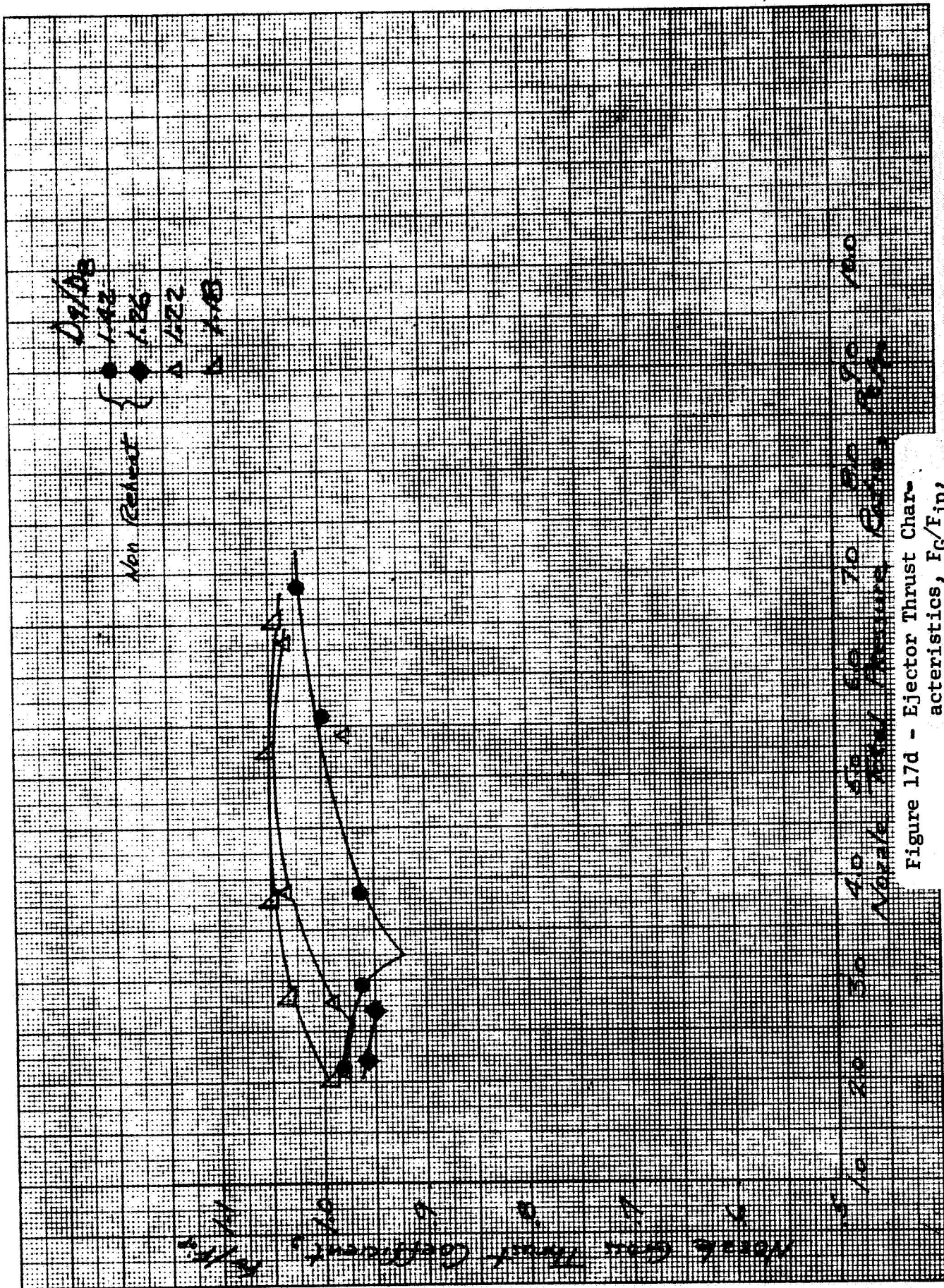


Figure 17d - Ejector Thrust Characteristics, F_G/F_{ip} , Ejector 2 $\omega/\sqrt{2} = 0.08$

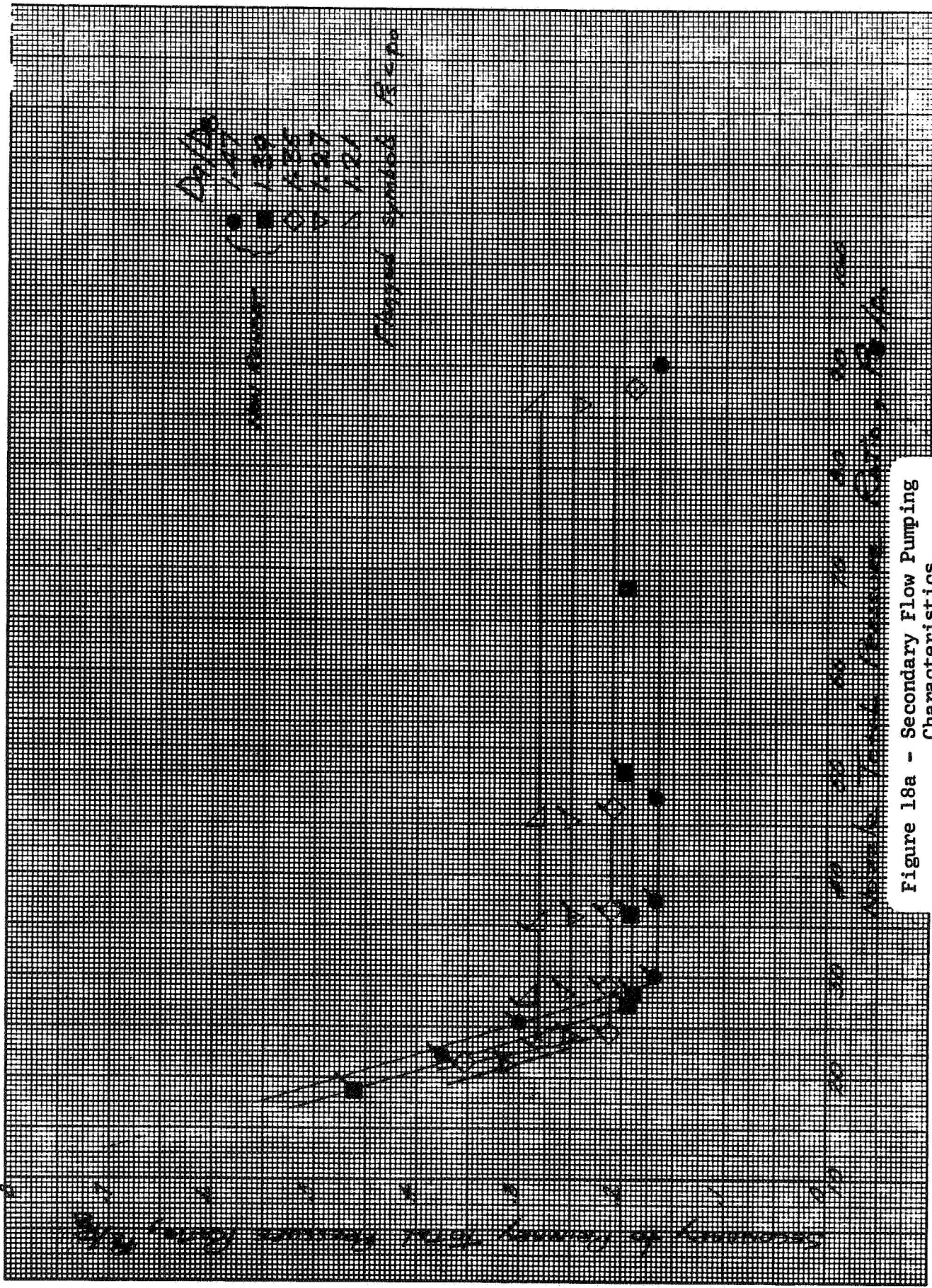


Figure 18a - Secondary Flow Pumping Characteristics, Ejector 3 $W/F = .02$

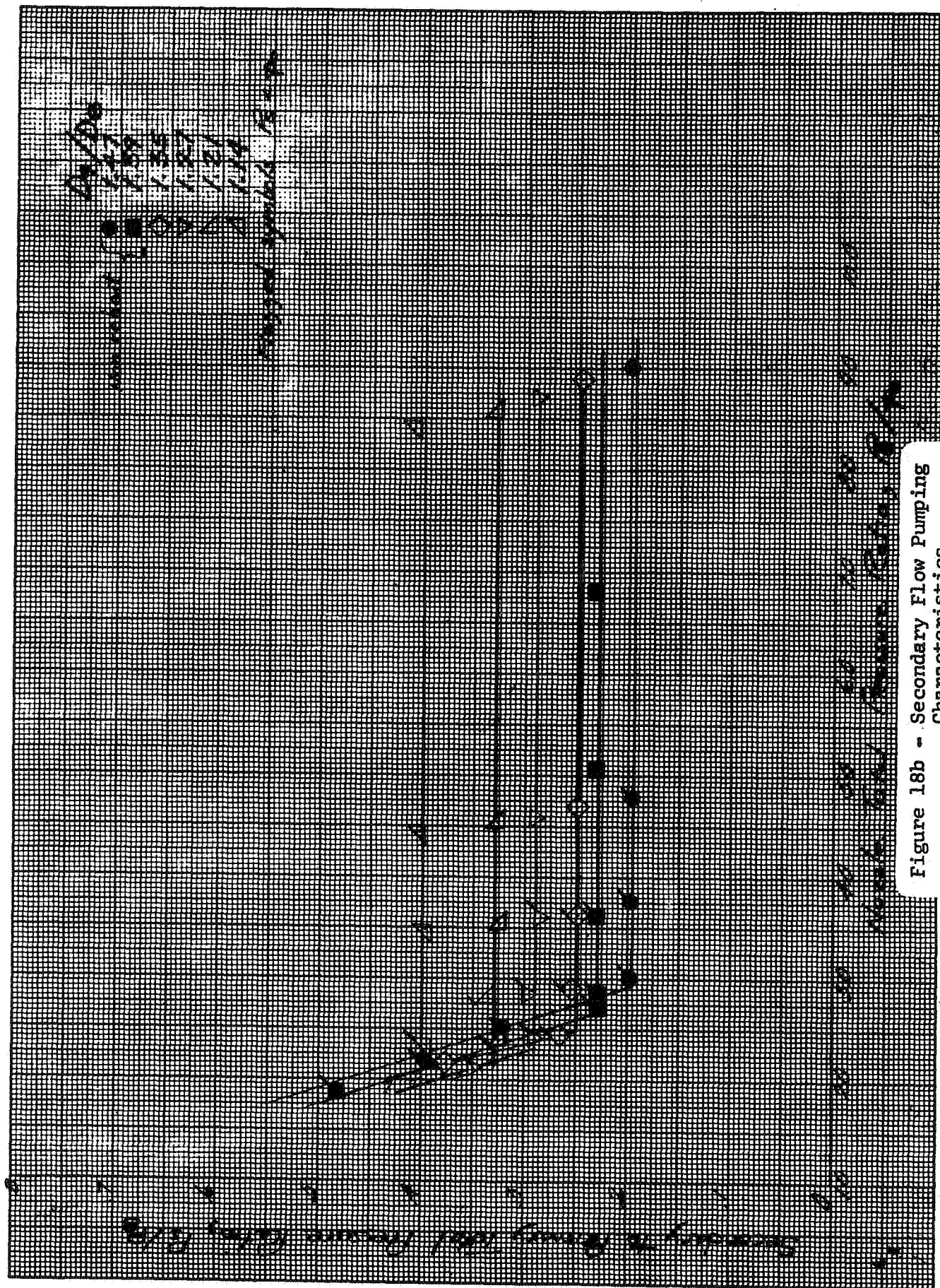


Figure 18b - Secondary Flow Pumping Characteristics, Ejector 3 $\omega/\sqrt{\tau} = 0.4$

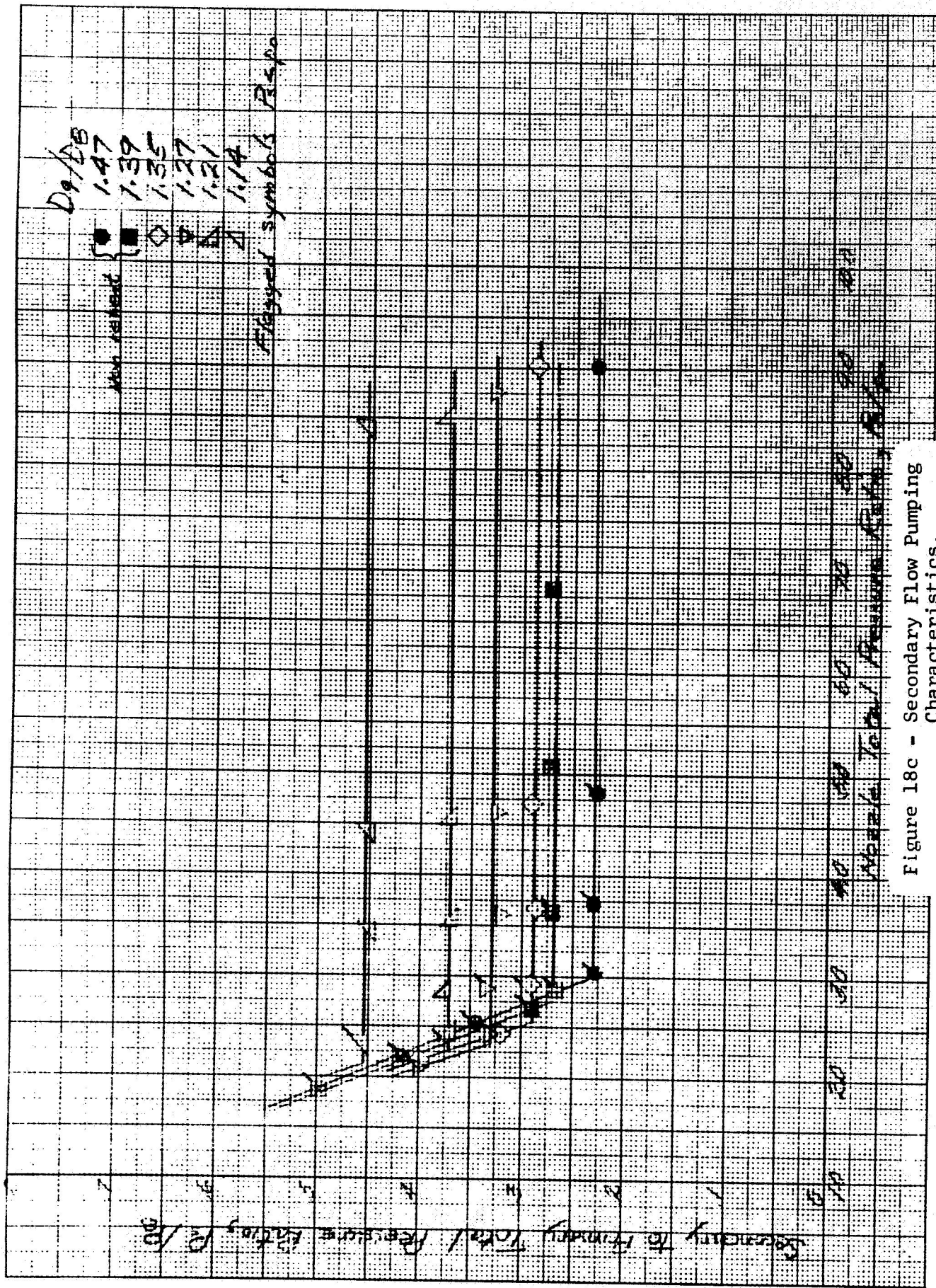


Figure 18c - Secondary Flow Pumping
 Characteristics,
 Ejector 3 $\omega/P_2 = .06$

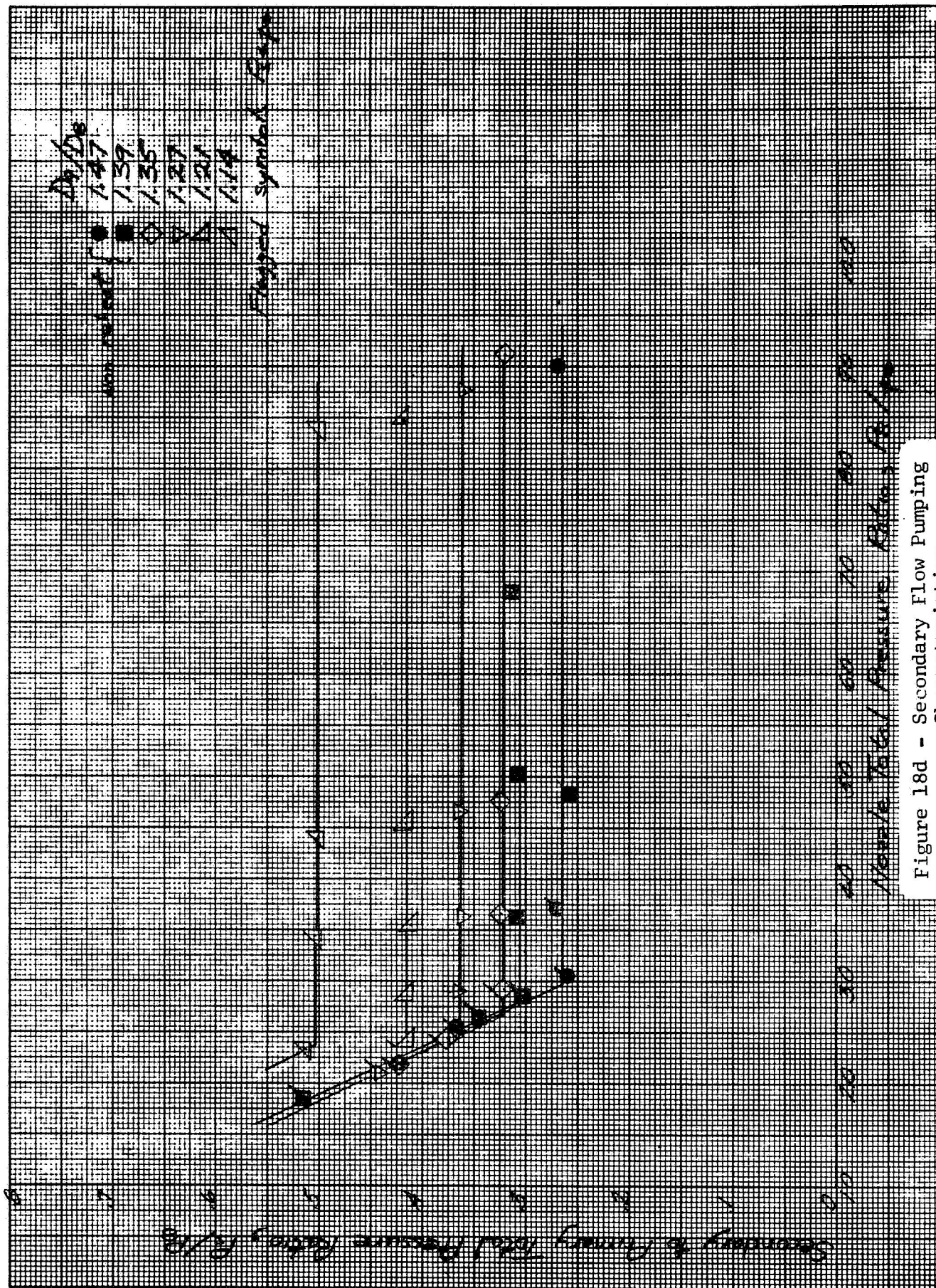


Figure 18d - Secondary Flow Pumping Characteristics, Ejector 3 WPT-08

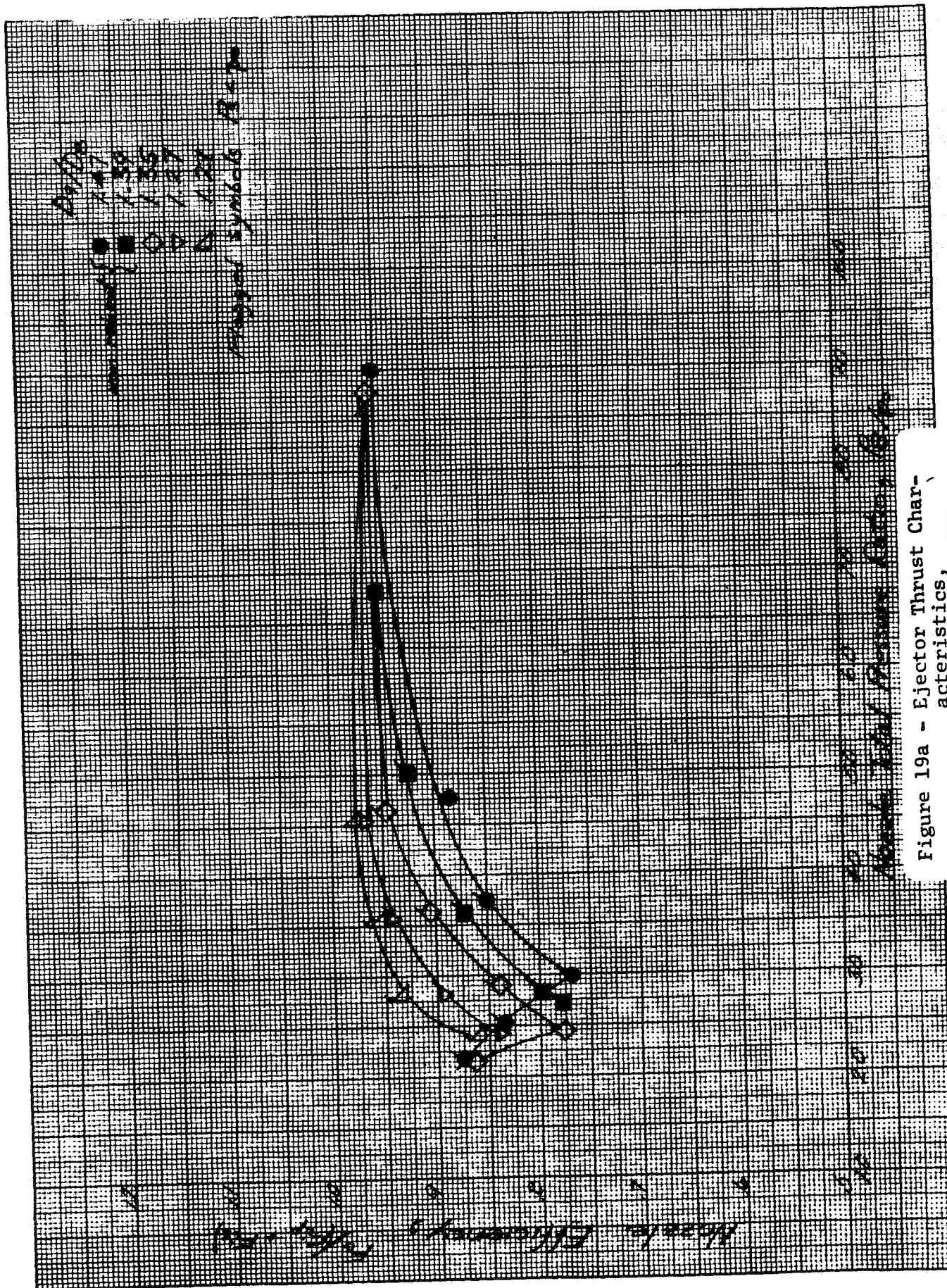


Figure 19a - Ejector Thrust Characteristics, Ejector 3 $W\sqrt{T_1} = 0.2$

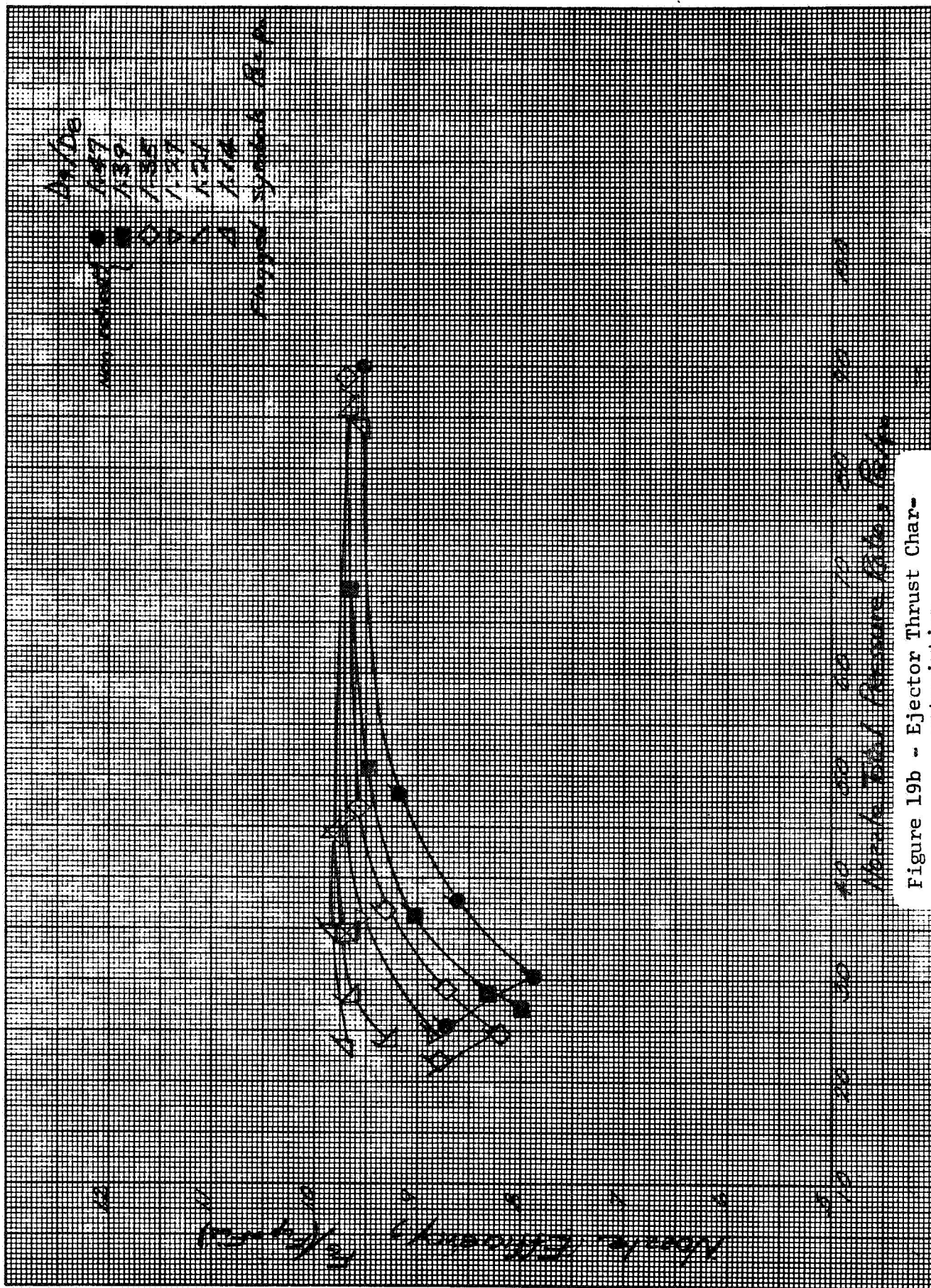


Figure 19b - Ejector Thrust Characteristics, Ejector 3 $\omega\sqrt{\tau} = .04$

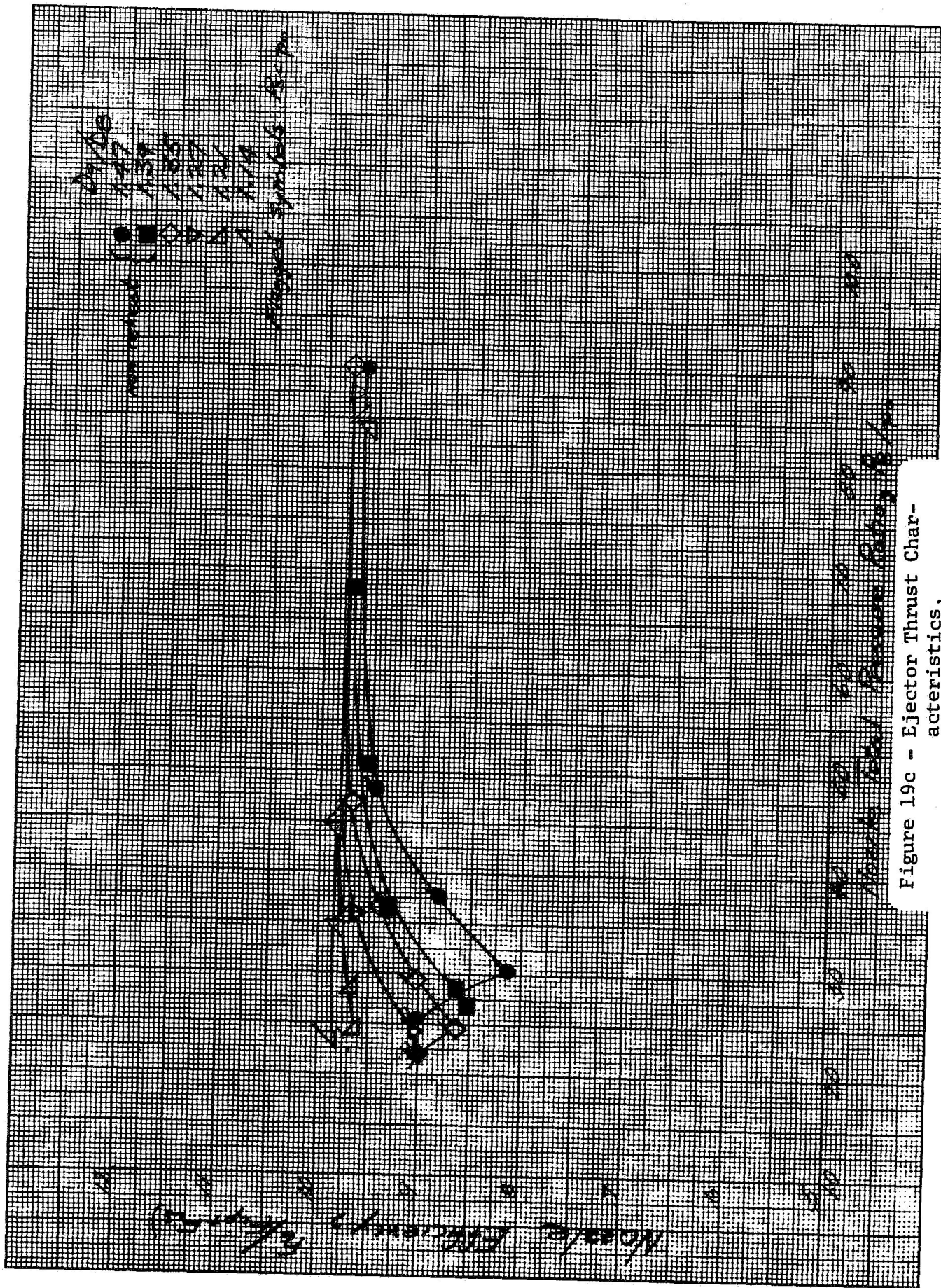


Figure 19c - Ejector Thrust Characteristics,
Ejector 3 $\omega/P_0 = 0.6$

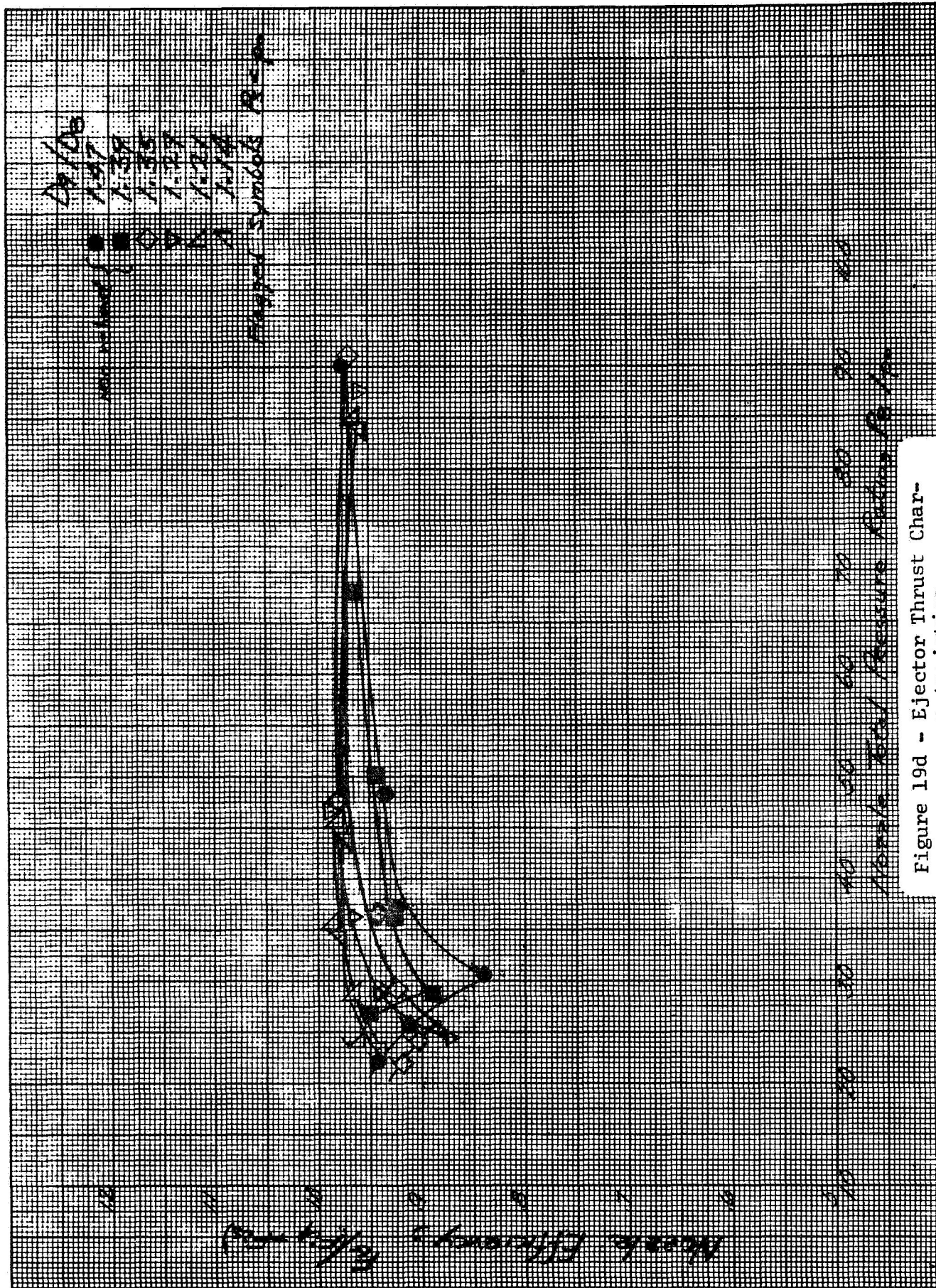


Figure 19d - Ejector Thrust Characteristics, Ejector 3 WJ-08

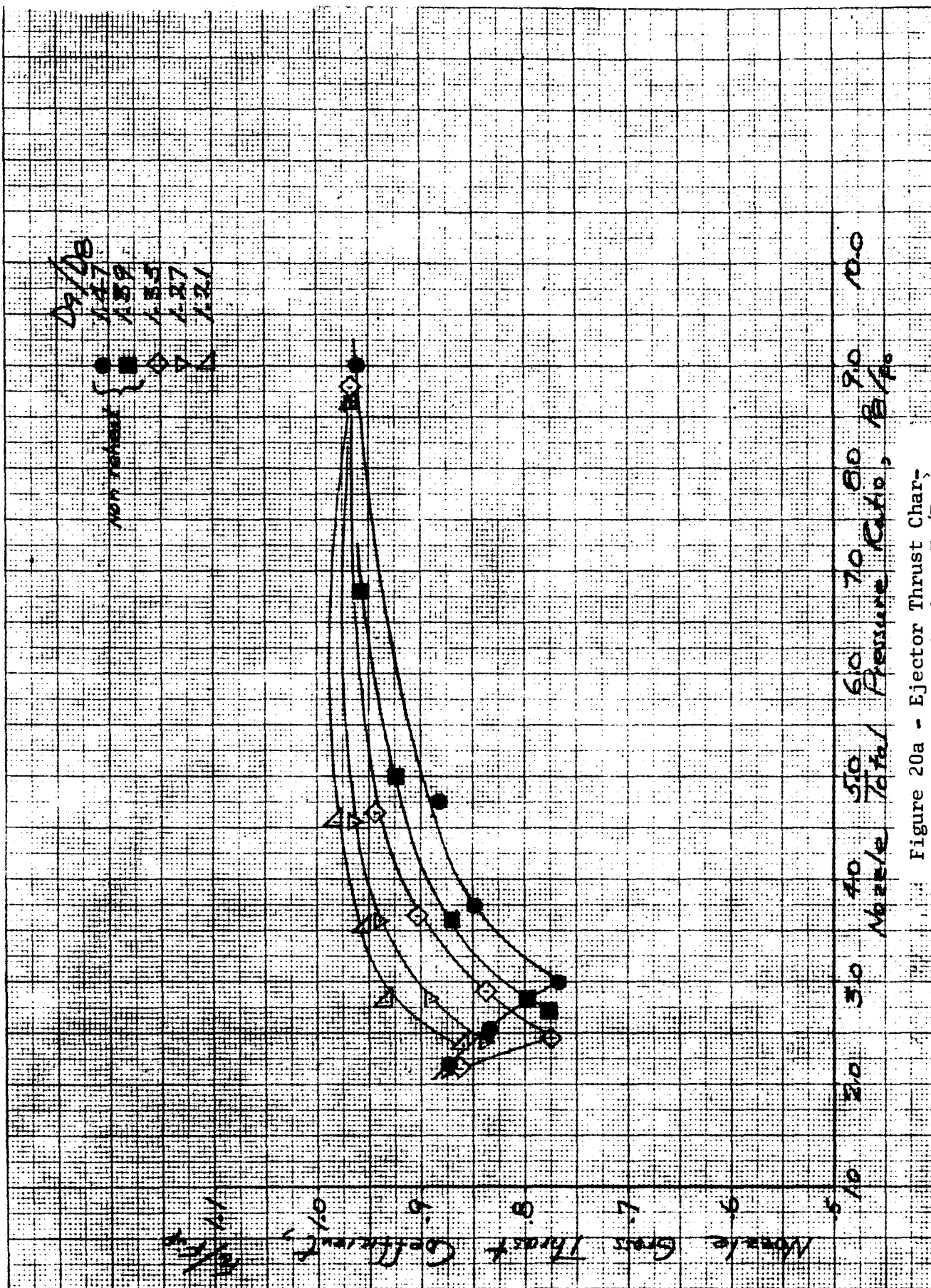


Figure 20a - Ejector Thrust Characteristics, $F_{G/Fip}$, Ejector 3 $W/P = .02$

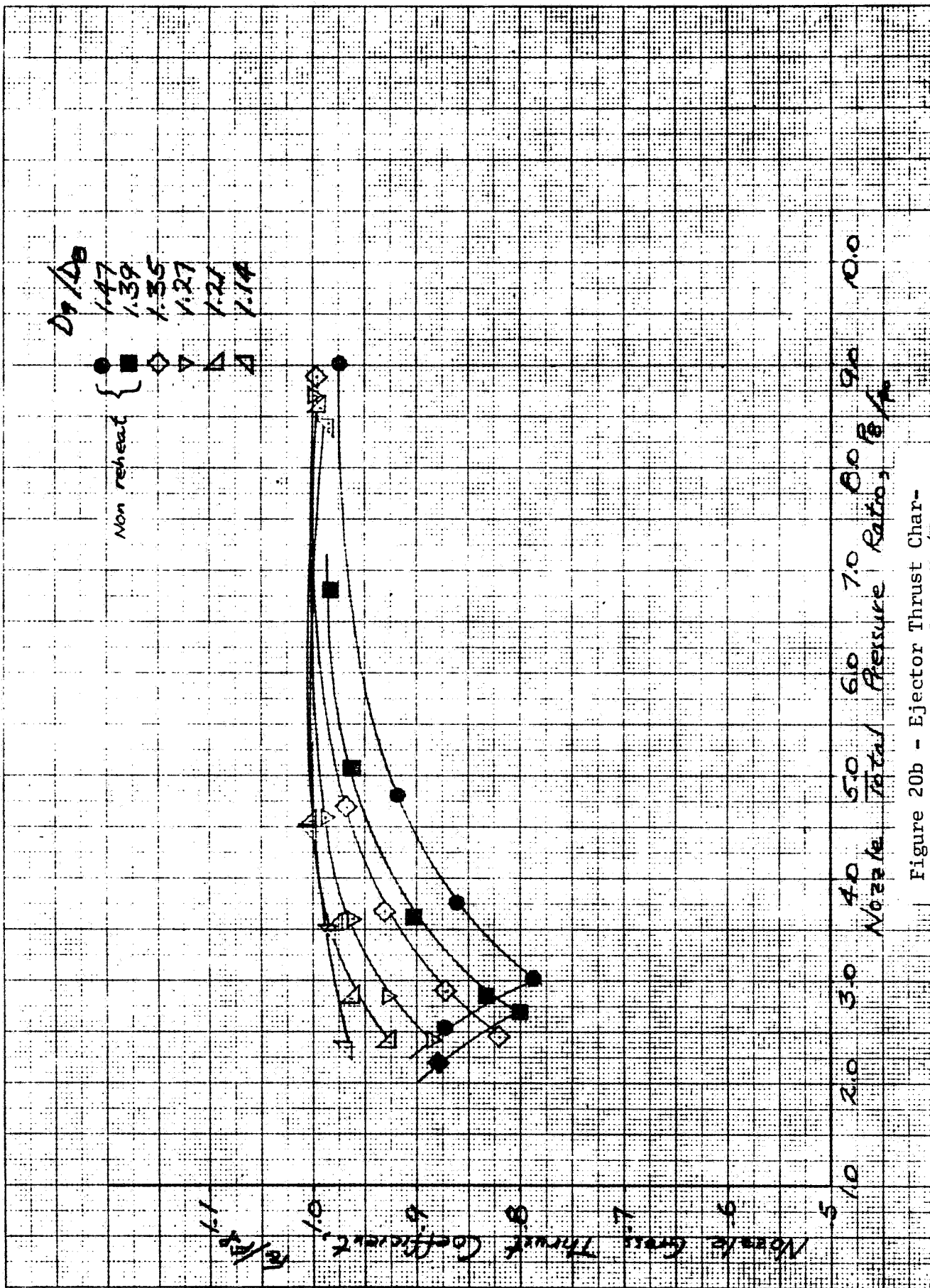


Figure 20b - Ejector Thrust Characteristics, P_0/P_a , Ejector 3 $WUE = 0.04$

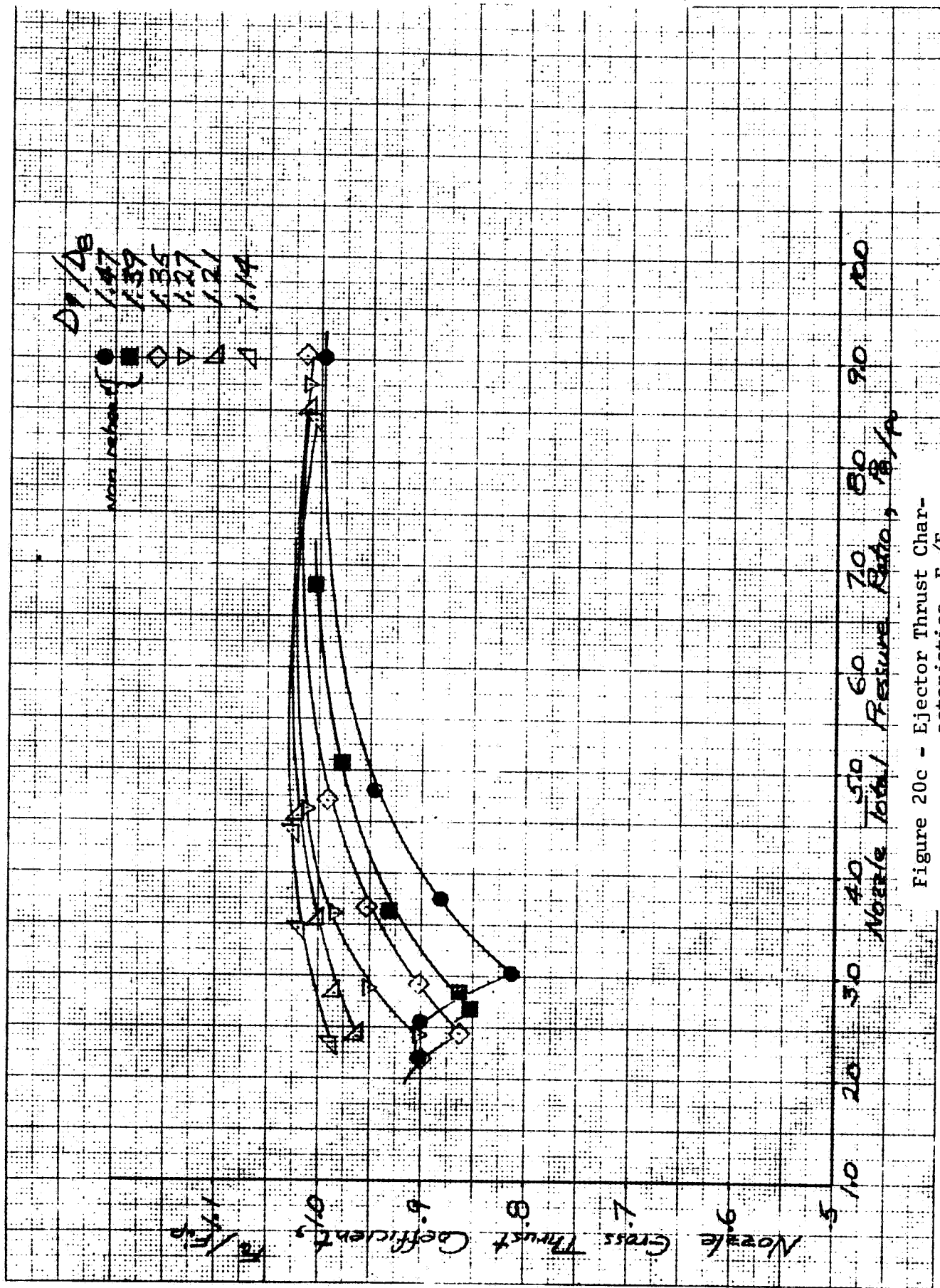


Figure 20c - Ejector Thrust Characteristics, F_G/F_{ip} , Ejector 3 $WPR=0.06$

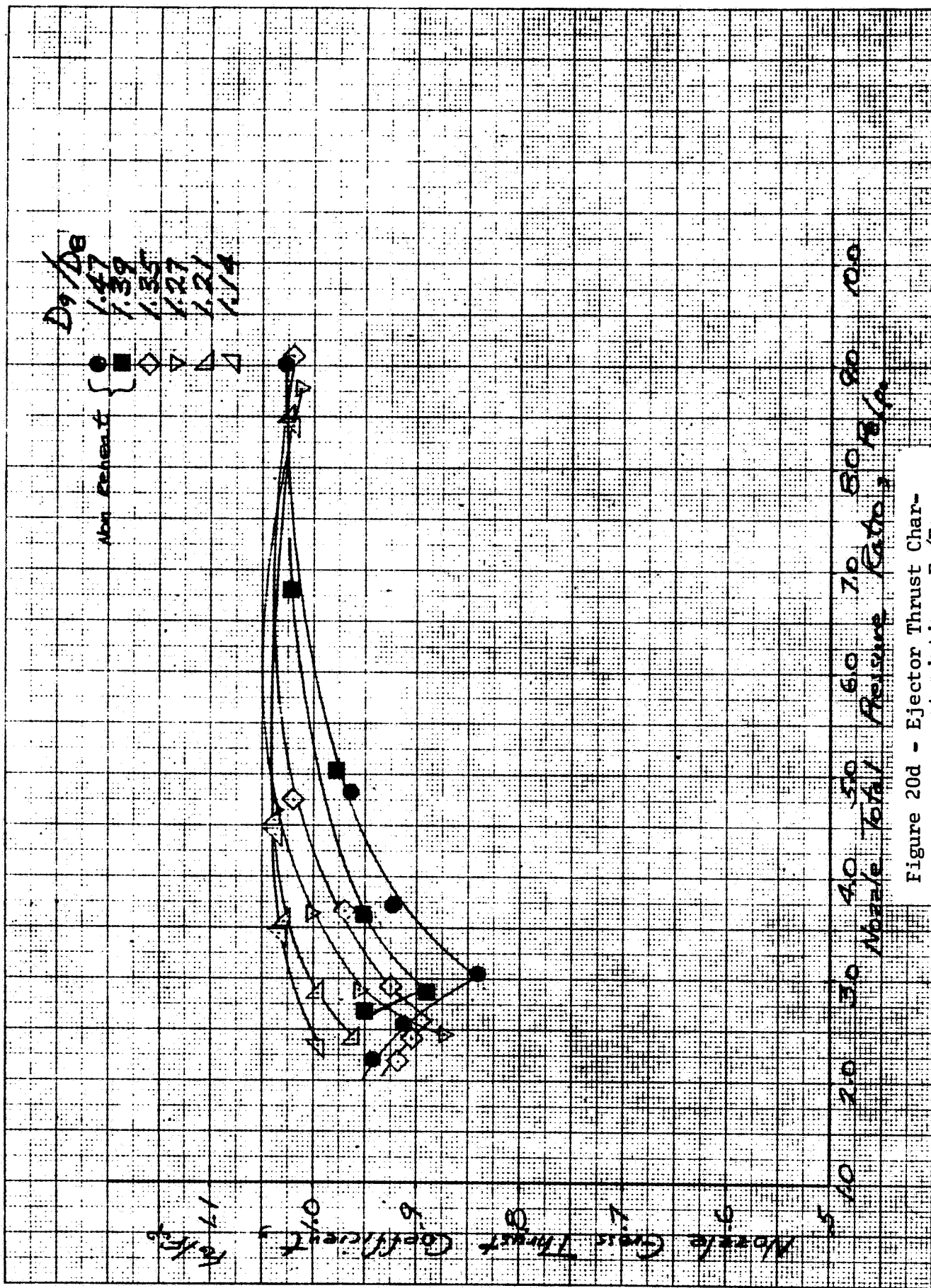
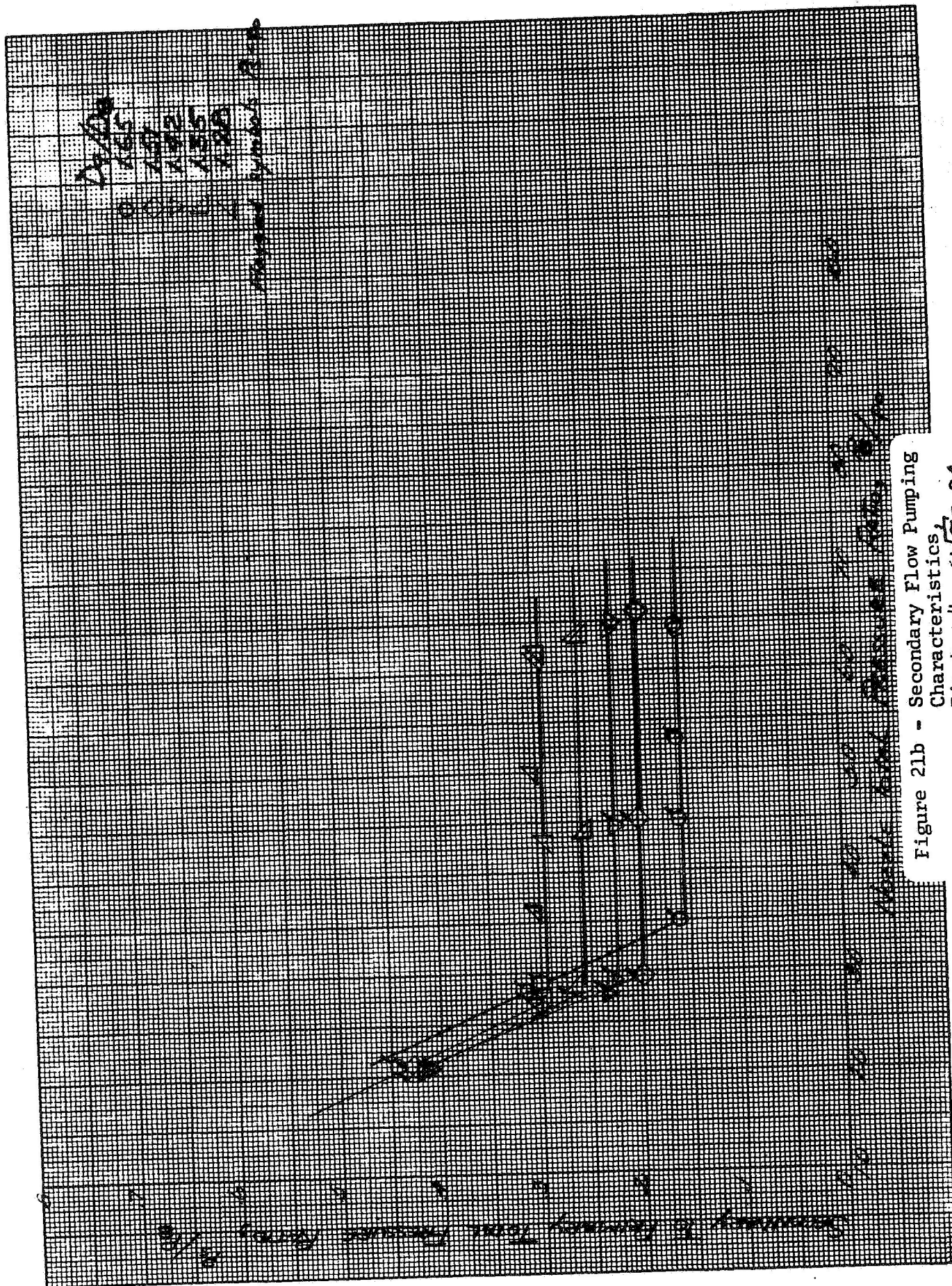


Figure 20d - Ejector Thrust Characteristics, F_G/F_{ip} , Ejector 3 $W/F = 0.08$



Date
 1/6/60
 1/6/60
 1/6/60
 1/6/60
 1/6/60
 1/6/60

Manual Spanish Room

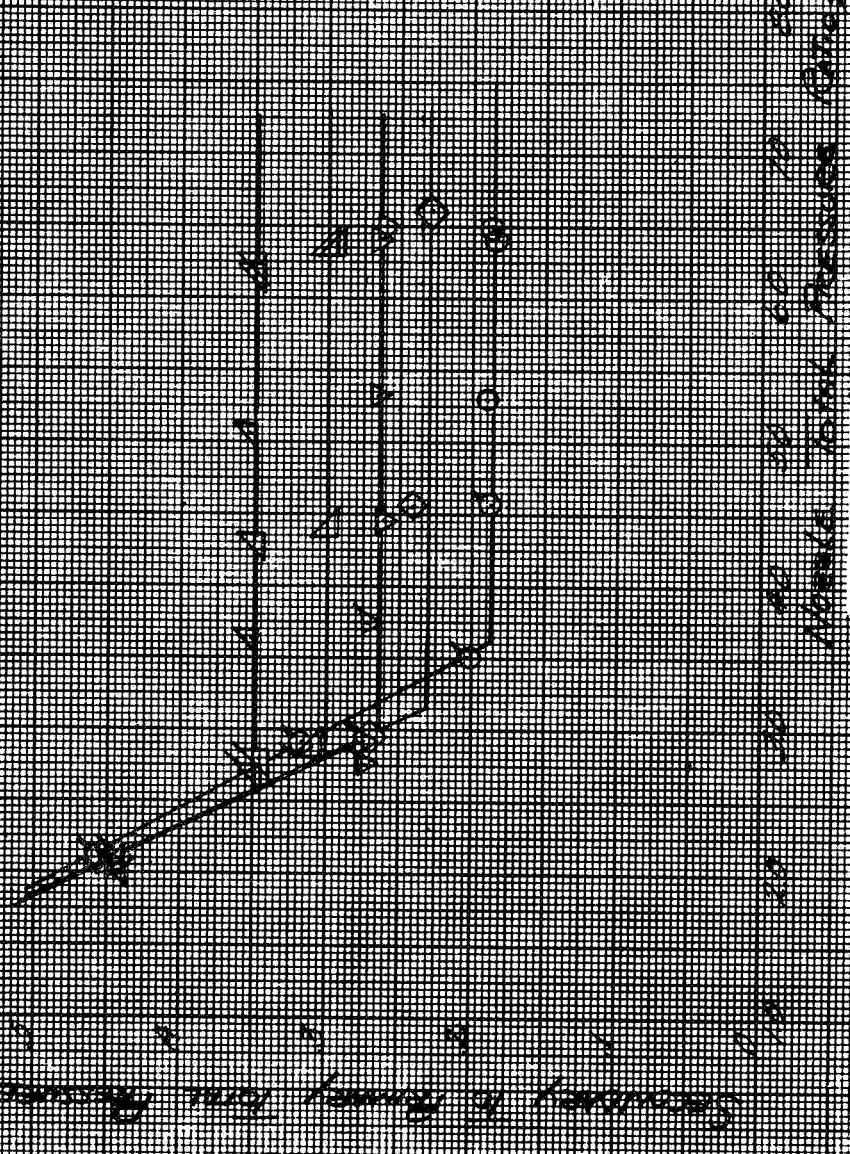


Figure 21c - Secondary Flow Pumping Characteristics, Ejector 4 $\omega\sqrt{\tau} = 0.06$

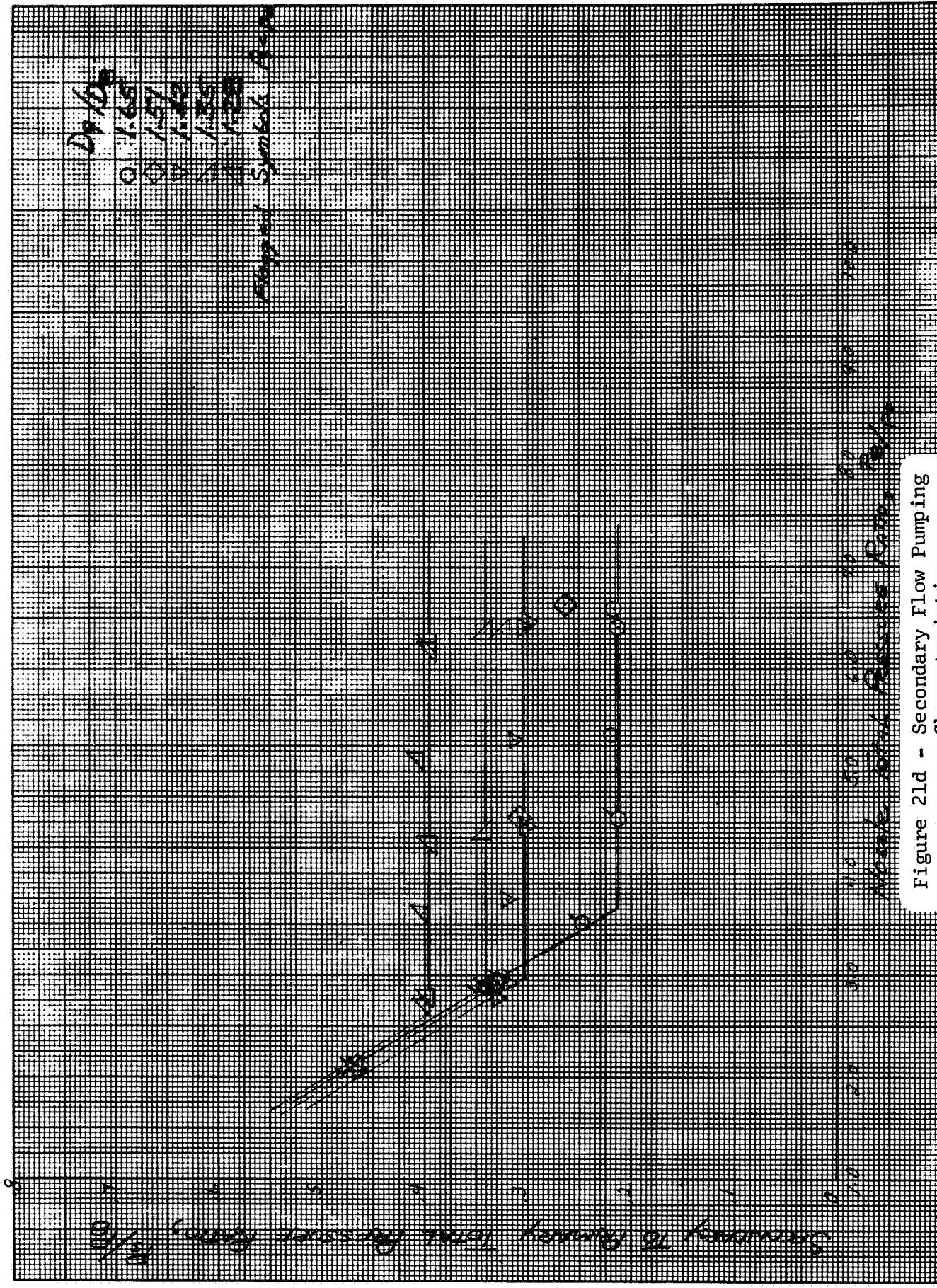
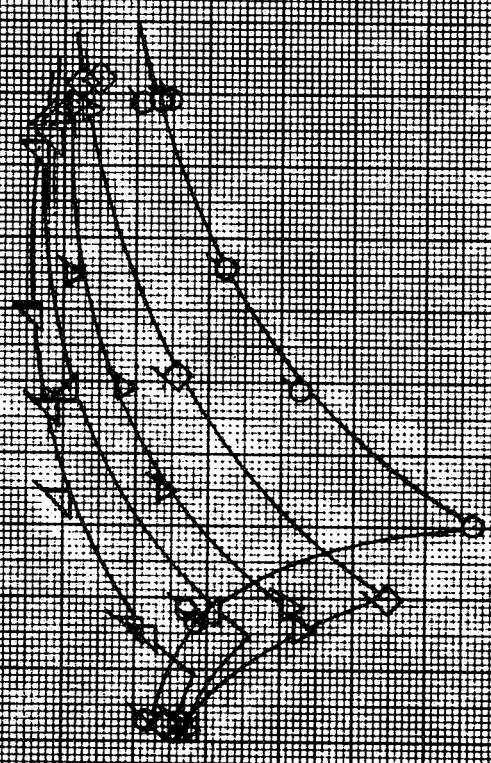


Figure 21d - Secondary Flow Pumping Characteristics, Ejector 4 $\omega\sqrt{Z} = .08$

08/10/58
 08/10/58
 08/10/58
 08/10/58
 08/10/58
 08/10/58

08/10/58
 08/10/58
 08/10/58
 08/10/58
 08/10/58
 08/10/58



Nozzle Thrust, P/P_0
 Nozzle Total Pressure, P/P_0
 Nozzle Total Pressure, P/P_0
 Nozzle Total Pressure, P/P_0
 Nozzle Total Pressure, P/P_0
 Nozzle Total Pressure, P/P_0

Figure 22a - Ejector Thrust Characteristics,
 Ejector 4, $\omega\sqrt{\tau} = .02$

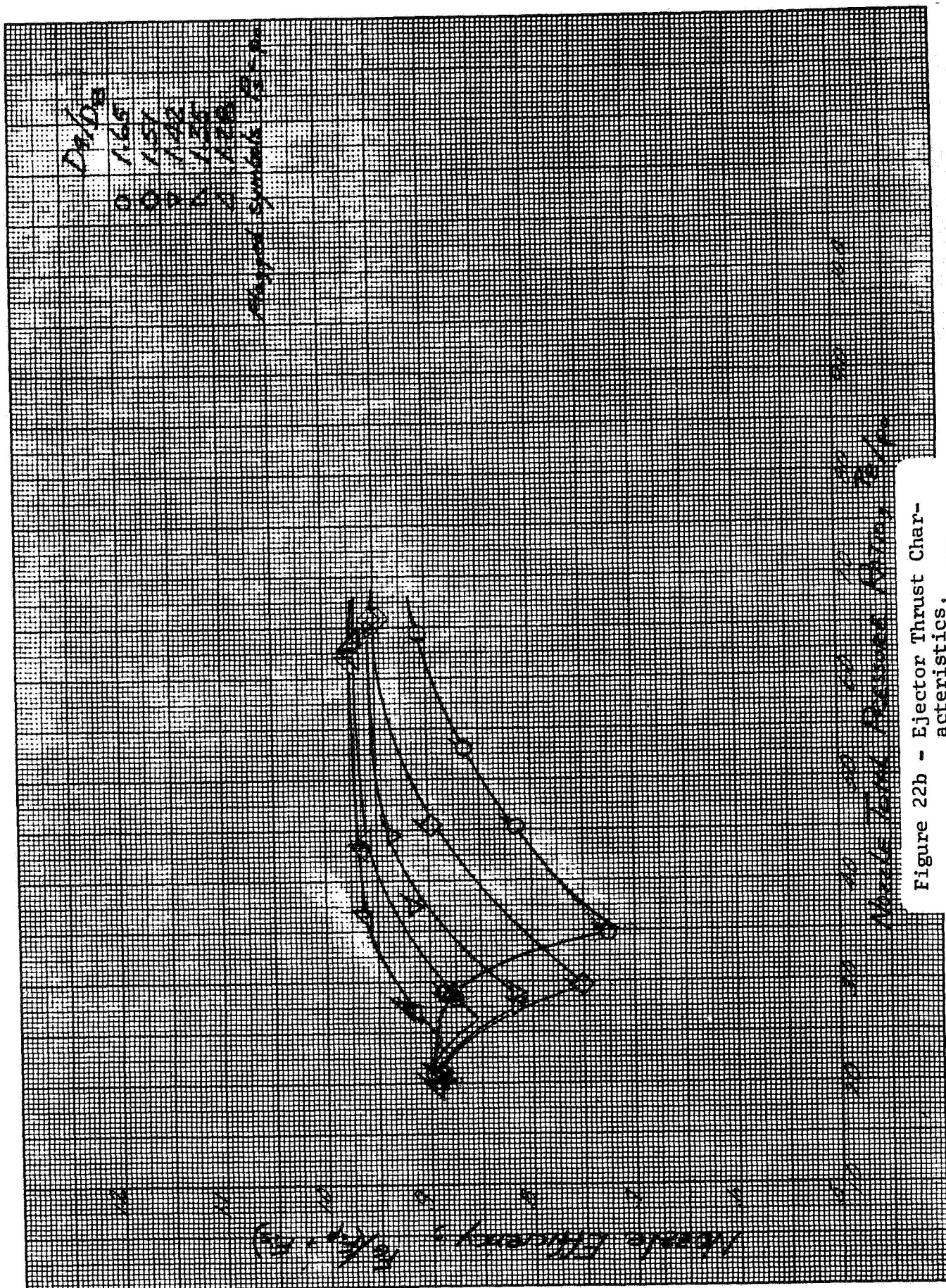
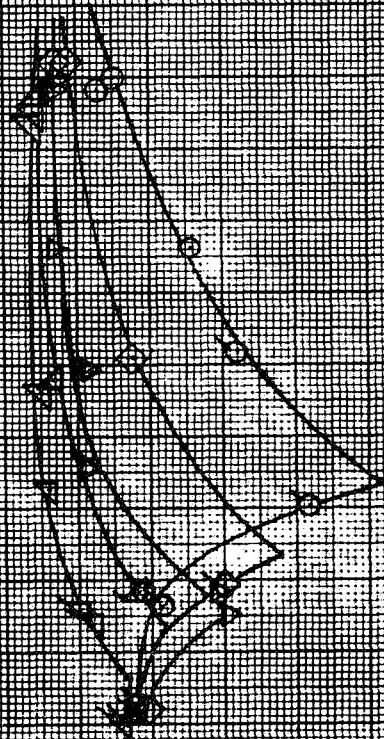


Figure 22b - Ejector Thrust Characteristics, Ejector 4, $\omega\sqrt{T} = .04$

$\frac{P_1}{P_0}$
 1.00
 1.05
 1.10
 1.15
 1.20

Assigned Symbols: S.P.



1.00
 1.05
 1.10
 1.15
 1.20
 1.25
 1.30
 1.35
 1.40
 1.45
 1.50
 1.55
 1.60
 1.65
 1.70
 1.75
 1.80
 1.85
 1.90
 1.95
 2.00

Figure 22c - Ejector Thrust Characteristics,
 Ejector 4 $\omega \sqrt{T} = .06$

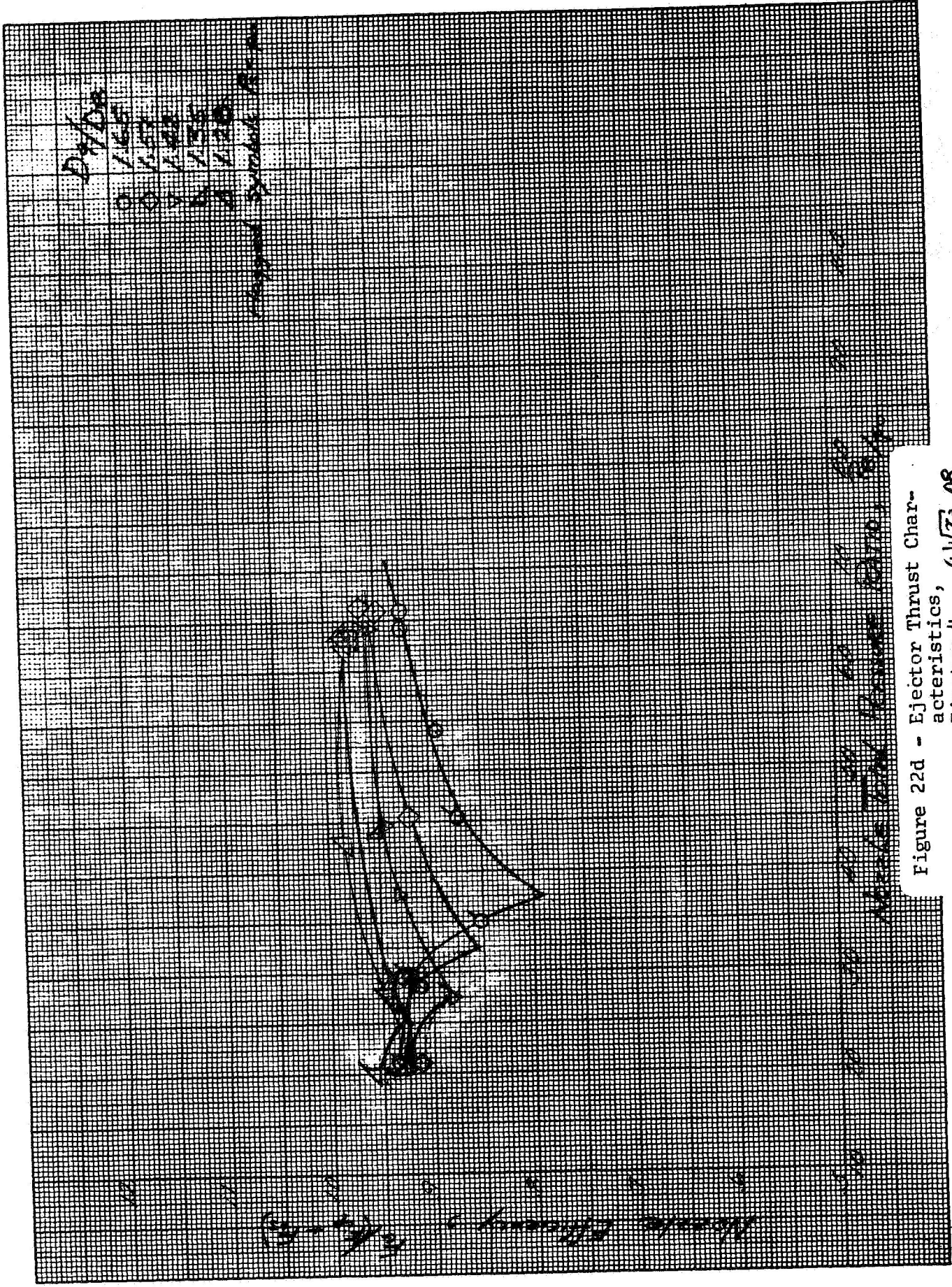


Figure 22d - Ejector Thrust Characteristics, $\omega \sqrt{r} = .08$
Ejector 4

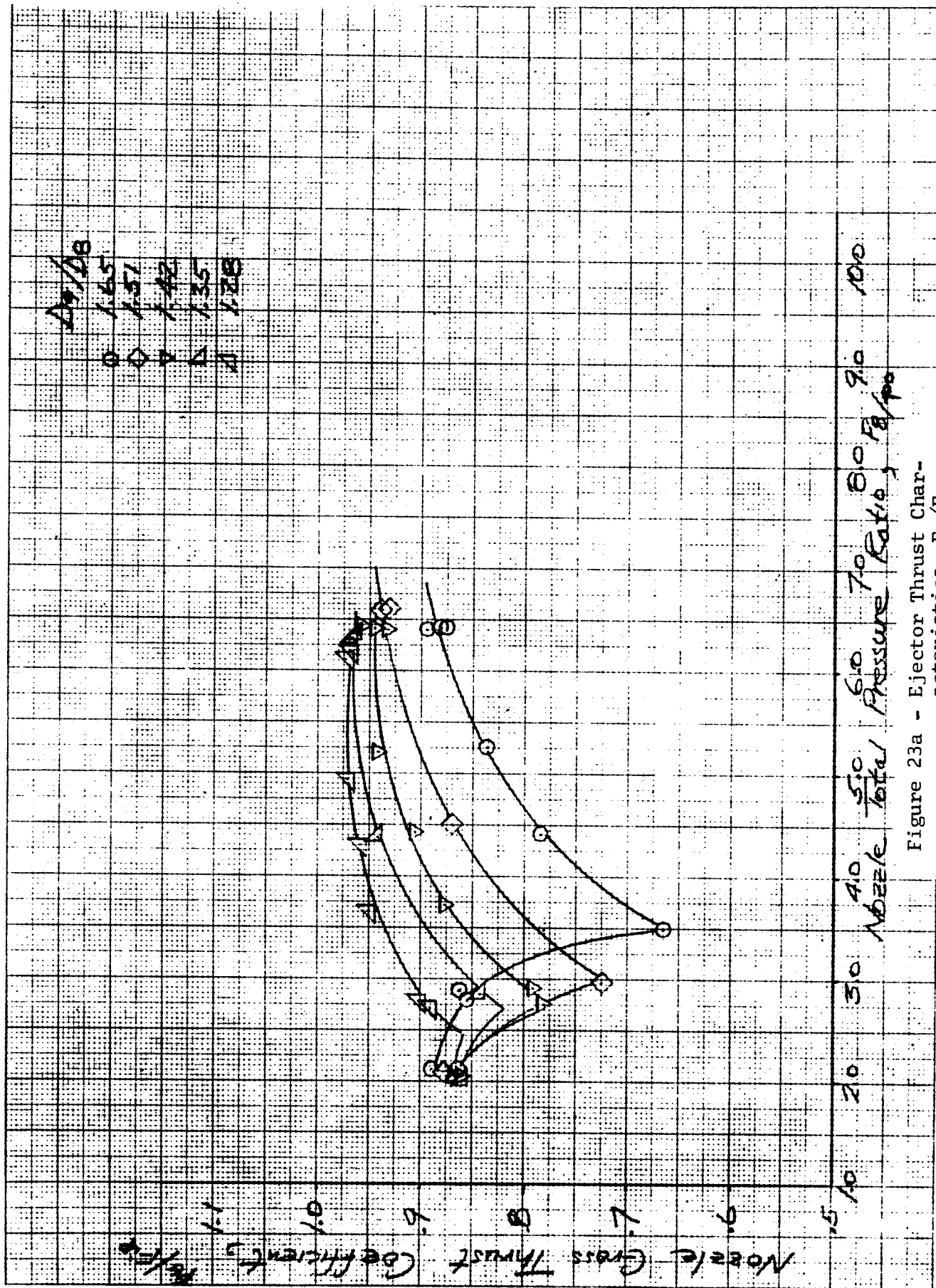
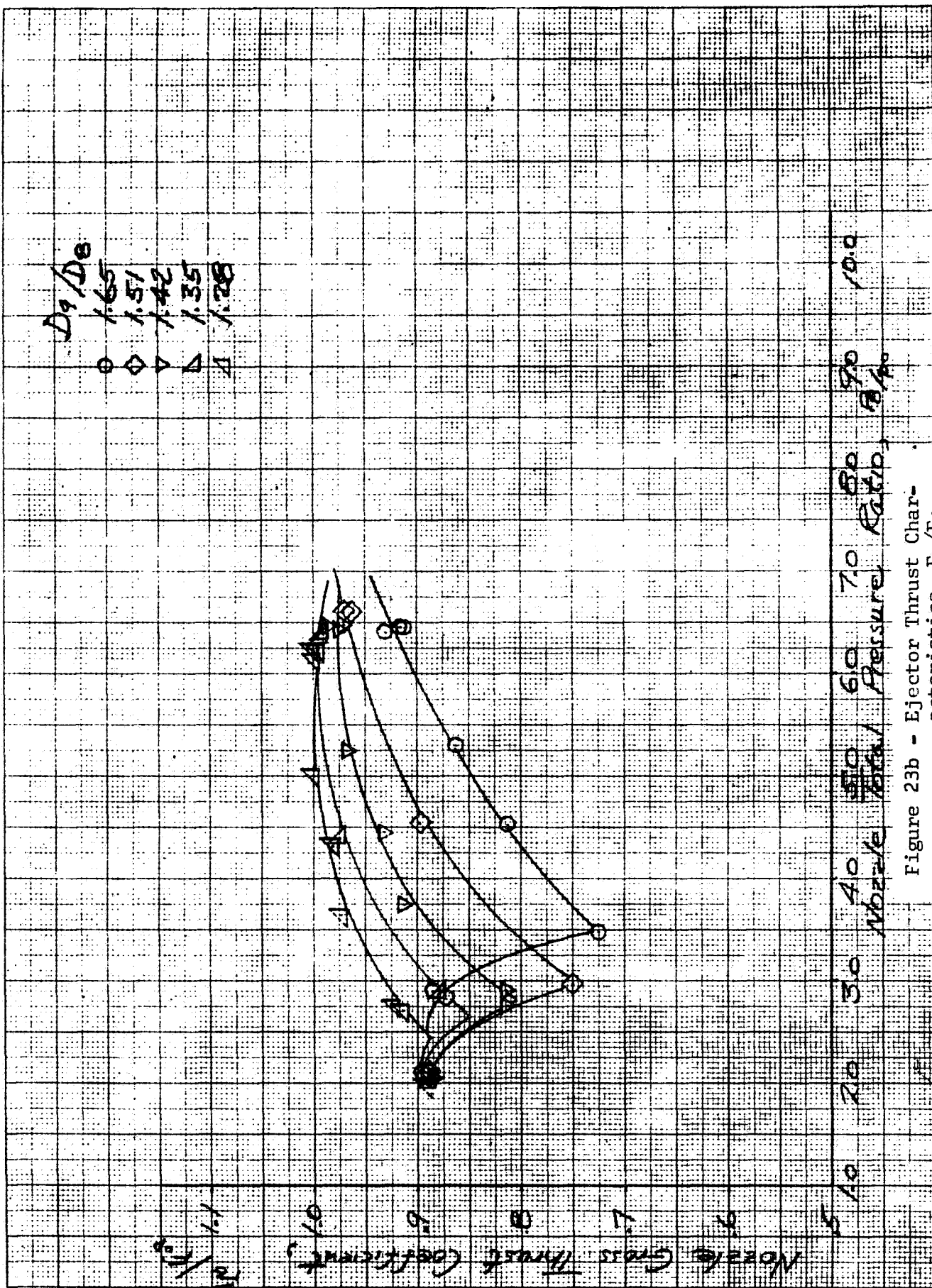


Figure 23a - Ejector Thrust Characteristics, F_G/F_{ip} , Ejector 4 $\omega/\sqrt{\gamma} = .02$



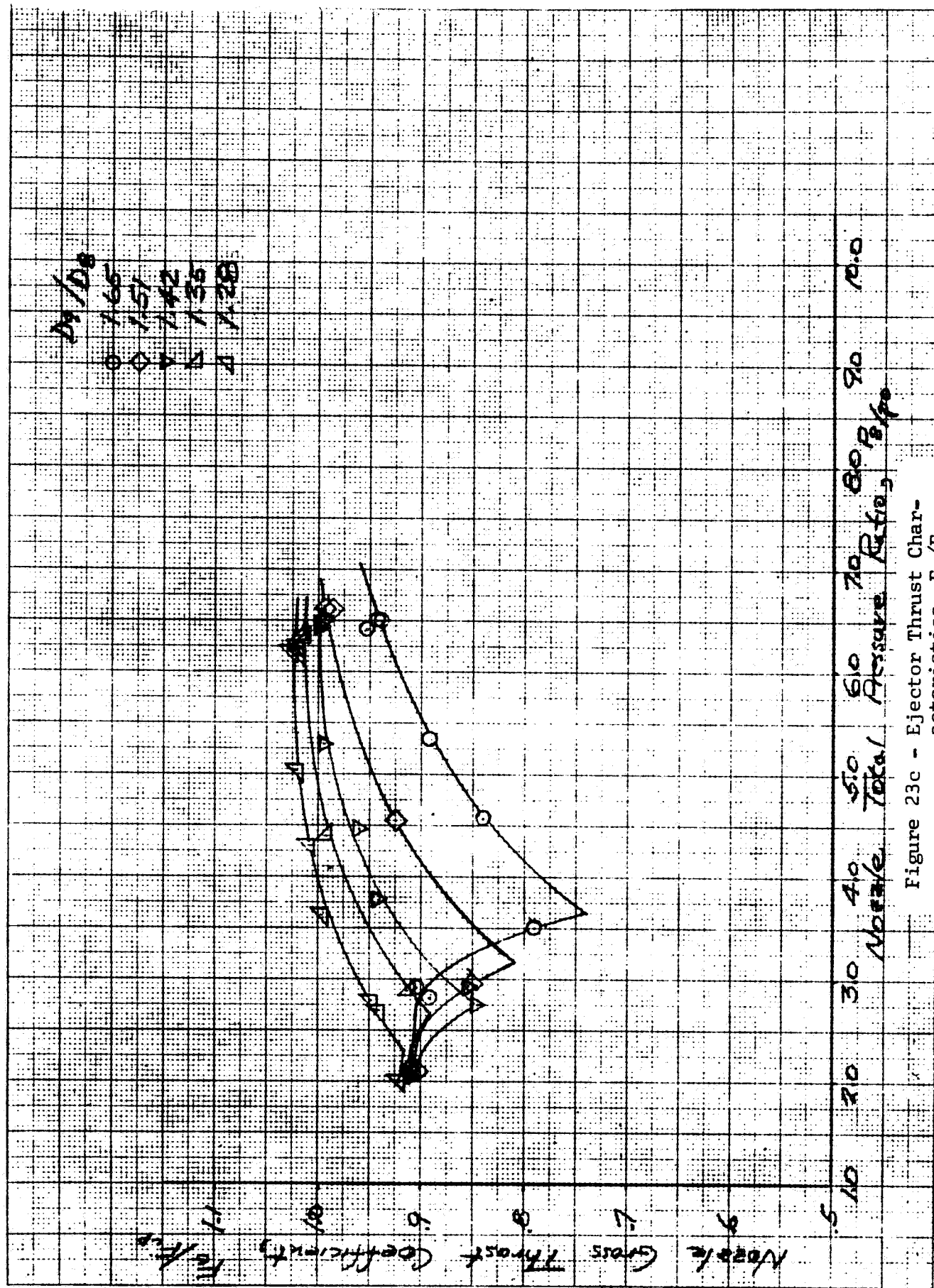


Figure 23c - Ejector Thrust Characteristics, F_g/F_{ip} , Ejector 4 $\omega/\sqrt{P} = .06$

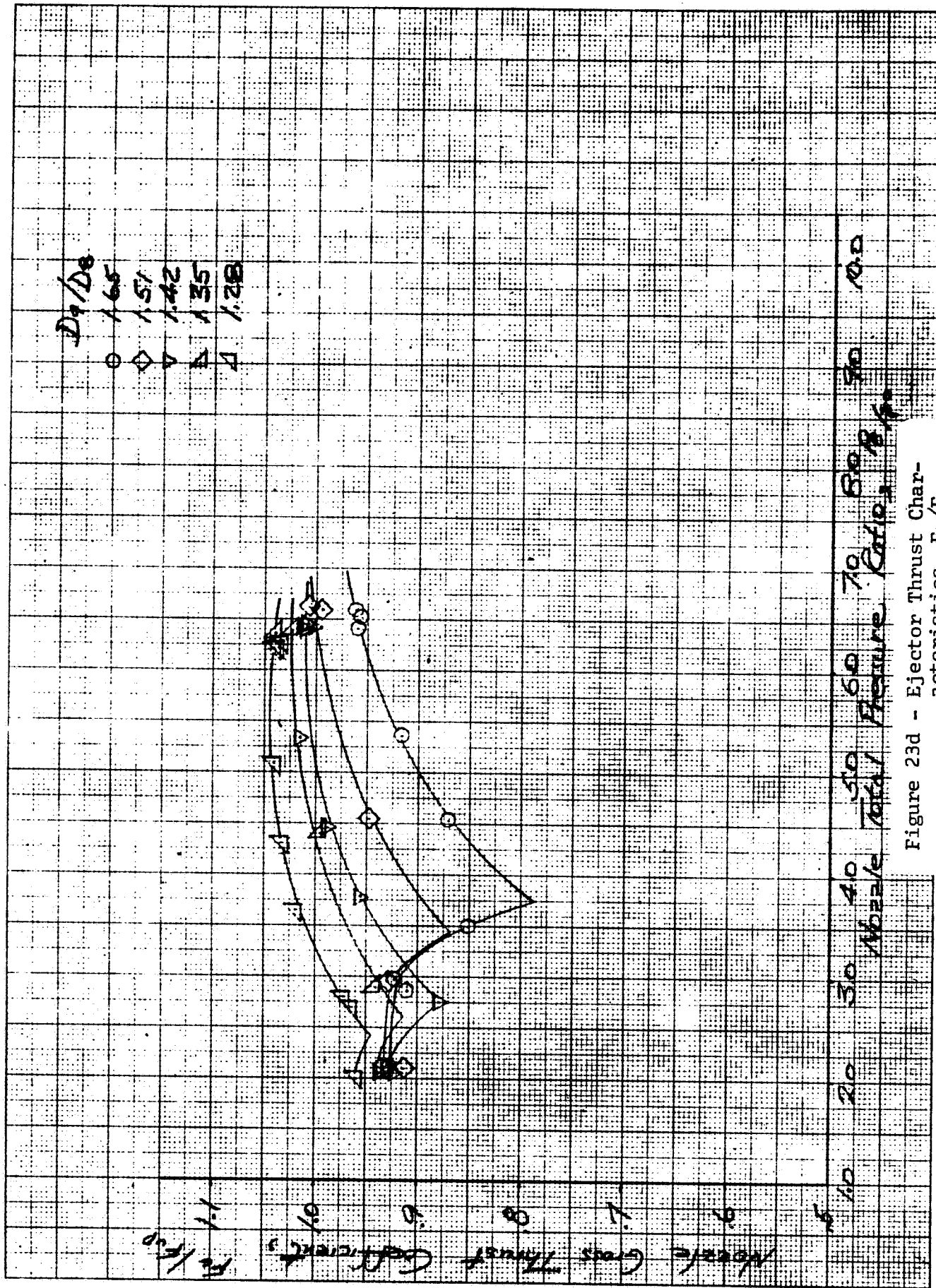


Figure 23d - Ejector Thrust Characteristics, F_g/F_p , Ejector 4 $\omega/\bar{P} = .08$

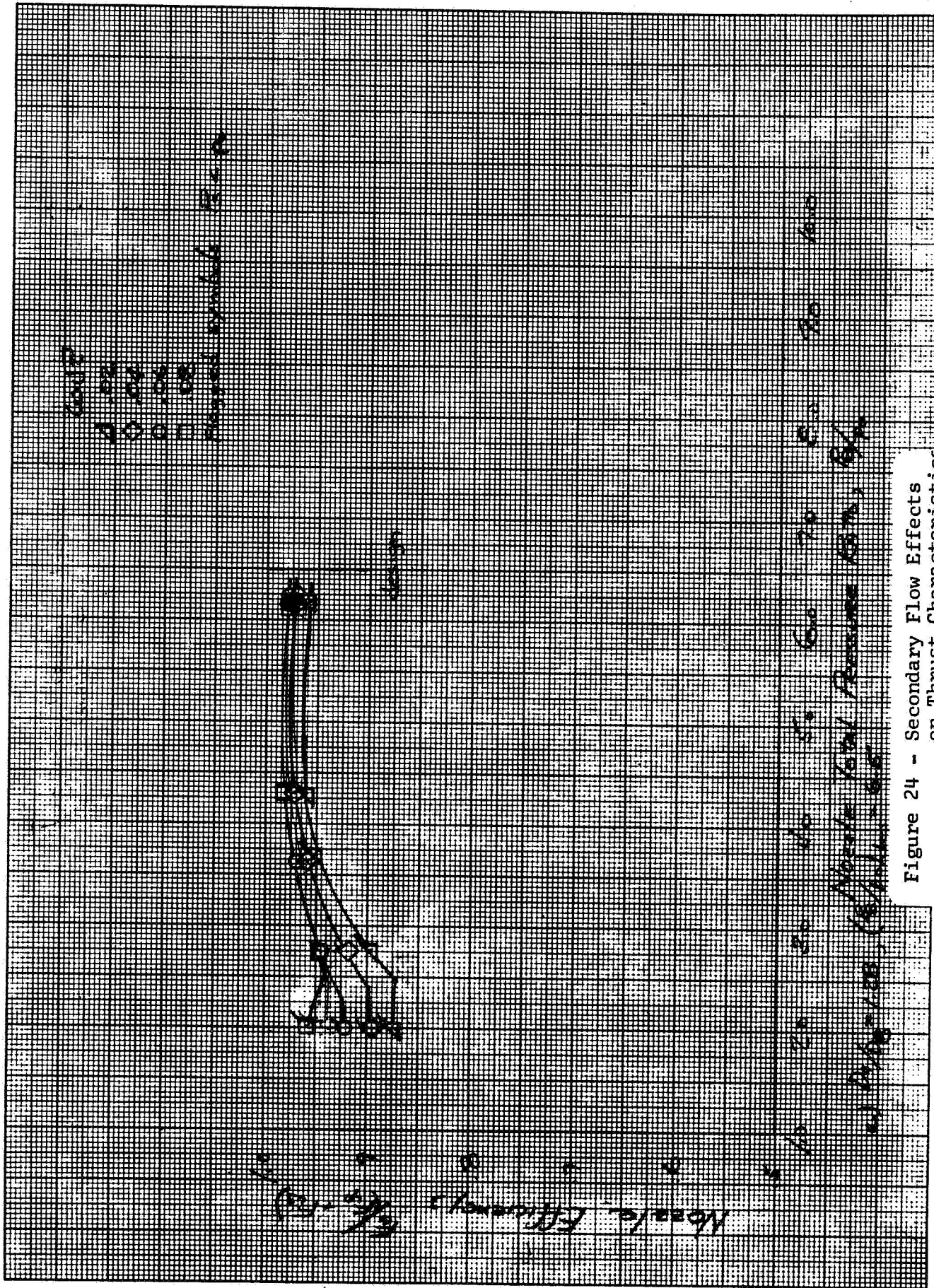


Figure 24 - Secondary Flow Effects
on Thrust Characteristics
of Ejector 4

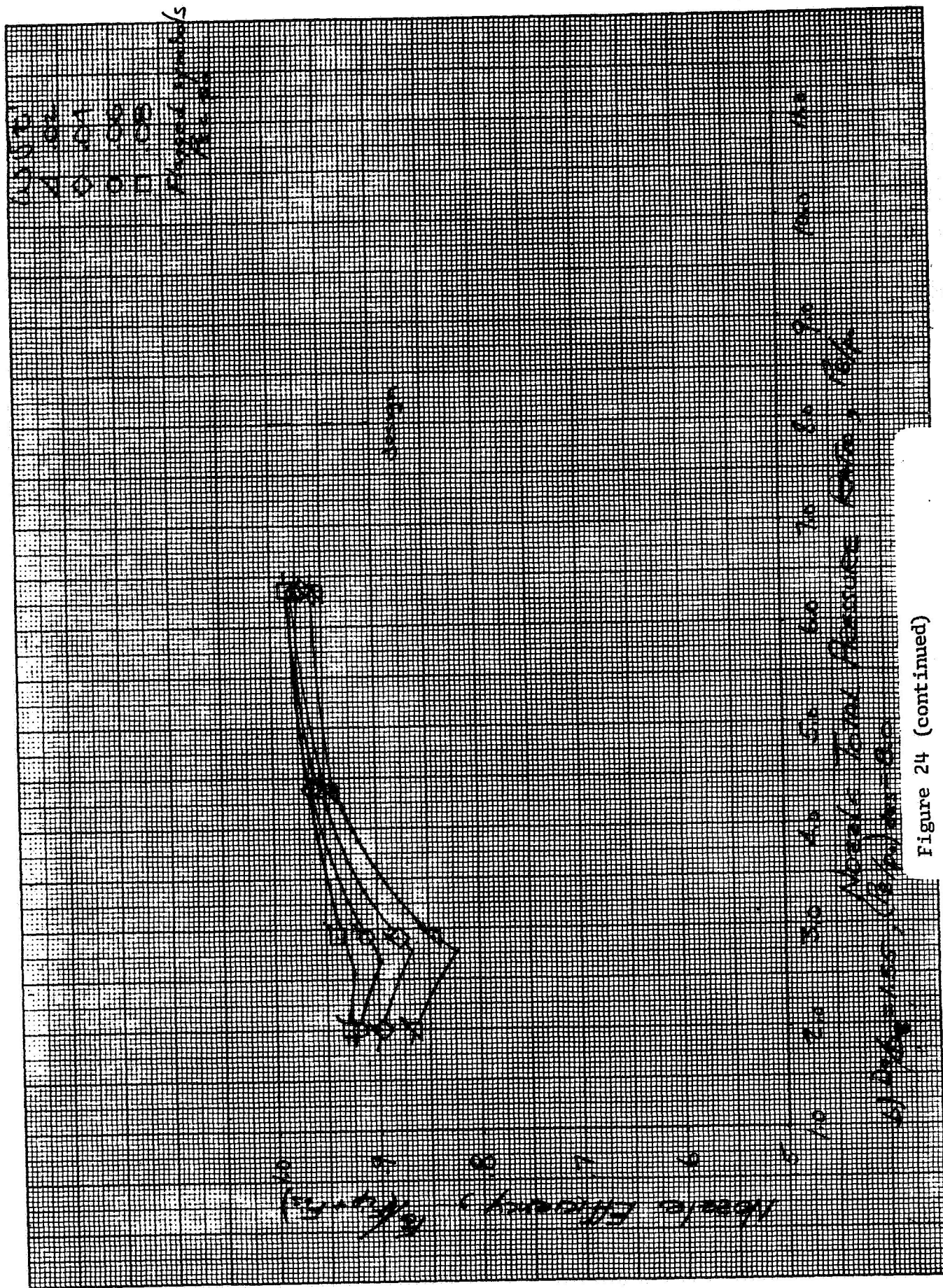
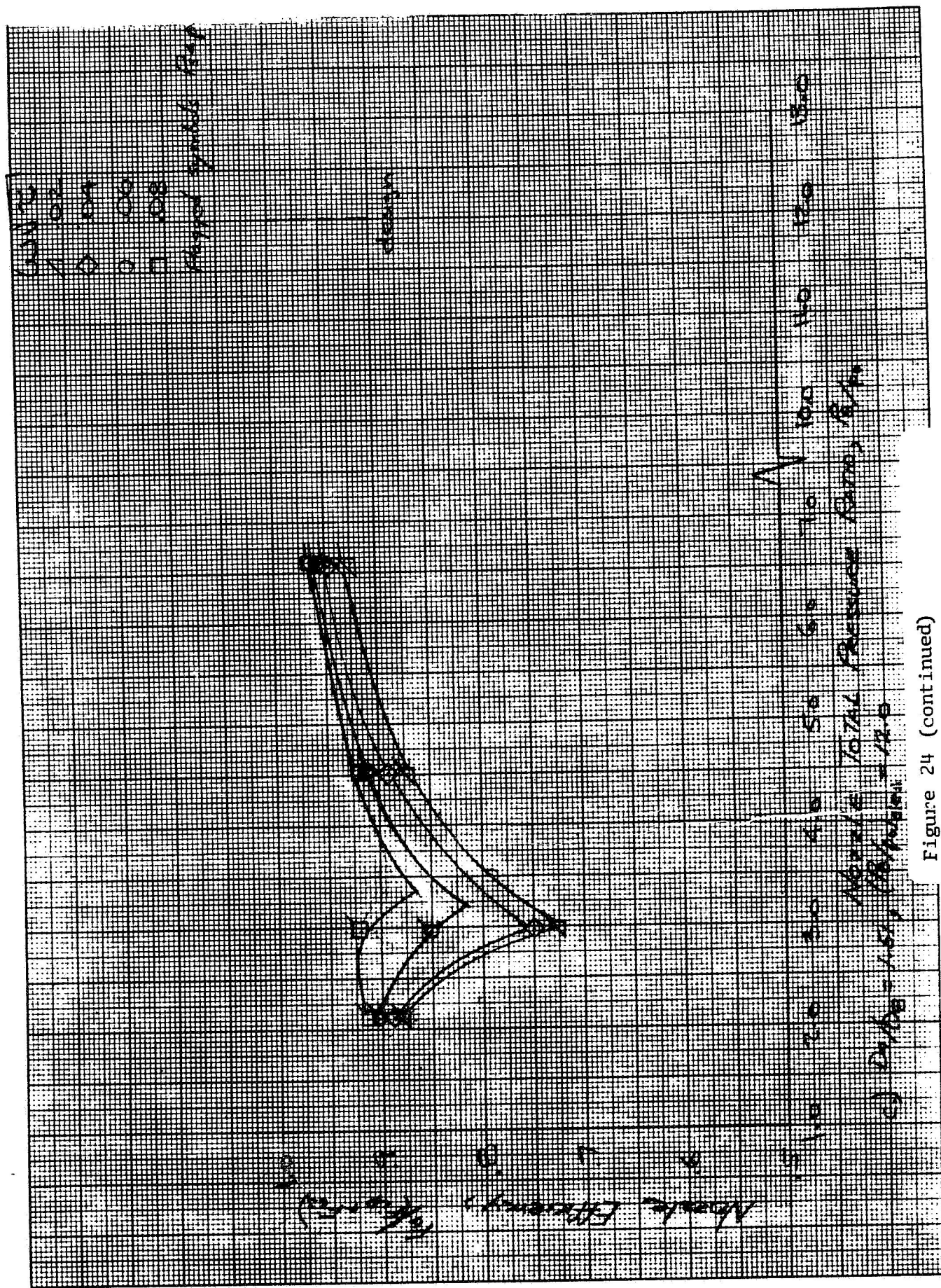
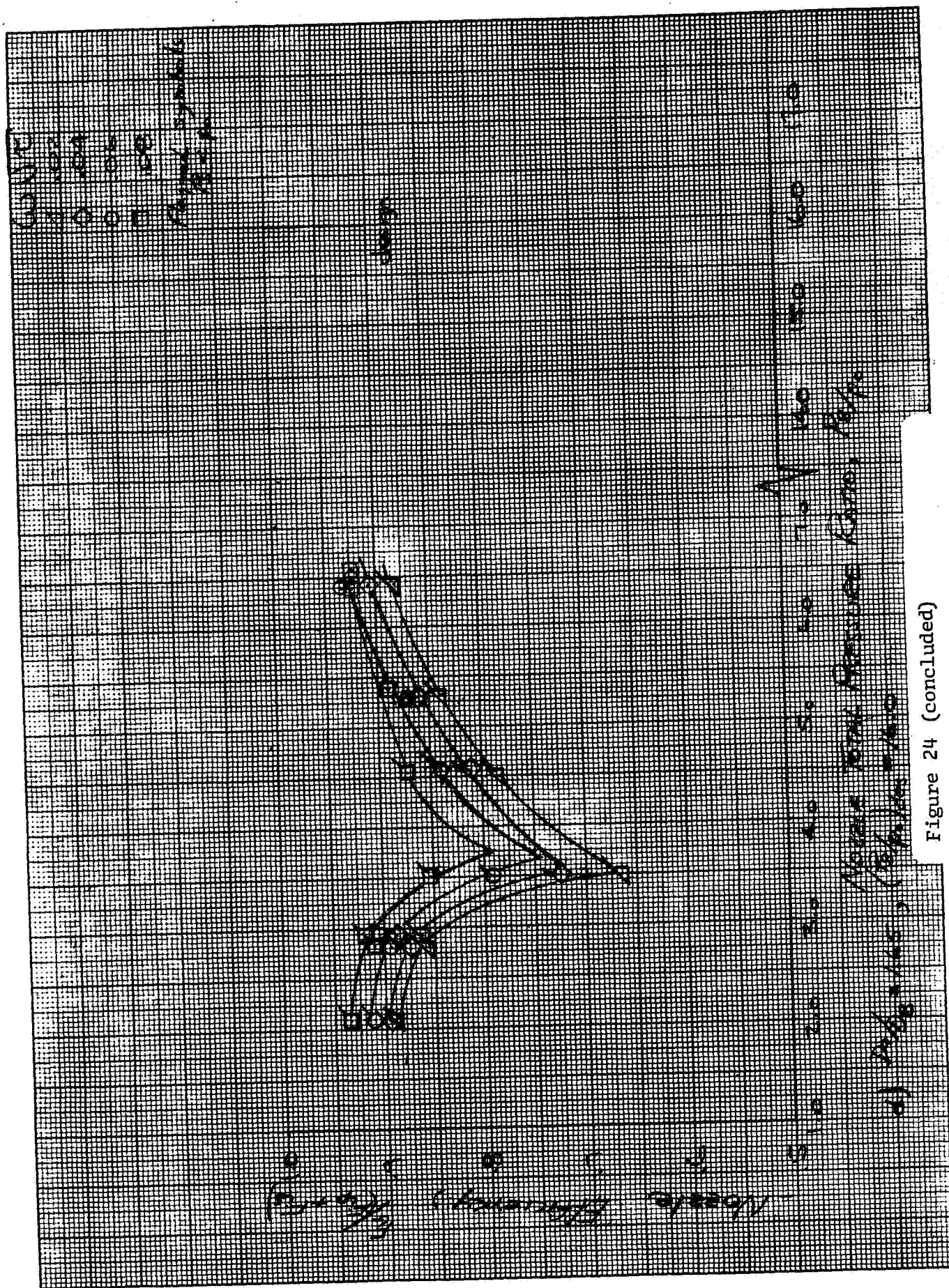


Figure 24 (continued)





Ejector
 Long
 Short
 Pressure Ratio
 1.0
 1.2
 1.4
 1.6
 1.8
 2.0
 2.2
 2.4
 2.6
 2.8
 3.0
 3.2
 3.4
 3.6
 3.8
 4.0
 4.2
 4.4
 4.6
 4.8
 5.0
 5.2
 5.4
 5.6
 5.8
 6.0
 6.2
 6.4
 6.6
 6.8
 7.0
 7.2
 7.4
 7.6
 7.8
 8.0
 8.2
 8.4
 8.6
 8.8
 9.0
 9.2
 9.4
 9.6
 9.8
 10.0
 10.2
 10.4
 10.6
 10.8
 11.0
 11.2
 11.4
 11.6
 11.8
 12.0
 12.2
 12.4
 12.6
 12.8
 13.0
 13.2
 13.4
 13.6
 13.8
 14.0
 14.2
 14.4
 14.6
 14.8
 15.0
 15.2
 15.4
 15.6
 15.8
 16.0
 16.2
 16.4
 16.6
 16.8
 17.0
 17.2
 17.4
 17.6
 17.8
 18.0
 18.2
 18.4
 18.6
 18.8
 19.0
 19.2
 19.4
 19.6
 19.8
 20.0
 20.2
 20.4
 20.6
 20.8
 21.0
 21.2
 21.4
 21.6
 21.8
 22.0
 22.2
 22.4
 22.6
 22.8
 23.0
 23.2
 23.4
 23.6
 23.8
 24.0
 24.2
 24.4
 24.6
 24.8
 25.0
 25.2
 25.4
 25.6
 25.8
 26.0
 26.2
 26.4
 26.6
 26.8
 27.0
 27.2
 27.4
 27.6
 27.8
 28.0
 28.2
 28.4
 28.6
 28.8
 29.0
 29.2
 29.4
 29.6
 29.8
 30.0
 30.2
 30.4
 30.6
 30.8
 31.0
 31.2
 31.4
 31.6
 31.8
 32.0
 32.2
 32.4
 32.6
 32.8
 33.0
 33.2
 33.4
 33.6
 33.8
 34.0
 34.2
 34.4
 34.6
 34.8
 35.0
 35.2
 35.4
 35.6
 35.8
 36.0
 36.2
 36.4
 36.6
 36.8
 37.0
 37.2
 37.4
 37.6
 37.8
 38.0
 38.2
 38.4
 38.6
 38.8
 39.0
 39.2
 39.4
 39.6
 39.8
 40.0
 40.2
 40.4
 40.6
 40.8
 41.0
 41.2
 41.4
 41.6
 41.8
 42.0
 42.2
 42.4
 42.6
 42.8
 43.0
 43.2
 43.4
 43.6
 43.8
 44.0
 44.2
 44.4
 44.6
 44.8
 45.0
 45.2
 45.4
 45.6
 45.8
 46.0
 46.2
 46.4
 46.6
 46.8
 47.0
 47.2
 47.4
 47.6
 47.8
 48.0
 48.2
 48.4
 48.6
 48.8
 49.0
 49.2
 49.4
 49.6
 49.8
 50.0
 50.2
 50.4
 50.6
 50.8
 51.0
 51.2
 51.4
 51.6
 51.8
 52.0
 52.2
 52.4
 52.6
 52.8
 53.0
 53.2
 53.4
 53.6
 53.8
 54.0
 54.2
 54.4
 54.6
 54.8
 55.0
 55.2
 55.4
 55.6
 55.8
 56.0
 56.2
 56.4
 56.6
 56.8
 57.0
 57.2
 57.4
 57.6
 57.8
 58.0
 58.2
 58.4
 58.6
 58.8
 59.0
 59.2
 59.4
 59.6
 59.8
 60.0
 60.2
 60.4
 60.6
 60.8
 61.0
 61.2
 61.4
 61.6
 61.8
 62.0
 62.2
 62.4
 62.6
 62.8
 63.0
 63.2
 63.4
 63.6
 63.8
 64.0
 64.2
 64.4
 64.6
 64.8
 65.0
 65.2
 65.4
 65.6
 65.8
 66.0
 66.2
 66.4
 66.6
 66.8
 67.0
 67.2
 67.4
 67.6
 67.8
 68.0
 68.2
 68.4
 68.6
 68.8
 69.0
 69.2
 69.4
 69.6
 69.8
 70.0
 70.2
 70.4
 70.6
 70.8
 71.0
 71.2
 71.4
 71.6
 71.8
 72.0
 72.2
 72.4
 72.6
 72.8
 73.0
 73.2
 73.4
 73.6
 73.8
 74.0
 74.2
 74.4
 74.6
 74.8
 75.0
 75.2
 75.4
 75.6
 75.8
 76.0
 76.2
 76.4
 76.6
 76.8
 77.0
 77.2
 77.4
 77.6
 77.8
 78.0
 78.2
 78.4
 78.6
 78.8
 79.0
 79.2
 79.4
 79.6
 79.8
 80.0
 80.2
 80.4
 80.6
 80.8
 81.0
 81.2
 81.4
 81.6
 81.8
 82.0
 82.2
 82.4
 82.6
 82.8
 83.0
 83.2
 83.4
 83.6
 83.8
 84.0
 84.2
 84.4
 84.6
 84.8
 85.0
 85.2
 85.4
 85.6
 85.8
 86.0
 86.2
 86.4
 86.6
 86.8
 87.0
 87.2
 87.4
 87.6
 87.8
 88.0
 88.2
 88.4
 88.6
 88.8
 89.0
 89.2
 89.4
 89.6
 89.8
 90.0
 90.2
 90.4
 90.6
 90.8
 91.0
 91.2
 91.4
 91.6
 91.8
 92.0
 92.2
 92.4
 92.6
 92.8
 93.0
 93.2
 93.4
 93.6
 93.8
 94.0
 94.2
 94.4
 94.6
 94.8
 95.0
 95.2
 95.4
 95.6
 95.8
 96.0
 96.2
 96.4
 96.6
 96.8
 97.0
 97.2
 97.4
 97.6
 97.8
 98.0
 98.2
 98.4
 98.6
 98.8
 99.0
 99.2
 99.4
 99.6
 99.8
 100.0
 100.2
 100.4
 100.6
 100.8
 101.0
 101.2
 101.4
 101.6
 101.8
 102.0
 102.2
 102.4
 102.6
 102.8
 103.0
 103.2
 103.4
 103.6
 103.8
 104.0
 104.2
 104.4
 104.6
 104.8
 105.0
 105.2
 105.4
 105.6
 105.8
 106.0
 106.2
 106.4
 106.6
 106.8
 107.0
 107.2
 107.4
 107.6
 107.8
 108.0
 108.2
 108.4
 108.6
 108.8
 109.0
 109.2
 109.4
 109.6
 109.8
 110.0
 110.2
 110.4
 110.6
 110.8
 111.0
 111.2
 111.4
 111.6
 111.8
 112.0
 112.2
 112.4
 112.6
 112.8
 113.0
 113.2
 113.4
 113.6
 113.8
 114.0
 114.2
 114.4
 114.6
 114.8
 115.0
 115.2
 115.4
 115.6
 115.8
 116.0
 116.2
 116.4
 116.6
 116.8
 117.0
 117.2
 117.4
 117.6
 117.8
 118.0
 118.2
 118.4
 118.6
 118.8
 119.0
 119.2
 119.4
 119.6
 119.8
 120.0
 120.2
 120.4
 120.6
 120.8
 121.0
 121.2
 121.4
 121.6
 121.8
 122.0
 122.2
 122.4
 122.6
 122.8
 123.0
 123.2
 123.4
 123.6
 123.8
 124.0
 124.2
 124.4
 124.6
 124.8
 125.0
 125.2
 125.4
 125.6
 125.8
 126.0
 126.2
 126.4
 126.6
 126.8
 127.0
 127.2
 127.4
 127.6
 127.8
 128.0
 128.2
 128.4
 128.6
 128.8
 129.0
 129.2
 129.4
 129.6
 129.8
 130.0
 130.2
 130.4
 130.6
 130.8
 131.0
 131.2
 131.4
 131.6
 131.8
 132.0
 132.2
 132.4
 132.6
 132.8
 133.0
 133.2
 133.4
 133.6
 133.8
 134.0
 134.2
 134.4
 134.6
 134.8
 135.0
 135.2
 135.4
 135.6
 135.8
 136.0
 136.2
 136.4
 136.6
 136.8
 137.0
 137.2
 137.4
 137.6
 137.8
 138.0
 138.2
 138.4
 138.6
 138.8
 139.0
 139.2
 139.4
 139.6
 139.8
 140.0
 140.2
 140.4
 140.6
 140.8
 141.0
 141.2
 141.4
 141.6
 141.8
 142.0
 142.2
 142.4
 142.6
 142.8
 143.0
 143.2
 143.4
 143.6
 143.8
 144.0
 144.2
 144.4
 144.6
 144.8
 145.0
 145.2
 145.4
 145.6
 145.8
 146.0
 146.2
 146.4
 146.6
 146.8
 147.0
 147.2
 147.4
 147.6
 147.8
 148.0
 148.2
 148.4
 148.6
 148.8
 149.0
 149.2
 149.4
 149.6
 149.8
 150.0
 150.2
 150.4
 150.6
 150.8
 151.0
 151.2
 151.4
 151.6
 151.8
 152.0
 152.2
 152.4
 152.6
 152.8
 153.0
 153.2
 153.4
 153.6
 153.8
 154.0
 154.2
 154.4
 154.6
 154.8
 155.0
 155.2
 155.4
 155.6
 155.8
 156.0
 156.2
 156.4
 156.6
 156.8
 157.0
 157.2
 157.4
 157.6
 157.8
 158.0
 158.2
 158.4
 158.6
 158.8
 159.0
 159.2
 159.4
 159.6
 159.8
 160.0
 160.2
 160.4
 160.6
 160.8
 161.0
 161.2
 161.4
 161.6
 161.8
 162.0
 162.2
 162.4
 162.6
 162.8
 163.0
 163.2
 163.4
 163.6
 163.8
 164.0
 164.2
 164.4
 164.6
 164.8
 165.0
 165.2
 165.4
 165.6
 165.8
 166.0
 166.2
 166.4
 166.6
 166.8
 167.0
 167.2
 167.4
 167.6
 167.8
 168.0
 168.2
 168.4
 168.6
 168.8
 169.0
 169.2
 169.4
 169.6
 169.8
 170.0
 170.2
 170.4
 170.6
 170.8
 171.0
 171.2
 171.4
 171.6
 171.8
 172.0
 172.2
 172.4
 172.6
 172.8
 173.0
 173.2
 173.4
 173.6
 173.8
 174.0
 174.2
 174.4
 174.6
 174.8
 175.0
 175.2
 175.4
 175.6
 175.8
 176.0
 176.2
 176.4
 176.6
 176.8
 177.0
 177.2
 177.4
 177.6
 177.8
 178.0
 178.2
 178.4
 178.6
 178.8
 179.0
 179.2
 179.4
 179.6
 179.8
 180.0
 180.2
 180.4
 180.6
 180.8
 181.0
 181.2
 181.4
 181.6
 181.8
 182.0
 182.2
 182.4
 182.6
 182.8
 183.0
 183.2
 183.4
 183.6
 183.8
 184.0
 184.2
 184.4
 184.6
 184.8
 185.0
 185.2
 185.4
 185.6
 185.8
 186.0
 186.2
 186.4
 186.6
 186.8
 187.0
 187.2
 187.4
 187.6
 187.8
 188.0
 188.2
 188.4
 188.6
 188.8
 189.0
 189.2
 189.4
 189.6
 189.8
 190.0
 190.2
 190.4
 190.6
 190.8
 191.0
 191.2
 191.4
 191.6
 191.8
 192.0
 192.2
 192.4
 192.6
 192.8
 193.0
 193.2
 193.4
 193.6
 193.8
 194.0
 194.2
 194.4
 194.6
 194.8
 195.0
 195.2
 195.4
 195.6
 195.8
 196.0
 196.2
 196.4
 196.6
 196.8
 197.0
 197.2
 197.4
 197.6
 197.8
 198.0
 198.2
 198.4
 198.6
 198.8
 199.0
 199.2
 199.4
 199.6
 199.8
 200.0
 200.2
 200.4
 200.6
 200.8
 201.0
 201.2
 201.4
 201.6
 201.8
 202.0
 202.2
 202.4
 202.6
 202.8
 203.0
 203.2
 203.4
 203.6
 203.8
 204.0
 204.2
 204.4
 204.6
 204.8
 205.0
 205.2
 205.4
 205.6
 205.8
 206.0
 206.2
 206.4
 206.6
 206.8
 207.0
 207.2
 207.4
 207.6
 207.8
 208.0
 208.2
 208.4
 208.6
 208.8
 209.0
 209.2
 209.4
 209.6
 209.8
 210.0
 210.2
 210.4
 210.6
 210.8
 211.0
 211.2
 211.4
 211.6
 211.8
 212.0
 212.2
 212.4
 212.6
 212.8
 213.0
 213.2
 213.4
 213.6
 213.8
 214.0
 214.2
 214.4
 214.6
 214.8
 215.0
 215.2
 215.4
 215.6
 215.8
 216.0
 216.2
 216.4
 216.6
 216.8
 217.0
 217.2
 217.4
 217.6
 217.8
 218.0
 218.2
 218.4
 218.6
 218.8
 219.0
 219.2
 219.4
 219.6
 219.8
 220.0
 220.2
 220.4
 220.6
 220.8
 221.0
 221.2
 221.4
 221.6
 221.8
 222.0
 222.2
 222.4
 222.6
 222.8
 223.0
 223.2
 223.4
 223.6
 223.8
 224.0
 224.2
 224.4
 224.6
 224.8
 225.0
 225.2
 225.4
 225.6
 225.8
 226.0
 226.2
 226.4
 226.6
 226.8
 227.0
 227.2
 227.4
 227.6
 227.8
 228.0
 228.2
 228.4
 228.6
 228.8
 229.0
 229.2
 229.4
 229.6
 229.8
 230.0
 230.2
 230.4
 230.6
 230.8
 231.0
 231.2
 231.4
 231.6
 231.8
 232.0
 232.2
 232.4
 232.6
 232.8
 233.0
 233.2
 233.4
 233.6
 233.8
 234.0
 234.2
 234.4
 234.6
 234.8
 235.0
 235.2
 235.4
 235.6
 235.8
 236.0
 236.2
 236.4
 236.6
 236.8
 237.0
 237.2
 237.4
 237.6
 237.8
 238.0
 238.2
 238.4
 238.6
 238.8
 239.0
 239.2
 239.4
 239.6
 239.8
 240.0
 240.2
 240.4
 240.6
 240.8
 241.0
 241.2
 241.4
 241.6
 241.8
 242.0
 242.2
 242.4
 242.6
 242.8
 243.0
 243.2
 243.4
 243.6
 243.8
 244.0
 244.2
 244.4
 244.6
 244.8
 245.0
 245.2
 245.4
 245.6
 245.8
 246.0
 246.2
 246.4
 246.6
 246.8
 247.0
 247.2
 247.4
 247.6
 247.8
 248.0
 248.2
 248.4
 248.6
 248.8
 249.0
 249.2
 249.4
 249.6
 249.8
 250.0
 250.2
 250.4
 250.6
 250.8
 251.0
 251.2
 251.4
 251.6
 251.8
 252.0
 252.2
 252.4
 252.6
 252.8
 253.0
 253.2
 253.4
 253.6
 253.8
 254.0
 254.2
 254.4
 254.6
 254.8
 255.0
 255.2
 255.4
 255.6
 255.8
 256.0
 256.2
 256.4
 256.6
 256.8
 257.0
 257.2
 257.4
 257.6
 257.8
 258.0
 258.2

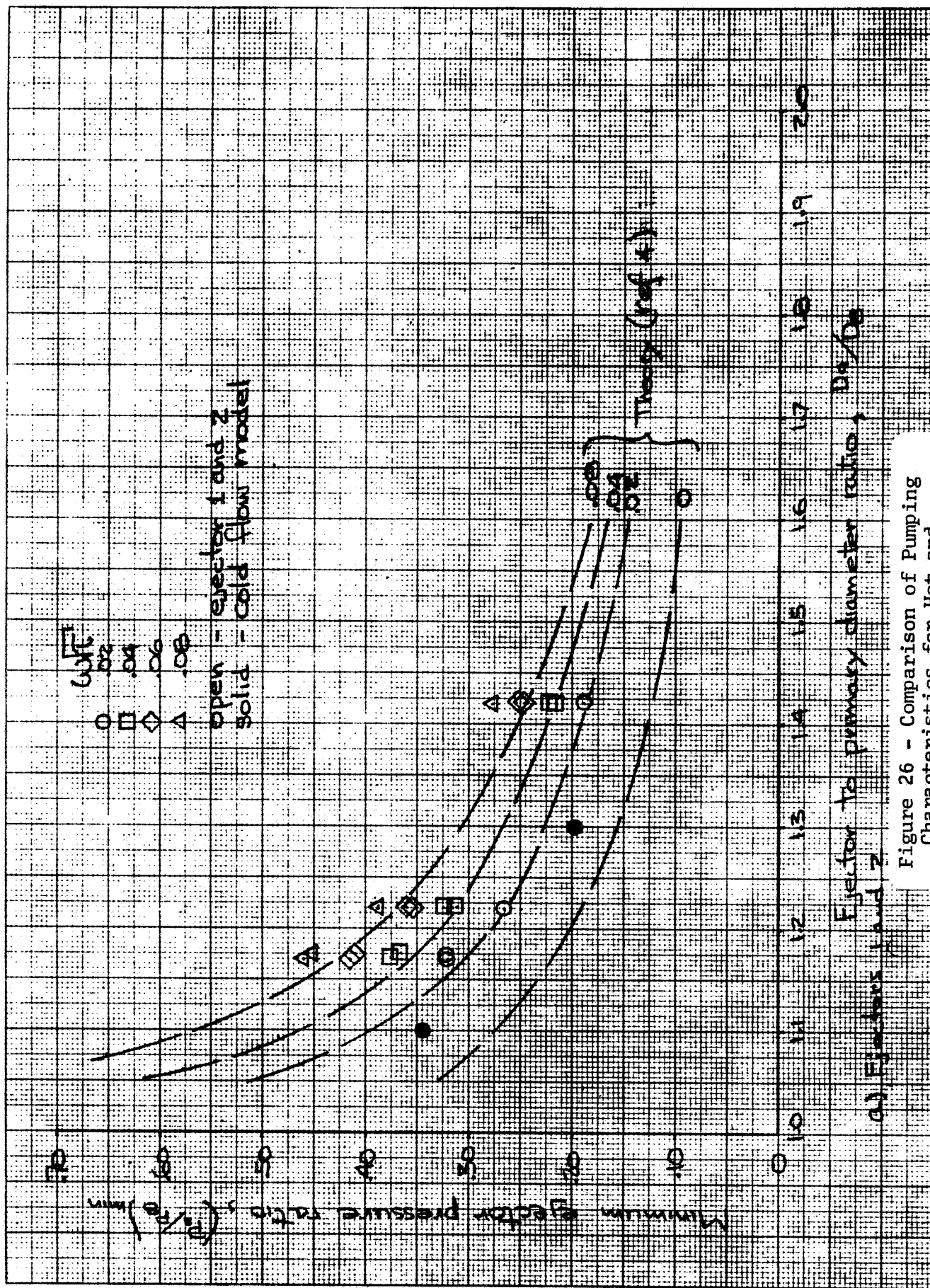


Figure 26 - Comparison of Pumping Characteristics for Hot and Cold Flow Cylindrical Ejectors

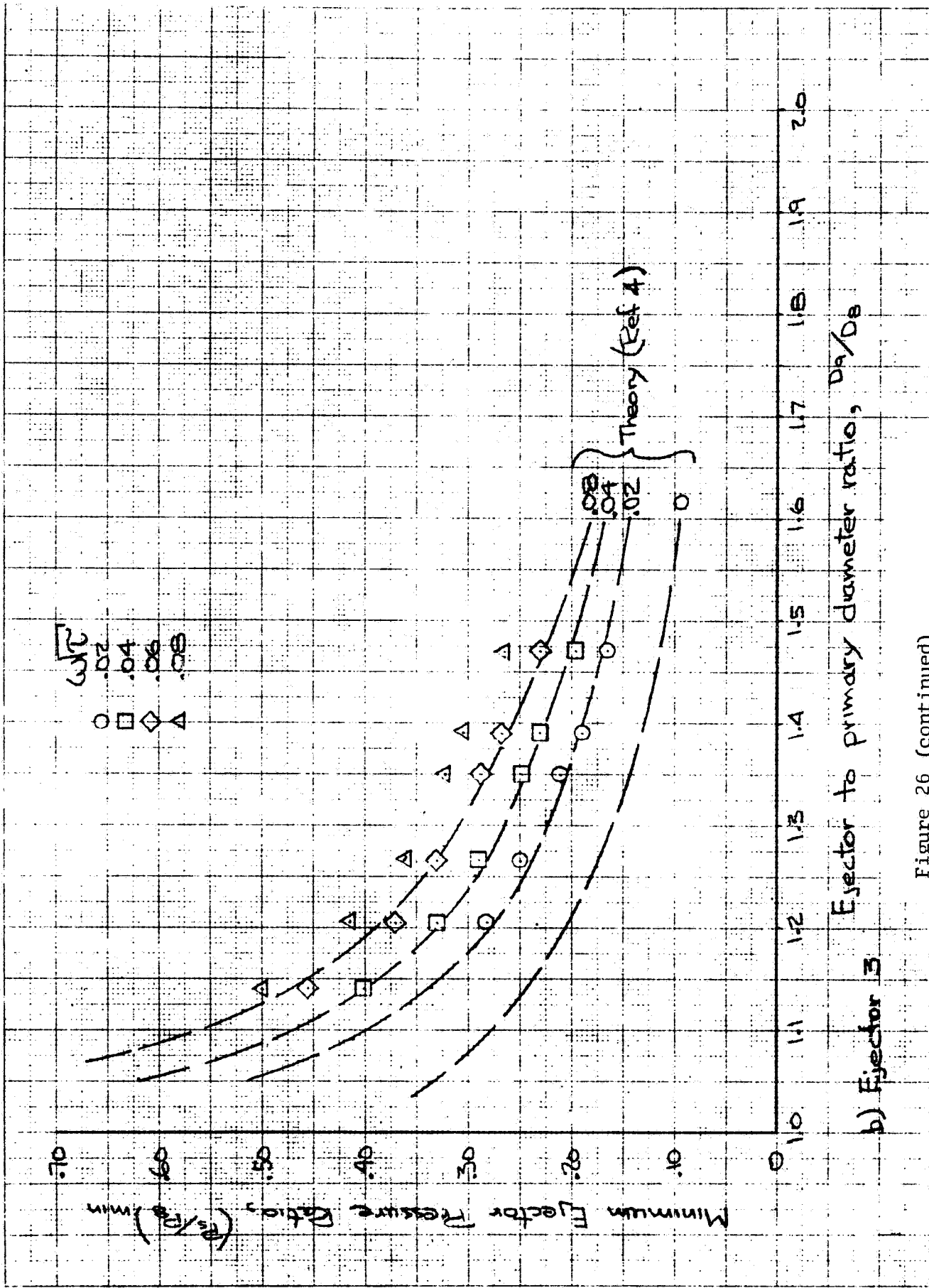


Figure 26 (continued)

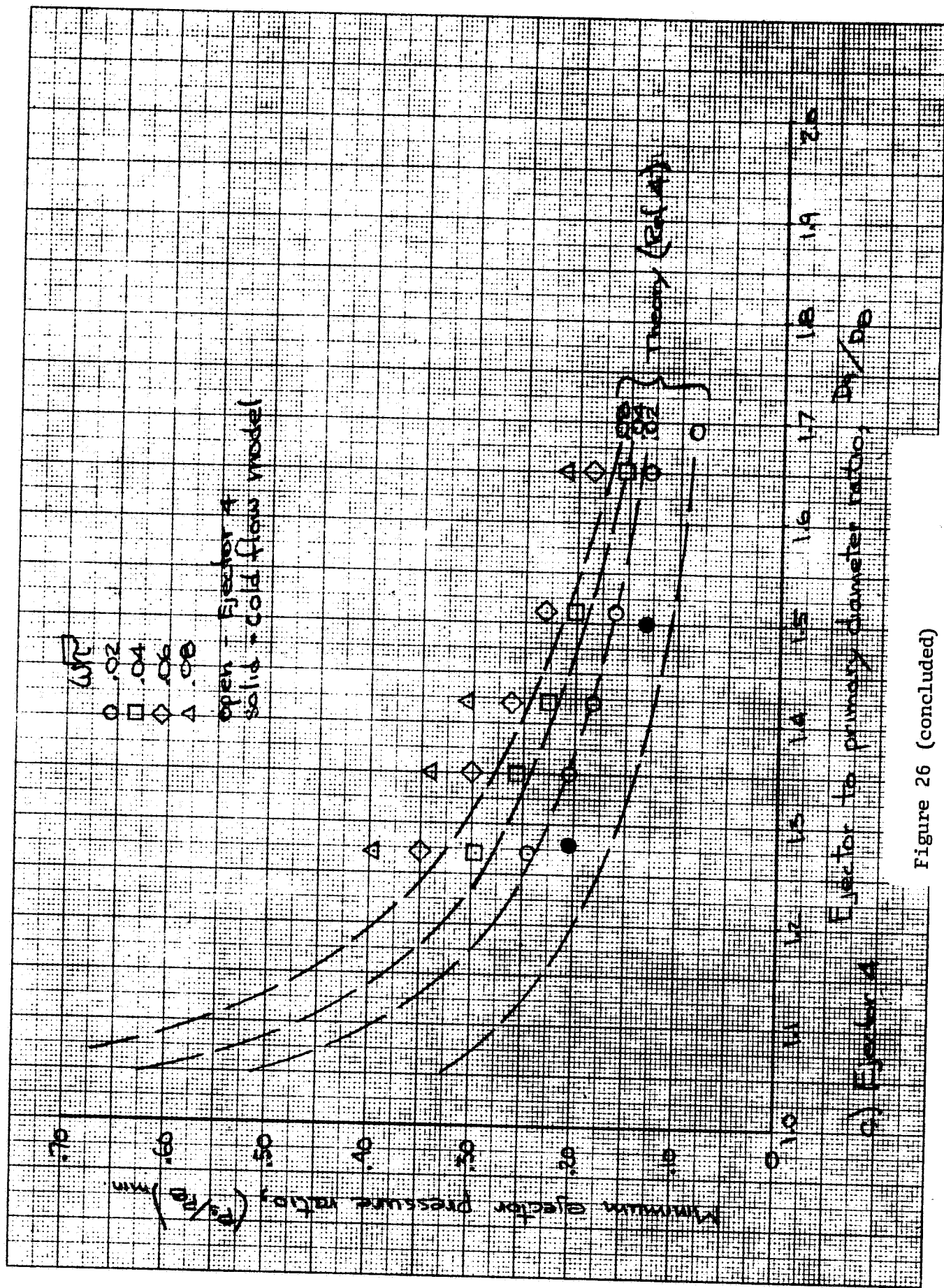
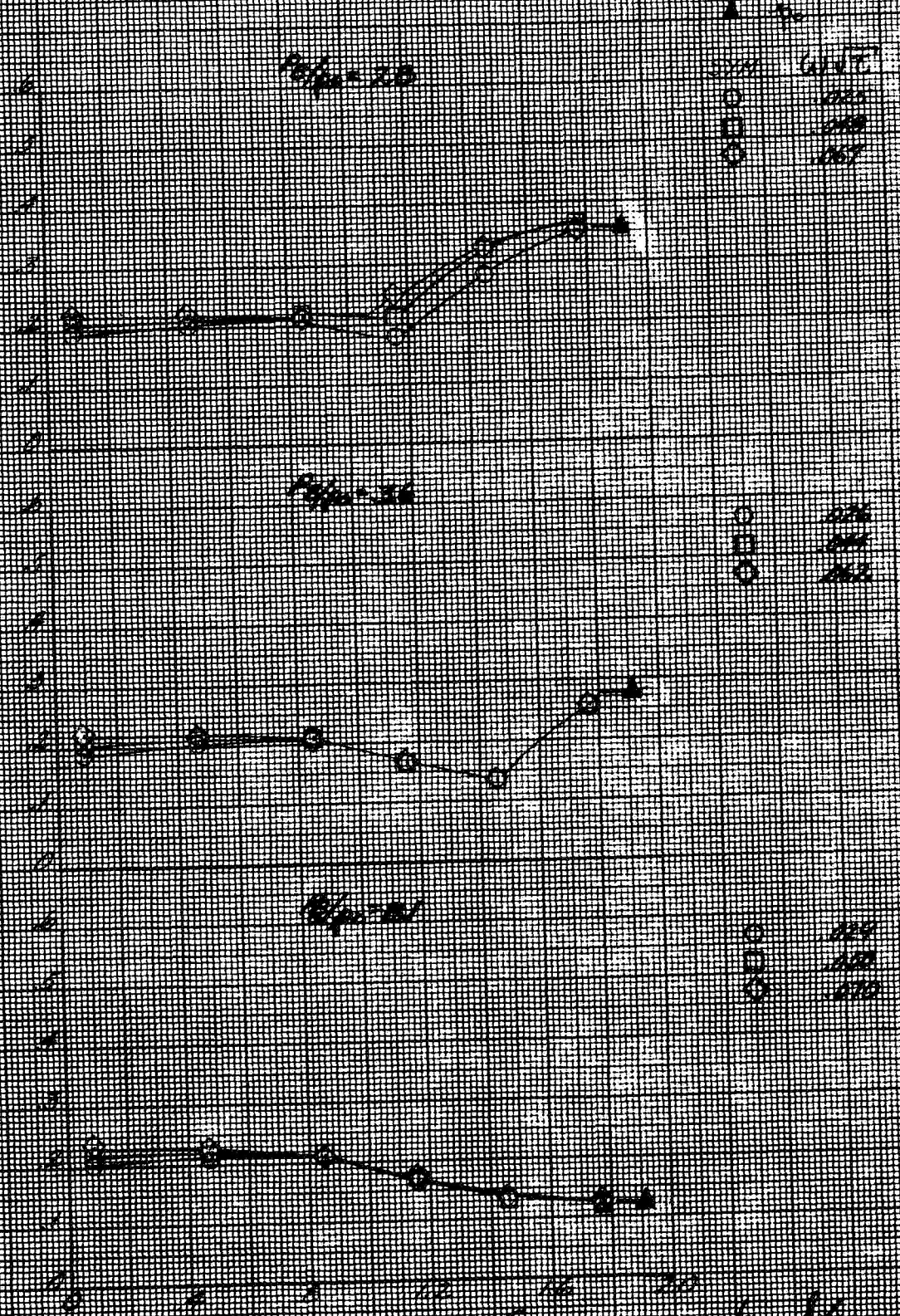


Figure 26 (concluded)

Wall pressure and temperature distribution in ejector

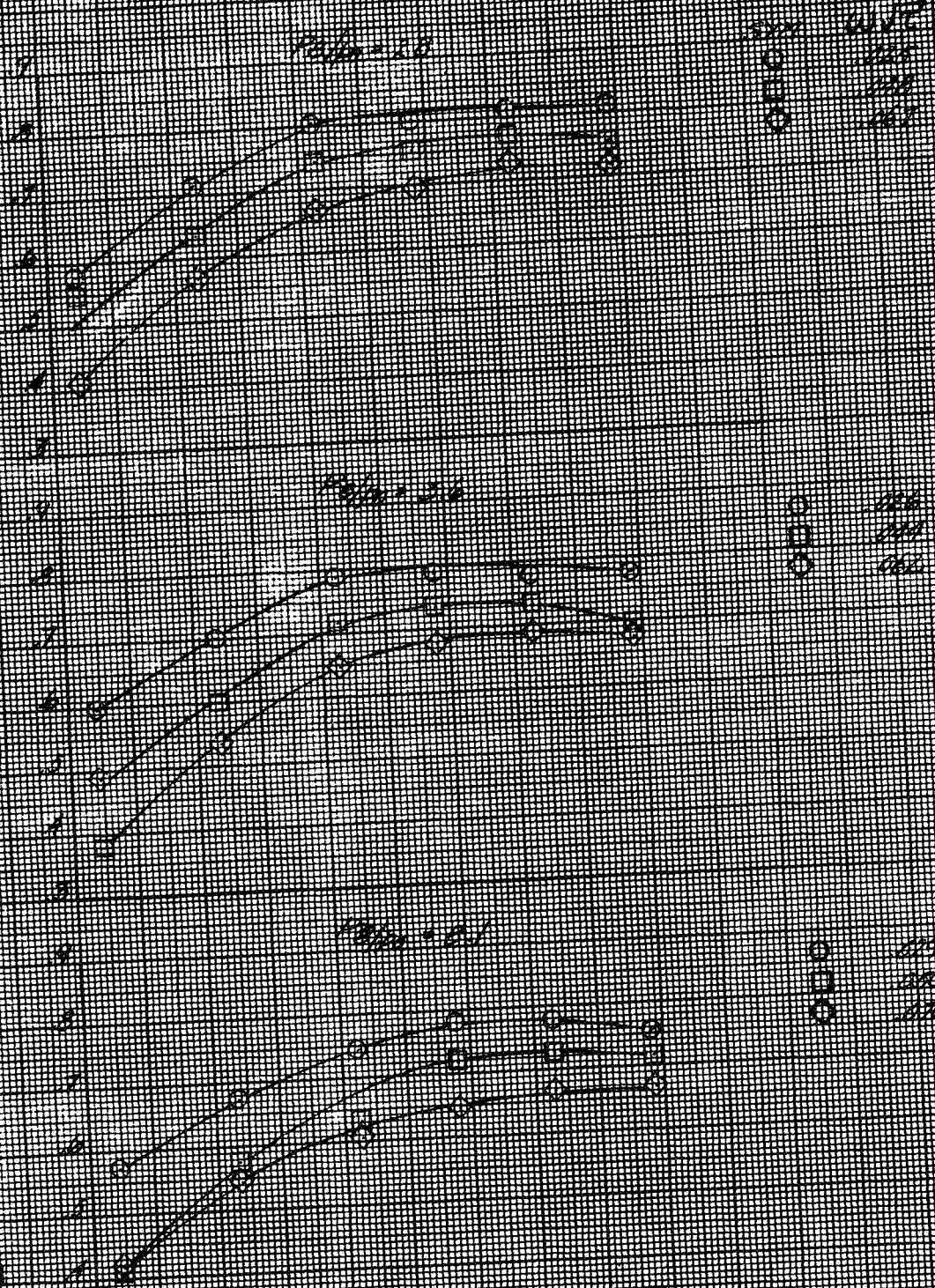


Diameter downstream of primary nozzle, d/d_0
 at 75% speed, $P_0 = 100 \times 10^4$ N/m² (atmosphere - 7.5

Figure 27 - Wall Pressure and Temperature Distribution of Ejector 3

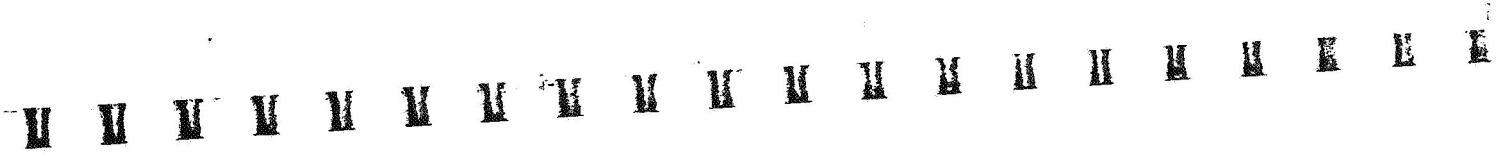


Extrinsic loss due to power and temperature rise.



Extrinsic loss due to power and temperature rise, W_{ex}
 b) 95% speed, $T_a = 750^\circ K$, $(P/\eta)_{max} = 9.5$

Figure 27 (continued)



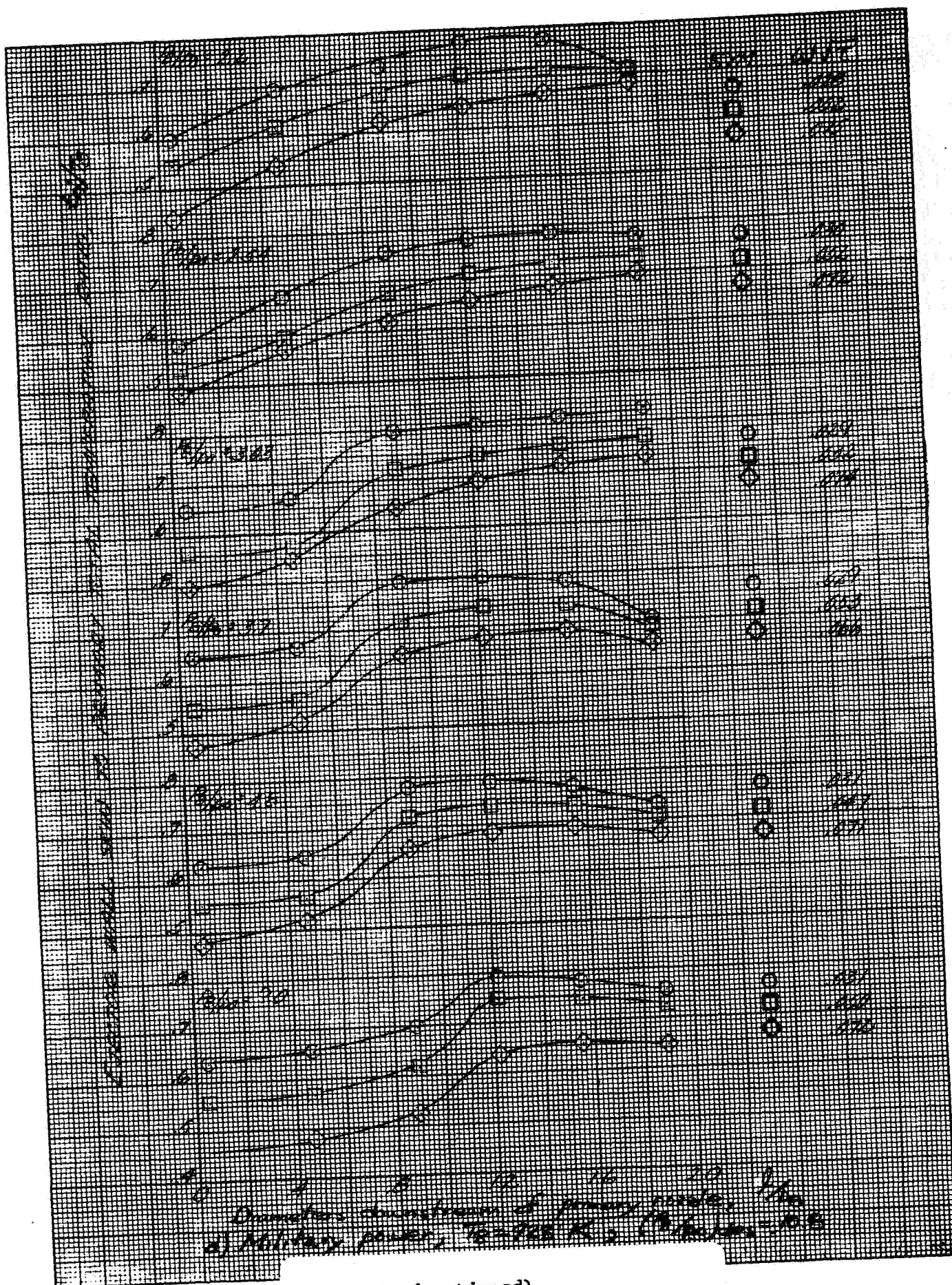


Figure 27 (continued)

Curves are drawn to nearest and nearest mm.

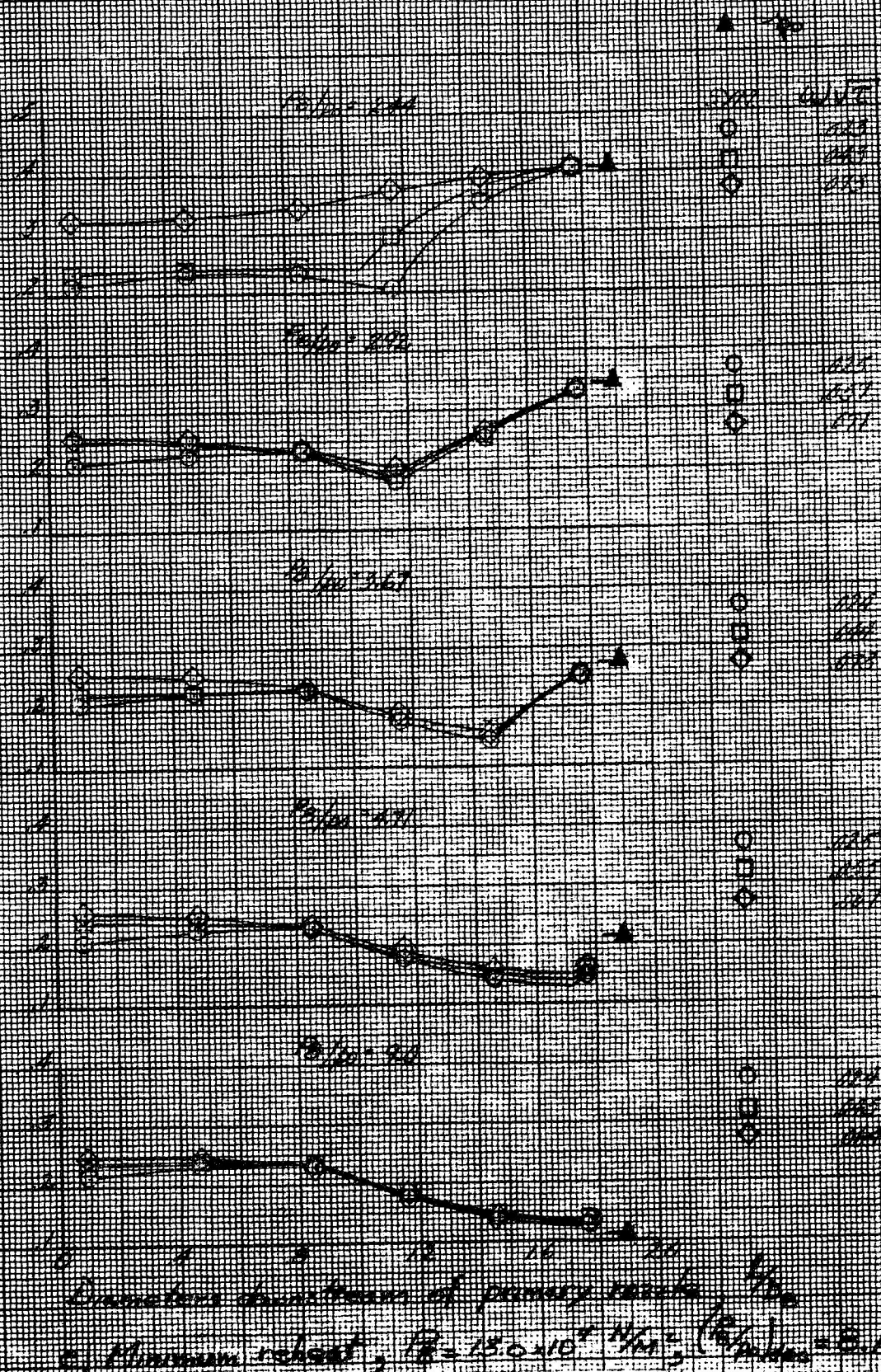
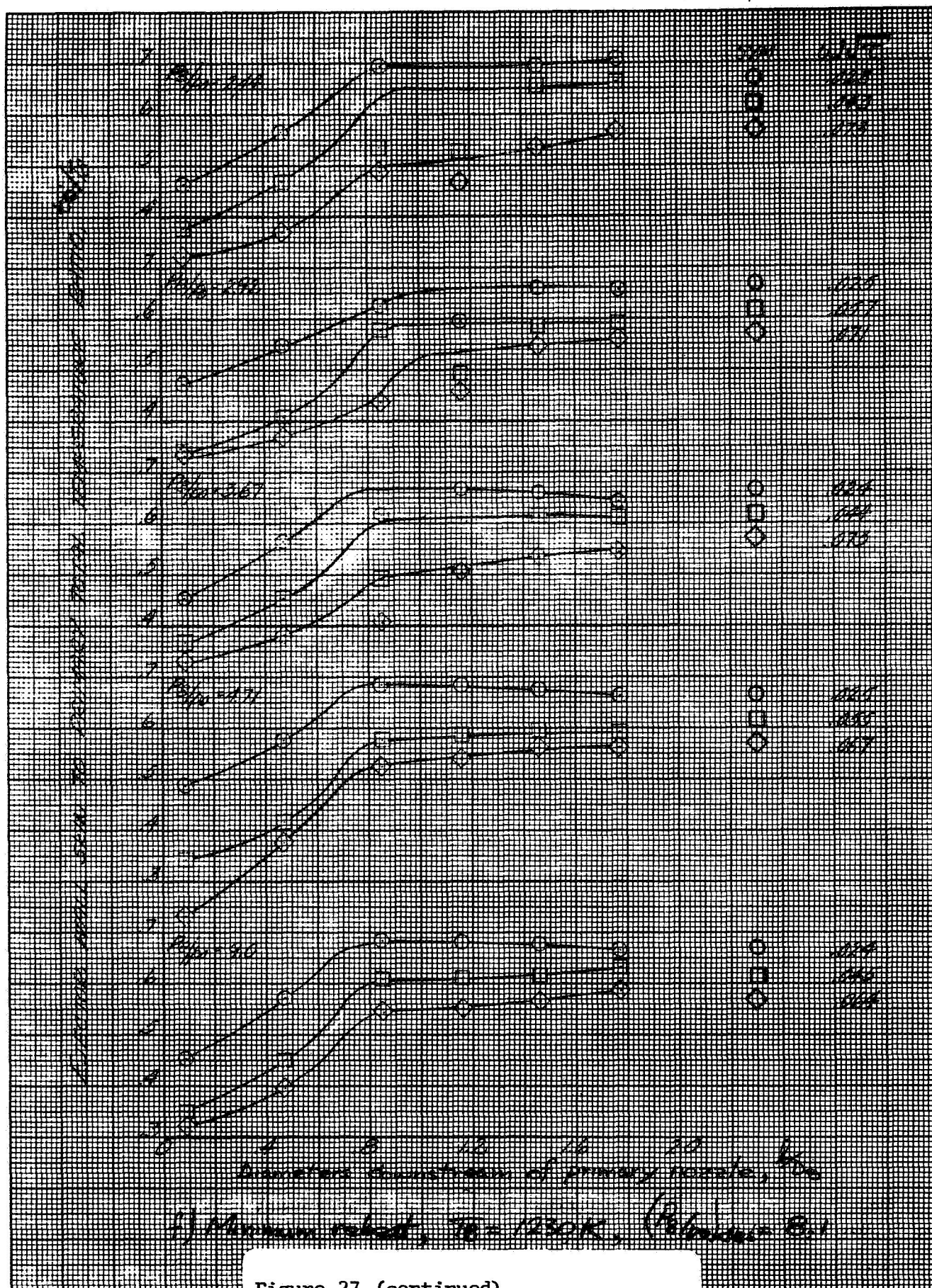


Figure 27 (continued)



Curves were drawn to minimum and maximum values of curves from average

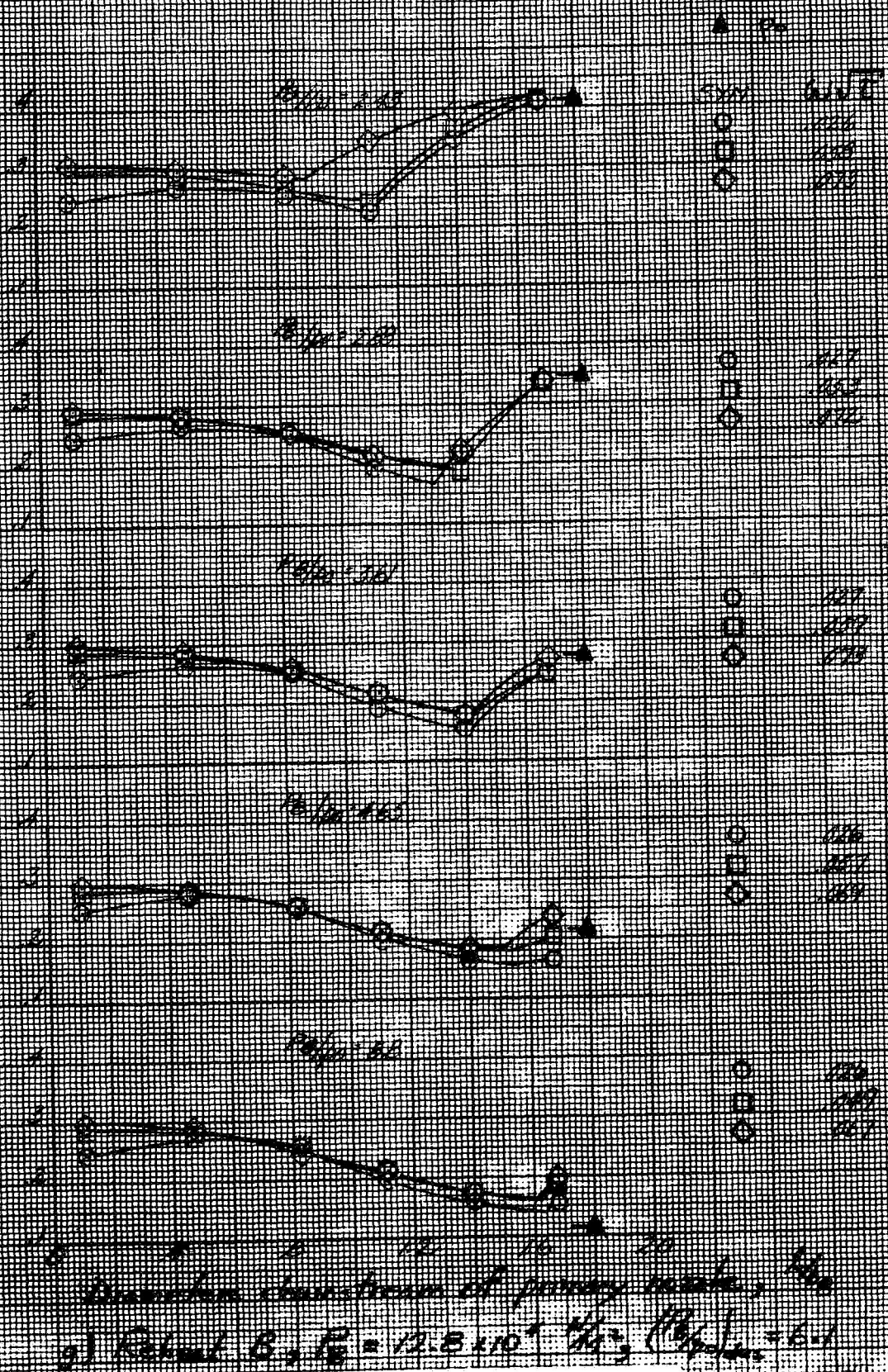


Figure 27 (continued)

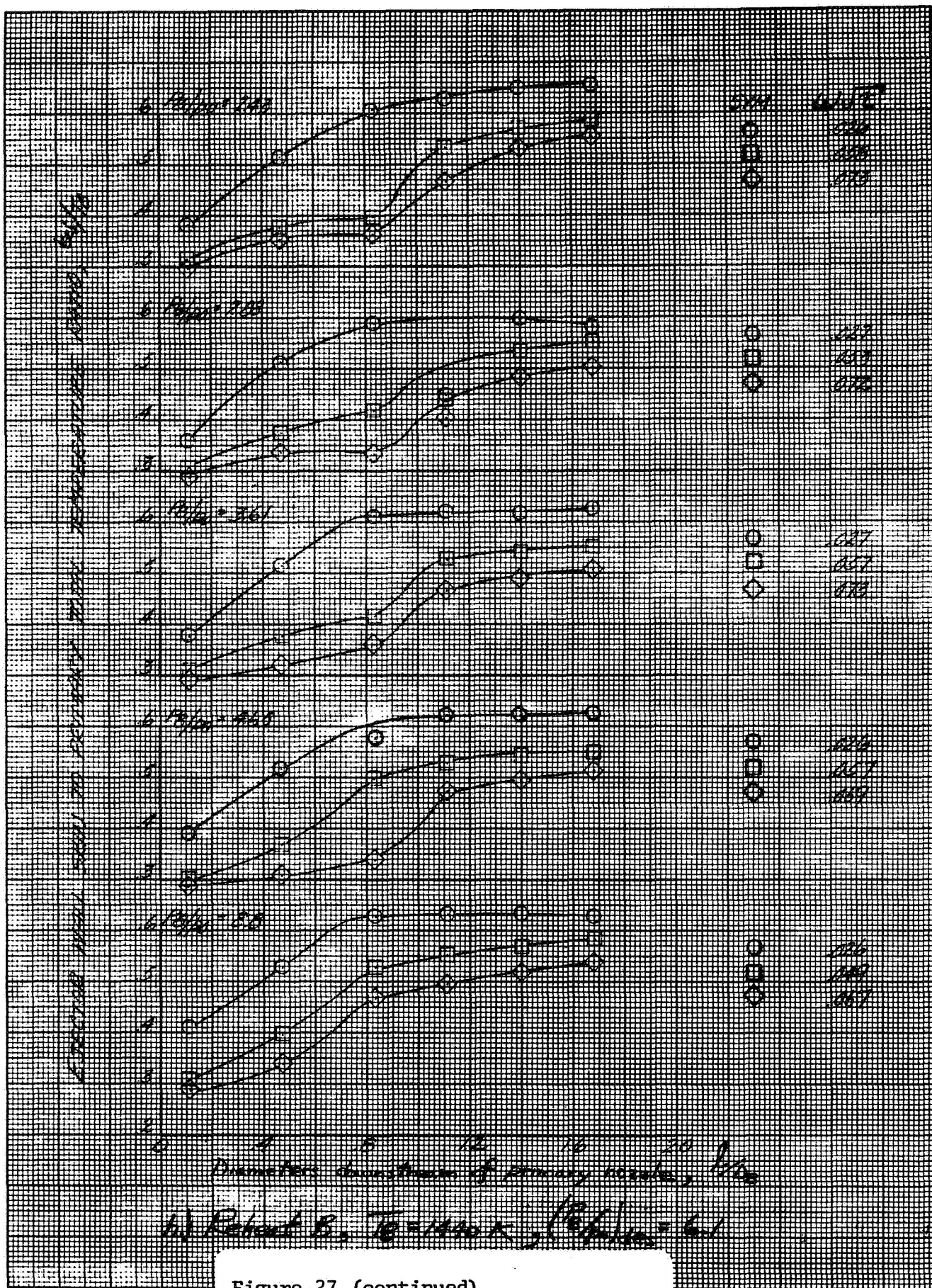
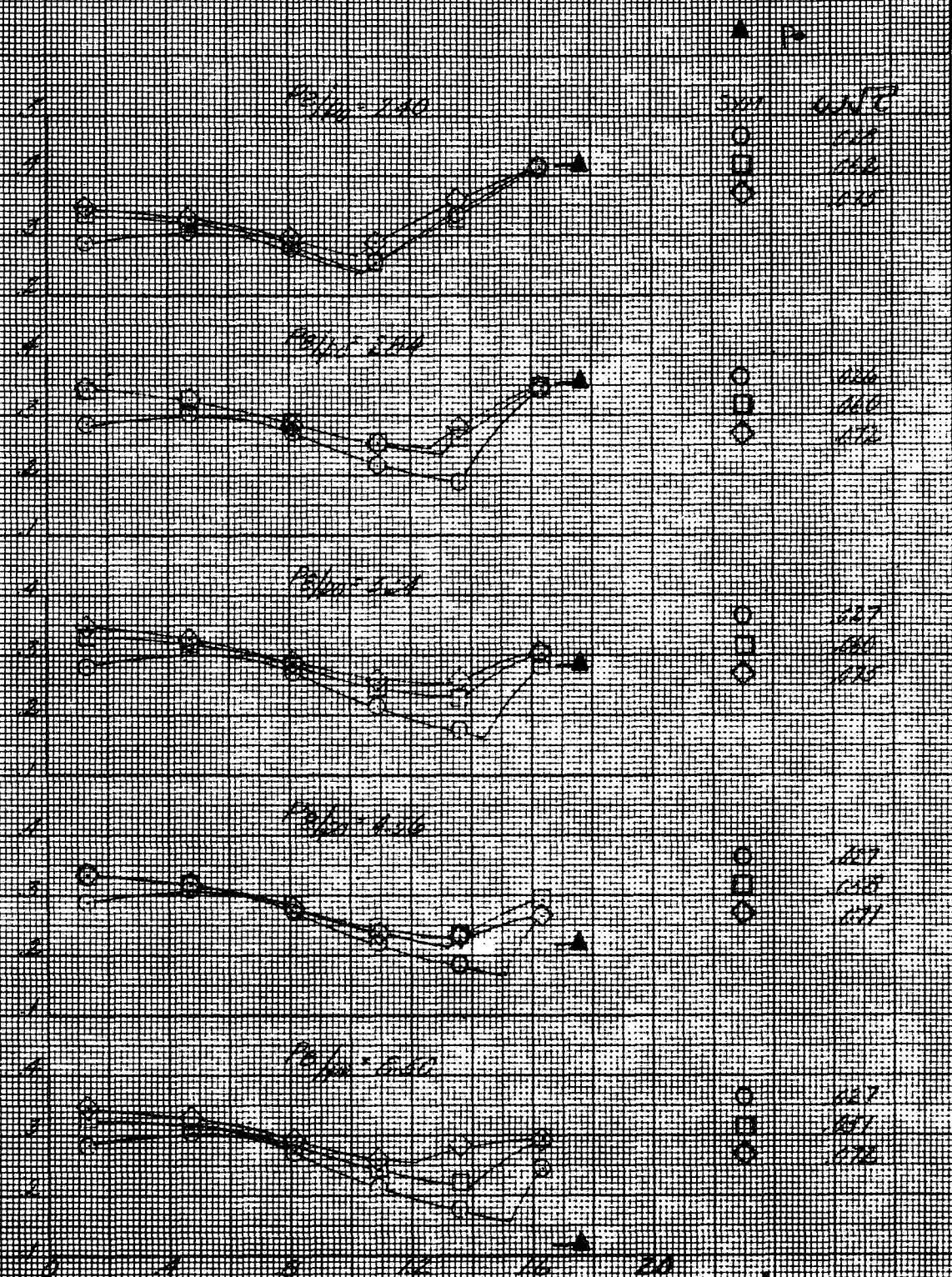


Figure 27 (continued)

Pressure and time to rupture and average area, P_0/P_{cr}



Diameter downstream of primary nozzle, D/D_0
 [] Reheat A, $E = 12.6 \times 10^4 \text{ ft}^2/\text{sec}^2$, $(P_0/P_{cr}) = 5.0$

Figure 27 (continued)

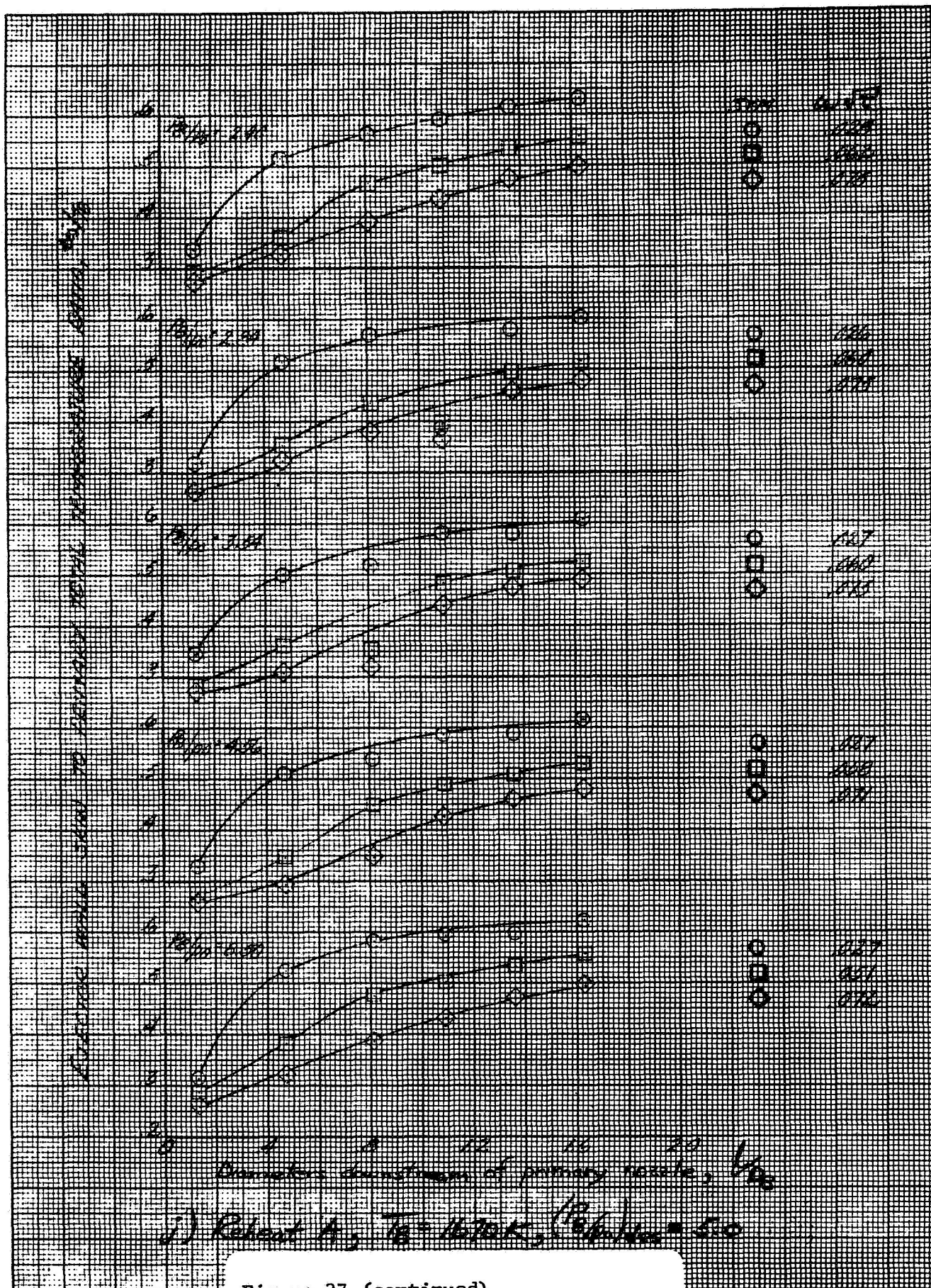


Figure 27 (continued)

Curves were taken at 10-15 sec. after maximum release of pressure

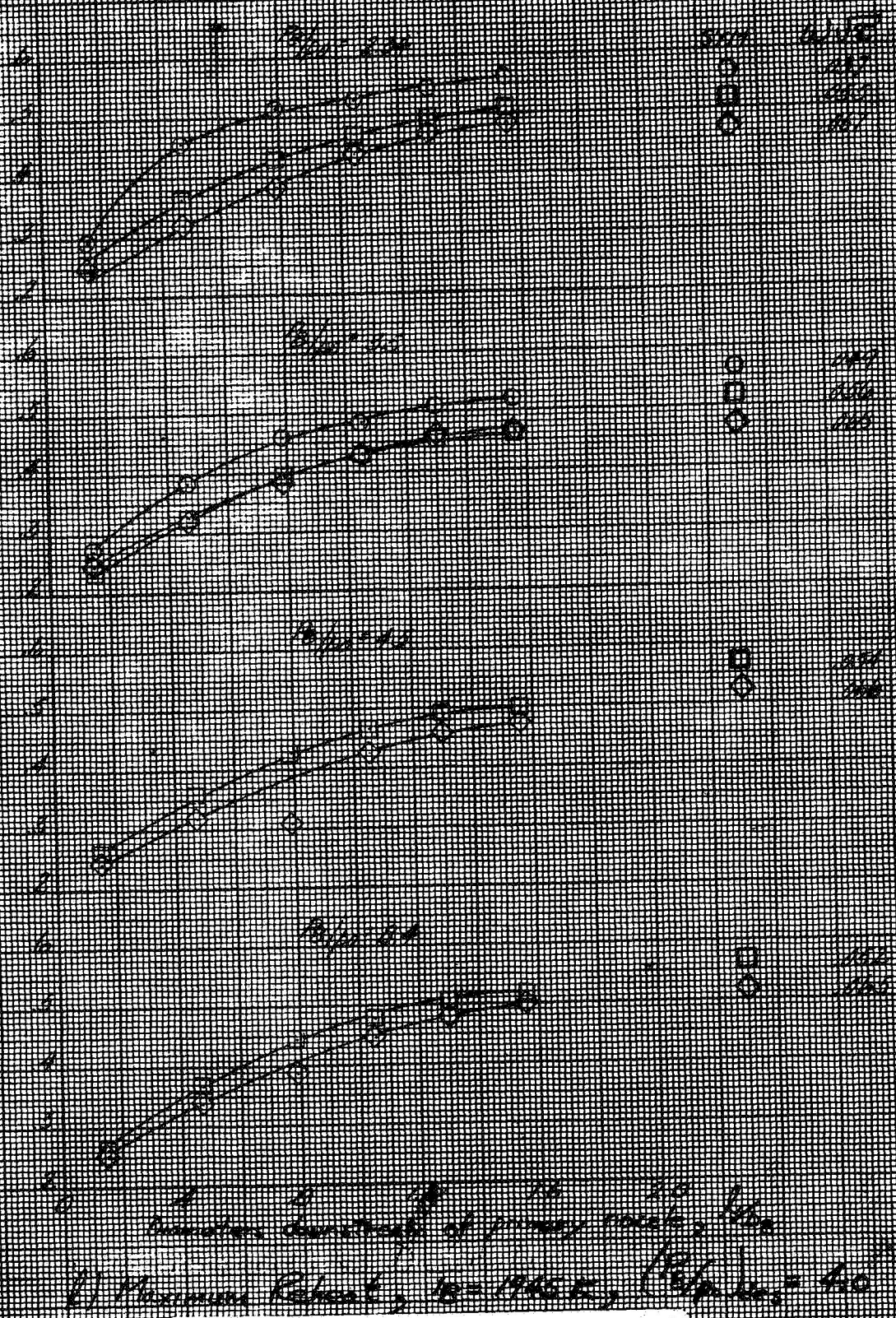


Figure 27 (concluded)